2011-07-27

Simulation Assisted Robotic Orthopedic Surgery in Femoroacetabular Impingement

Ta-Cheng Chang
University of Miami, tcchang1@gmail.com

Follow this and additional works at: https://scholarlyrepository.miami.edu/oa_dissertations

UNIVERSITY OF MIAMI

SIMULATION ASSISTED ROBOTIC ORTHOPEDIC SURGERY IN
FEMOROACETABULAR IMPINGEMENT

By

Ta-Cheng Chang

A DISSERTATION

Submitted to the Faculty
of the University of Miami
in partial fulfillment of the requirements for
the degree of Doctor of Philosophy

Coral Gables, Florida

August 2011

UNIVERSITY OF MIAMI

A dissertation submitted in partial fulfillment of
the requirements for the degree of
Doctor of Philosophy

SIMULATION ASSISTED ROBOTIC ORTHOPEDIC SURGERY IN
FEMOROACETABULAR IMPINGEMENT

Ta-Cheng Chang

Approved:

_____
Weizhao Zhao, Ph.D.
Associate Professor of
Biomedical Engineering

_____
Terri A. Scandura, Ph.D.
Dean of the Graduate School

_____
Jorge Bohorquez, Ph.D.
Assistant Professor of
Biomedical Engineering

_____
Chun-Yuh Huang, Ph.D.
Assistant Professor of
Biomedical Engineering

_____
Louis Arata, Ph.D.
Chief Software Architect
MAKO Surgical Corp.
Fort Lauderdale, Florida

_____
Hyosig Kang, Ph.D.
Director, Platform & Research
Application
MAKO Surgical Corp.
Fort Lauderdale, Florida

CHANG, TA-CHENG   (Ph.D., Biomedical Engineering)
<u>Simulation Assisted Robotic Orthopedic</u>   (August 2011)
<u>Surgery in Femoroacetabular Impingement</u>

Abstract of a dissertation at the University of Miami.

Dissertation supervised by Professor Weizhao Zhao.
No. of pages in text. (138)

Femoroacetabular impingement (FAI) has been increasingly recognized as a cause of early hip osteoarthritis. FAI is characterized by pathologic contact between the femur and acetabular rim during hip join movement, caused by morphological abnormalities. Arthroscopic technique has become increasingly popular for FAI surgical treatment because of its minimal invasiveness. However, it involves cumbersome procedures and over- or under-resection are likely to occur. To tackle this issue, robot-assisted FAI arthroscopy is a well suited approach because it results in high accuracy and reproducible surgical outcomes.

This dissertation provides new approaches and methods for the current challenges in the development of robot-assisted FAI arthroscopy. The study has three objectives: 1) to develop a robust calibration method for the A-mode ultrasound probe used for noninvasive bone registration, 2) to develop a bone registration simulator for verifying the registration accuracy and consistency for any given registration point-pattern, and 3) to develop a hip range of motion simulation system that returns the virtual range of motion and determines the bone resection volume.

Carefully designed calibration procedures and simulation experiments have been conducted during the study of this research. From the experimental results, the developed

ultrasound calibration method successfully reduces the registration errors and is proved to be robust. The results from the registration simulator indicate that the pattern with widely distributed points lead to better registration accuracy and consistency. The hip range of motion simulation system results in acceptable accuracy and successfully generates the resection volume.

With further modifications, the ultrasound probe can be successfully calibrated with the developed method, and will be applied for noninvasive bone registration. The registration simulator can also be served as a useful tool for determining the optimized registration point-pattern, which can lead to reduced surgical trauma and registration time. Finally, the developed range of motion simulation system can allow the surgeon to evaluate the surgical outcome and to determine the resection volume even before the surgery begins. To conclude, this dissertation provides useful approaches, methods, and software for developing robot-assisted FAI arthroscopy.

ACKNOWLEDGEMENTS

Lastly and most importantly, I want to express my deepest appreciation and love to my parents, my brother and sister, and all the family members. Without their unconditional love and continued encouragement, I would never have the life-changing opportunity to study abroad and accomplish this dissertation.

Ta-Cheng Chang
August 2011, Miami

TABLE OF CONTENTS

CHAPTER 5

CHAPTER 6

LIST OF FIGURES

LIST OF TABLES

ABBREVIATIONS

3D: Three-Dimensional

APP: Anterior Pelvic Plane

ASIS: Anterior Superior Iliac Spine

BPA: Ball-Pivoting Algorithm

CAOS: Computer-Assisted Orthopedic Surgery

CMM: Coordinate Measurement Machine

CT: Computed Tomography

DICOM: Digital Imaging and Communications in Medicine

FAI: Femoroacetabular Impingement

FDA: Food and Drug Administration

GUI: Graphical User Interface

ICP: Iterative Closest Point

LMA: Levenberg–Marquardt Algorithm

MRI: Magnetic Resonance Imaging

NSAID: Nonsteroidal Anti-Inflammatory Drug

OA: Osteoarthritis

PC: Personal Computer

PSIS: Posterior Superior Iliac Spine

RMS: Root Mean Square

ROI: Region of Interest

ROM: Range of Motion

SCFE: Slipped Capital Femoral Epiphysis

STL: Stereolithography

THR: Total Hip Replacement

UKA: Unicompartmental Knee Arthroplasty

US: Ultrasound

CHAPTER 1

INTRODUCTION

Hip pain has been frequently associated with osteoarthritis (OA) in the joint. However, recently studies have proposed that femoroacetabular impingement (FAI) is a non-arthritic source of hip pain commonly seen in young patients. FAI has been increasingly recognized as an etiological cause of early OA of the hip, particularly in active young adults and athletes with groin pain (Ganz et al., 2003; Tanzer and Noiseux, 2004; Beck et al., 2005). The estimated prevalence of FAI in the general population is about 10-15% while the latest studies at the time of writing indicate that the prevalence may be even higher (Tannast et al., 2007b; Keogh and Batt, 2008; Kang et al., 2010). The number of scientific studies on FAI has also grown almost exponentially during recent years (Leunig et al., 2009).

FAI is characterized by pathologic contact between the proximal femur and acetabular rim during hip join motion, caused by morphological abnormalities of the femoral head or head-neck junction, acetabulum, or both. The abnormal impingement can lead to acetabular labral tears and intra-articular cartilage damage. FAI also reduces the physiologic hip range of motion (ROM) and produces pain in patients during daily activities. The goal of FAI surgical treatment is to alleviate the pain by repairing the damaged soft tissue and removing the bony deformity on the proximal femur in order to restore the normal bone morphology as well as hip ROM. Conventional surgical techniques for FAI include open hip dislocation (Ganz et al., 2001;

www.manaraa.com

Peters and Erickson, 2006a) and a less invasive alternative with minimal incisions, i.e., hip arthroscopy (Guanche and Bare, 2006; Philippon et al., 2007b; Horisberger et al., 2010).

Superior precision and minimal invasiveness have been desired in orthopedic surgery for decades. As technology advances, computer-assisted orthopedic surgery (CAOS) has become increasingly popular since it seems promising to achieve above goals. CAOS has been proven feasible in different orthopedic procedures such as pedicle screw placement (Amiot et al., 2000; Schlenzka et al., 2000), total hip arthroplasty (DiGioia, III et al., 2003; Widmer and Grutzner, 2004), total knee arthroplasty (Anderson et al., 2005; Luring et al., 2008), and partial knee arthroplasty (Jenny et al., 2007; Jamali et al., 2009). Recently, driven by computer hardware and software, robot-assisted orthopedic surgery has emerged from CAOS because it assists the surgeon to achieve consistently reproducible and accurate surgical outcome (Conditt and Roche, 2009; Pearle et al., 2010).

Robot-assisted orthopedic surgery usually consists of three major components: pre-operative virtual planning, intra-operative navigation, and robotic surgical intervention (Adili, 2004). It allows the surgeon to design a pre-operative surgical plan based on the three-dimensional (3D) data generated from computed tomography (CT) or magnetic resonance imaging (MRI) images. The robotic arm is controlled by a computer and guides the surgeon to execute procedures precisely by following the pre-defined plan. Robot-assisted surgical system usually involves a tracking mechanism to provide intra-operative navigation for the surgeon. With the navigation, direct visualization of the surgical site is not required therefore the surgical trauma can be minimized. In short,

computer-assisted robotic orthopedic surgery increases surgeon's confidence shortens both surgical and recovery time, and reduces post-operative complications.

1.1 MOTIVATION

Conventional FAI arthroscopic surgery is performed by inserting an endoscopy and instruments into the hip joint through multiple "portals" with small incisions. During the procedure, iterative bone debridement and confirmation of the resection are required intra-operatively. The surgeon has to constantly and visually evaluate the geometry of the anatomical features by taking multiple fluoroscopic images of the surgical site in order to check if the pre-determined anatomical parameters are achieved (Notzli et al., 2002; Johnston et al., 2008). The hip also undergoes a ROM test to confirm if the normal kinematics is restored through the resection.

These iterative procedures, however, may not only require extra operative time due to the cumbersomeness, but also result in over- or under-resection because the bone resection outcome can only be assessed after the debridement (Ilizaliturri, Jr., 2009; Larson and Wulf, 2009; Mardones et al., 2009; Matsuda, 2009). Over-resection can lead to femoral neck fracture and under-resection may require a revision arthroscopy (Mardones et al., 2005; Heyworth et al., 2007; Philippon et al., 2007b). Moreover, the bone resection outcomes may be in poor consistency because of the error caused by human factors. In addition, with current techniques, the necessity of fluoroscopic images also risks the patient under extra radiation exposure.

To address these problems, computer-assisted robotic orthopedic surgery is a well suited approach because it yields accurate and reproducible bone resurfacing results. The over- or under-resection can hence be avoided and the inconsistency of resections can also be eliminated. With robot-assisted FAI surgery, the repeated confirmation with fluoroscopic images is no longer required so that the surgical time as well as the radiation exposure of patients can be diminished.

1.2 RESEARCH CHALLENGES AND OBJECTIVES

In robot-assisted orthopedic surgery, registration is a key step for the system to provide intra-operative navigation. It establishes the spatial coordinate mapping between the patient's surgical site and the 3D computer data set (Ma and Ellis, 2003). With successful registration, the system can therefore provide the intra-operative details to the surgeon about how the surgery is being executed on the actual anatomy. Conventional methods for bone registration include fiducial-based or surface-based techniques with mechanical probes to collect data points on the bone surface. These methods usually requiring extra or extensive incisions to access the bone for obtaining satisfactory data points, however, increase the surgical trauma and reduce the power of CAOS (Kozak et al., 2002; Amiot and Poulin, 2004).

Due to the nature of FAI arthroscopic procedure, only a limited area of the bone is accessible for surface-based registration. Therefore, an alternative method to noninvasively collect bone registration data points is highly desirable. For conventional surface-based bone registration, a method to define an ideal registration "point-pattern,"

which requires only a small number of data points within the limited accessible area but resulting in acceptable accuracy, is also desired.

In addition, robot-assisted FAI arthroscopic surgery also consists of major components of robot-assisted surgery including pre-operative planning, intra-operative navigation, and robotic intervention. During pre-operative planning, the surgical system should be able to instantly return the surgical outcome of the resection plan. In order to virtually assess the resection result, a software system capable of simulating hip ROM and generating the "to-be-removed" resection volume by given bone models is desirable. With the software system, the surgeon can finalize the surgical plan based on the returned ROM information and the suggested resection volume through the simulations. The robotic arm then guides the surgeon to perform accurate bone debridement.

To address the challenges stated above, the three objectives of the present study are:

- To calibrate the noninvasive A-mode ultrasound (US) bone registration system pre-developed by our group (Mozes et al., 2010) for robot-assisted FAI arthroscopic surgery, under the MAKO RIO Robotic Arm Interactive Orthopedic System (MAKO Surgical Corp., Fort Lauderdale, FL, USA).

- To develop a bone registration simulator for verifying the registration accuracy and consistency of a given "point-pattern" for robot-assisted FAI arthroscopic surgery.

- To develop a virtual hip ROM simulation system that can generate the bone resection volume based on given bone models for robot-assisted FAI arthroscopic surgery.

1.3 SIGNIFICANCE OF THE STUDY

Recent publications have suggested that A-mode US might be feasible for noninvasive bone registration in CAOS (Amstutz et al., 2003; Moulder et al., 2003; Heger et al., 2005; Heger et al., 2007; Oszwald et al., 2008; Fieten et al., 2009; Fieten et al., 2010). US calibration has also been addressed as an important issue. Different US calibration techniques have been proposed (Mercier et al., 2005; Fieten et al., 2009). Successful calibration can greatly reduce the errors caused by the acoustic variation of soft tissue and the geometric difference between US signal and physical location (Barratt et al., 2001; Barratt et al., 2006). This study demonstrates a robust calibration method for A-mode US bone registration. With further modifications, the calibrated A-mode US probe can be used to replace the conventional mechanical probes; hence noninvasive bone registration can be achieved without extra surgical trauma in robot-assisted FAI arthroscopic surgery.

Successful registration leads to accurate intra-operative navigation and thus the pre-defined surgical plan can be performed precisely. For surface-based registration, selection of data points in terms of the number of points and location of sampled points, which are so called "point-pattern," has been indicated as an important variant which can significantly influence the registration accuracy (Simon, 1996; Glozman et al., 2001; Rusinkiewicz and Levoy, 2001; Gelfand et al., 2003). The proposed registration simulator accommodates various parameters and point-patterns to simulate how they affect the registration result. This simulator is a useful tool for determining the ideal registration point-pattern, which not only leads to superior registration accuracy, but also requires a small number of data points within the accessible area. The later therefore minimizes

both the surgical trauma and data collection time in robot-assisted FAI arthroscopic surgery.

For hip ROM simulation, several impingement detection methods have been proposed; however, they primarily focus on dealing with a ball-and-socket model for the hip anatomy (Kawasaki et al., 2004; Arbabi et al., 2007; Arbabi et al., 2009; Cai et al., 2009; Arbabi et al., 2010). These methods thus may not be ideal for non-ball-and-socket models such as knee, spine, or wrist. Some methods detect impingement but cannot return the penetration depth of the impingement for generating a bone resection volume (Hu et al., 2001; Kubiak-Langer et al., 2007; Tannast et al., 2007a). In this study, a general impingement detection method based on 3D computer graphical models has been developed. This method not only provides the information about penetration depth but also can be implemented into various orthopedic applications, not restricted to the ball-and-socket movement. Furthermore, the hip ROM simulation system proposed in this study allows the surgeon to evaluate the surgical outcome and to determine the resection volume even before the surgery begins. In this way, the resection volume can be quantified, the human error can be diminished, and radiation exposure of patients can be reduced as well.

1.4 DISSERTATION OVERVIEW

The dissertation is organized as follows. In Chapter 2, a medical background of hip joint anatomy and FAI is described. A brief technical overview of computer-assisted robotic orthopedic surgery is then provided. Chapter 3 presents an enhanced calibration method using an A-mode US probe designed for noninvasive bone registration with a 3D

optical tracking system. The location of the transmitting/sensing element inside the US transducer housing is calibrated based on a nonlinear optimization algorithm. The accuracy and the robustness of the calibrated US probe are also evaluated.

Chapter 4 covers a software based bone registration simulator. A femoral model generated by CT images is loaded into the simulator. The registration results based on this model with different point-patterns and registration parameters are presented. Chapter 5 deals with the development of a hip ROM simulation system. An impingement detection system is first developed using bounding sphere computer graphic algorithm. Both precision and accuracy of the impingement detection system are verified by using a custom-designed phantom. Next, the impingement detection system is implemented into the hip ROM simulation system, which simulates the ROM of different hip joint motions and generates the "to-be-removed" bone resection volume. The simulated ROM is then verified by manipulating sawbones under the navigation of a tracking system. Lastly, Chapter 6 summarizes the works of this study and suggests possible directions for future work. Figure 1-1 below illustrates an overview of the major tasks completed in this study.
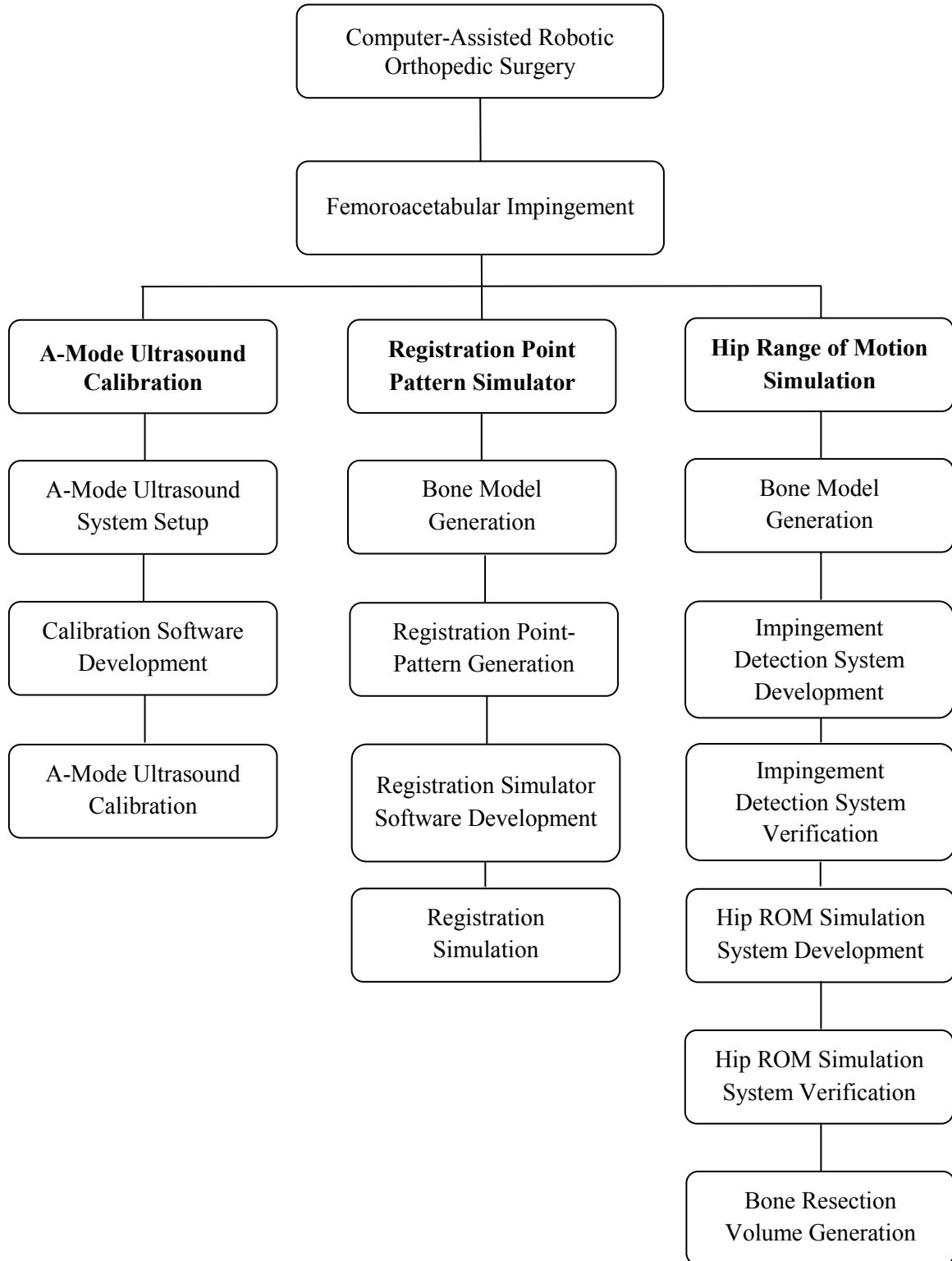
Figure 1-1: Illustration of the major tasks of the study. In total thirteen tasks under three objectives are completed.

CHAPTER 2

BACKGROUND

This chapter describes a medical background and a technical background of this dissertation. The anatomy of the hip joint is firstly discussed to provide the reader with a better understanding of the general knowledge of orthopedics. A more detailed background of FAI including pathology, etiology, diagnosis, and treatment options is then given. After this, a history and state of the art technology of computer-assisted robotic orthopedic surgery are introduced.

2.1 ANATOMY OF THE HIP JOINT

The hip joint is a ball-and-socket joint consisting of the head of the femur and the acetabulum of the pelvis. Hip joint allows a wide range of movements including flexion, extension, abduction, adduction, internal rotation, and external rotation with three degrees of freedom (Keogh and Batt, 2008). During childhood, the pelvis is comprised by three separated bones, the ilium (superior region), the ischium (posterior region), and the pubis (anterior region), as illustrated in Figure 2-1. These bones are fused and their boundaries become indistinguishable in adolescence. The superior region of the ilium is a "wing-like" expanded portion called ala. Ala consists of a thickened superior margin named iliac crest, which stretches posteriorly from a blunt anterior superior iliac spine (ASIS) to a sharp posterior superior iliac spine (PSIS). The anterior border of the pubis is thickened

to form a pubic crest. A prominent "knob-like" pubic tubercle is located at the lateral end of the pubic crest. A "cup-shaped" cavity of the pelvis called the acetabulum is formed by aspects of the three bones and articulates with the femur in the hip joint. The articular surface of the acetabulum is attached with a "U-shaped" cartilage (the lunate surface) except the central region (the acetabular fossa) and the inferior portion (the acetabular notch) of the acetabulum.
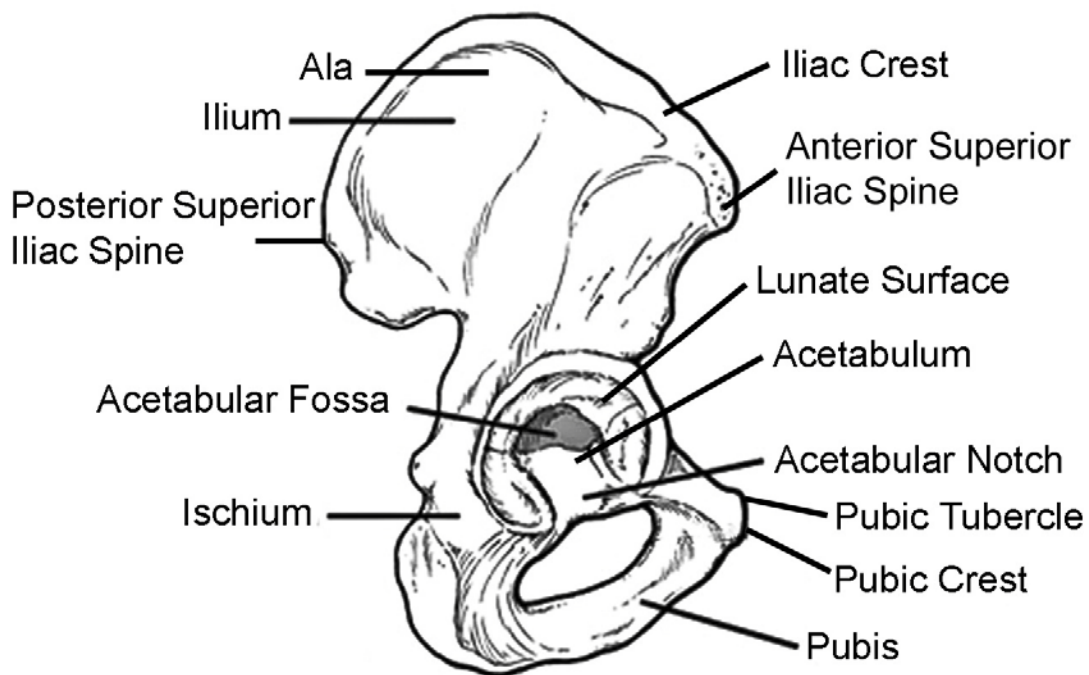
Figure 2-1: Lateral view of a left hemi-pelvis. The pelvis is comprised by three bones and consists of a deeply cupped acetabulum (Marieb and Mallatt, 1996; Dorland, 2000).

The femur, the single bone of the thigh, is the longest and strongest bone in the body. The medial portion of the proximal femur is a "ball-like" femoral head, which is connected to the femoral shaft through the femoral neck, as shown in Figure 2-2. The femoral head is approximately spherical and has a small pit, fovea capitis, at the center. The contour of the femur becomes concave at the femoral head-neck junction. The greater trochanter locates at the lateral side of the junction of the shaft and neck, while the lesser trochanter, the medial. The distal portion of the femur ends in lateral and medial condyles. These two condyles have the most prominent points on the sides called the lateral epicondyle and medial epicondyle respectively.

The hip joint is encompassed by a fibrous joint capsule, which increases the stability of the joint (see Figure 2-3). Three major ligaments reinforce the joint capsule: a) the iliofemoral ligament, a V-shaped ligament tightened in hip extension, locates anteriorly from the superior region of the acetabulum to both the anterior-superior and anterior-inferior regions of the femoral neck; b) the pubofemoral ligament, a triangular ligament tightened in hip extension and abduction, locates inferiorly from the anterior portion of the acetabulum to the inferior region of the femoral neck; and c) the ischiofemoral ligament, a spiral ligament tightened in hip extension and internal rotation, locates posteriorly from the posterior portion of the acetabulum to the superior region of the femoral neck.
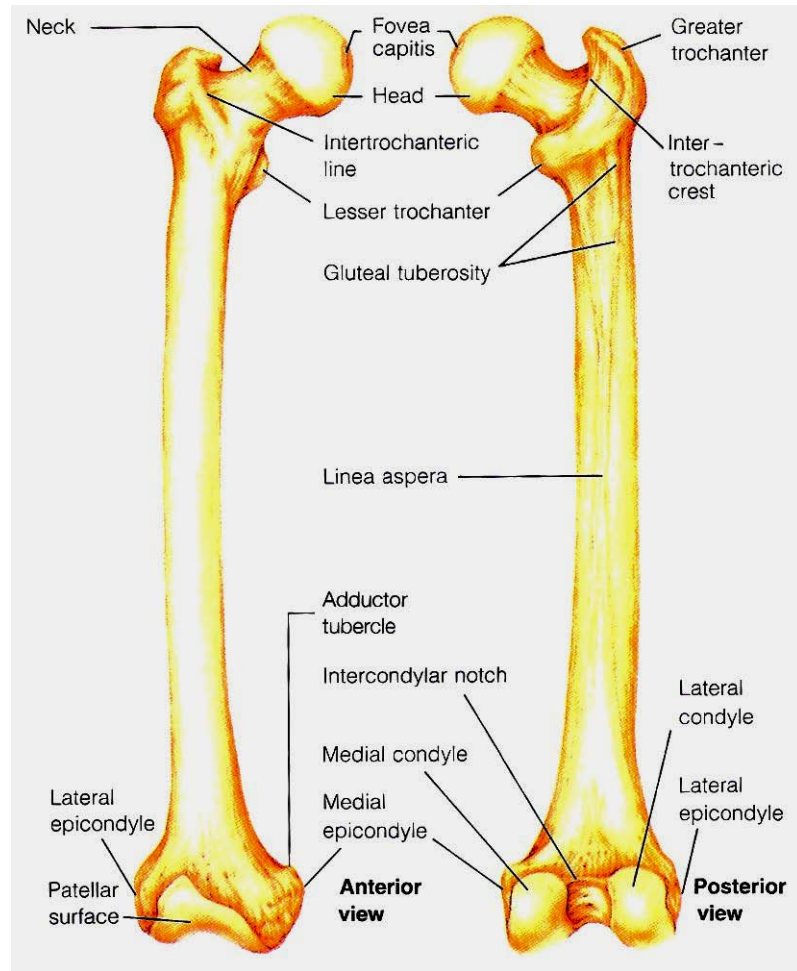
Figure 2-2: Anterior view (left) and posterior view (right) of a right femur (Marieb and Mallatt, 1996).
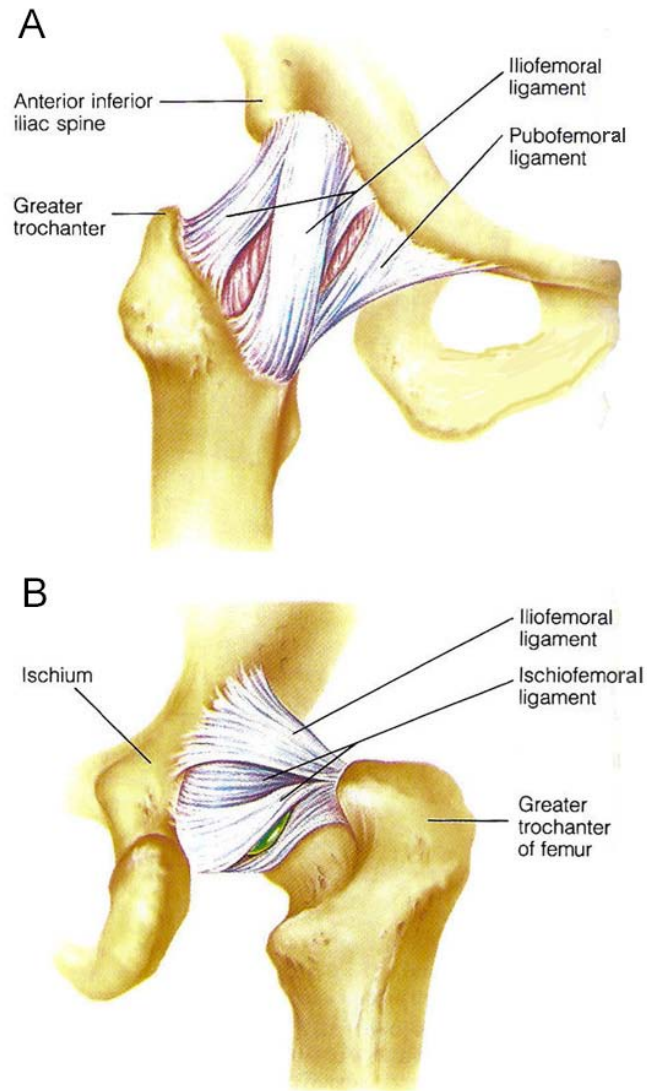
Figure 2-3: A) Anterior view of the hip joint. B) Posterior view of the hip joint (Marieb and Mallatt, 1996).

Inside the hip joint, the capsule is filled with synovial fluid secreted from the synovial membrane. A ligament called ligamentum teres runs from the fovea capitis of the femoral head to the acetabular notch, as shown in Figure 2-4. A circular fibrocartilaginous rim called the acetabular labrum is attached to the bony edge of the acetabulum. The diameter of the labrum is less than that of the femoral head; thus the labrum deepens the acetabulum by preventing the femoral head from slipping out of the socket.
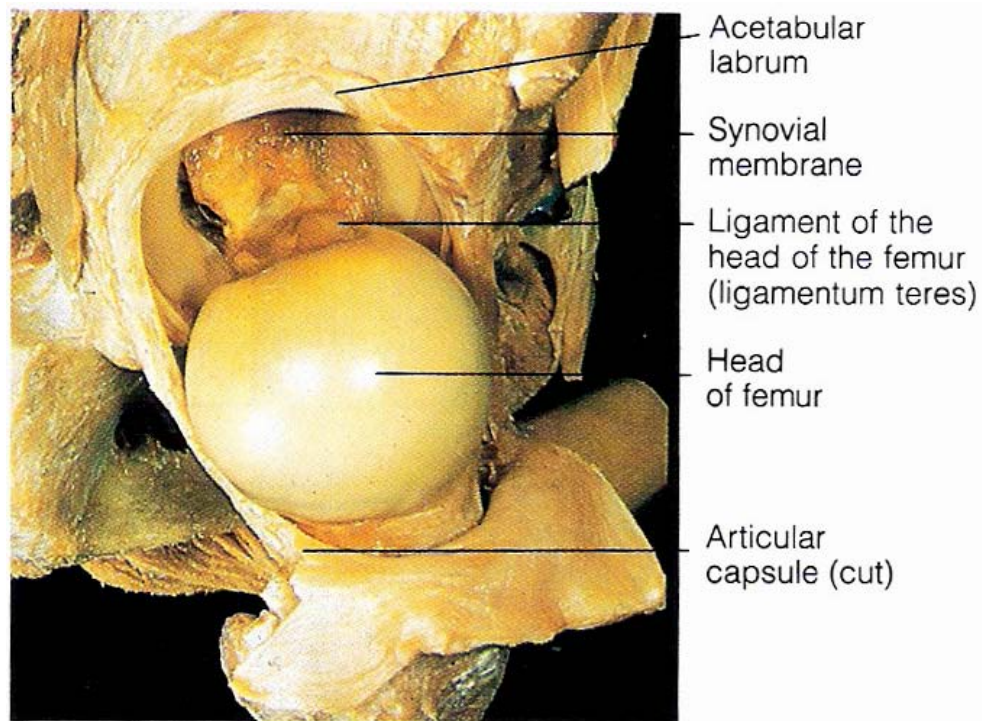
Figure 2-4: Photograph of the interior of the hip joint (Marieb and Mallatt, 1996).

2.2 FEMOROACETABULAR IMPINGEMENT

FAI results from abnormal contact between the proximal femur and acetabular rim during hip joint movement. FAI is caused by morphological abnormalities of the femoral head or head-neck junction, acetabulum, or both, and thus leads to acetabular labrum and cartilage damage as well as early OA. FAI decreases hip ROM and causes pain in patients. Stulberg et al. (Stulberg and Harris, 1974; Stulberg et al., 1975) first reported the association between the abnormal morphology of the hip and the development of idiopathic arthritis. They described abnormal head-neck offset, which they called "pistol grip deformity" and is now referred to as FAI, in patients with early hip OA. Their finding was then supported by Harris (Harris, 1986), who investigated 75 patients with idiopathic OA of the hip and found that 40% had "pistol grip deformity." It was not until more recently that the research of FAI significantly increased. Ganz et al. (Ganz et al., 2003) classified FAI into two types: cam and pincer impingements. Cam impingement, characterized by femoral deformities and previously described as "pistol grip deformity," involves a non-spherical femoral head and insufficient head-neck offset, causing impingement against the acetabular rim. Pincer impingement, characterized by acetabular deformities, involves over coverage of the acetabulum, resulting in contact between the acetabular rim and the femoral head-neck junction. Cam impingement is more common in young and athletic males, while pincer impingement is more frequently seen in middle aged athletic females. In clinical, often a combination of cam and pincer impingements can lead to the development of FAI. An illustration of anterior FAI can be found in Figure 2-5 below.
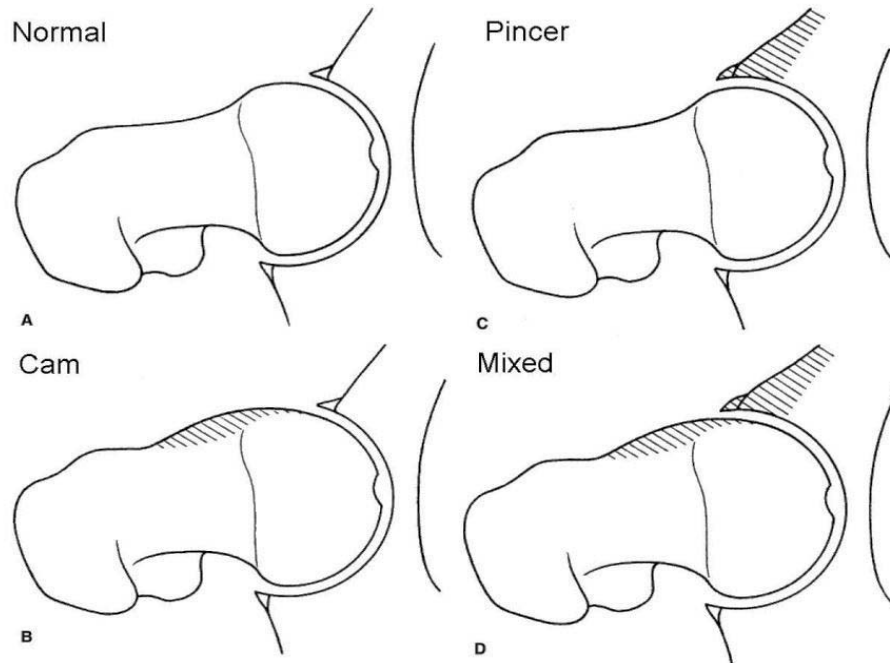
Figure 2-5: Anterior femoroacetabular impingement. A) Normal hip, B) Cam impingement, C) Pincer impingement, and D) Mixed (Lavigne et al., 2004).

Cam impingement causes excessive force across the cartilage along the acetabular rim, resulting in large cartilage abrasions, flaps, detachment, and eventually the damage of adjacent labrum in the form of labral tears, as illustrated in Figure 2-6. Pincer impingement deepens the acetabulum and results in a chondral injury along the acetabulum. The acetabular cartilage lesions caused by pincer impingement are often limited to a small region and therefore less problematic than the lesions seen in cam impingement (Kassarjian et al., 2006).
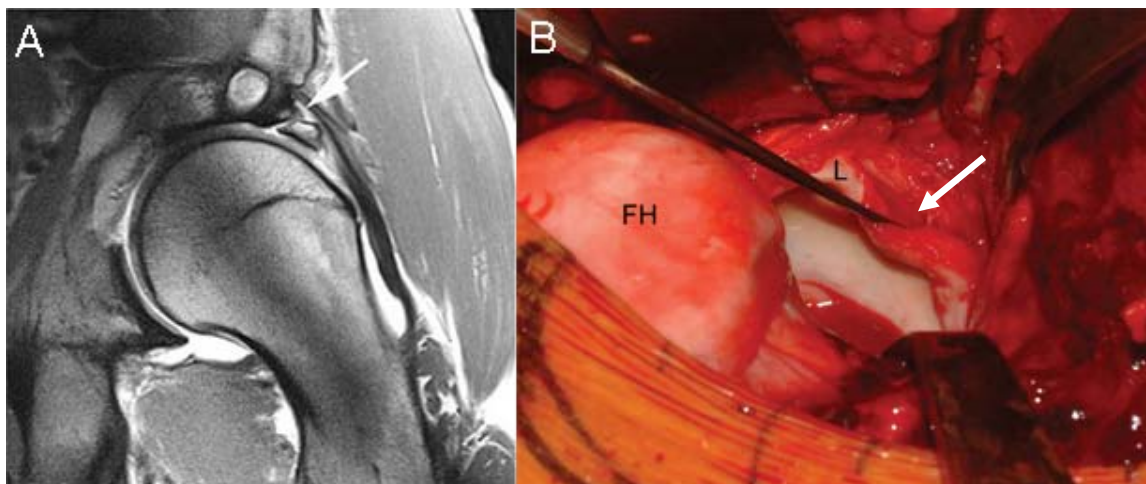
Figure 2-6: A) MR image of cam FAI-induced acetabular rim fracture (arrow) and cartilage damage (Leunig et al., 2009). B) Photograph of labral tears (arrow) (Bizzini et al., 2007).

Although the etiology of FAI has not yet completely identified, predisposing conditions have been reported such as slipped capital femoral epiphysis (SCFE), Legg-Calve-Perthes disease, hip dysplasia, coxa magna, post-traumatic acetabular dysplasia and femoral retrotorsion, and iatrogenic deformities (Kassarjian et al., 2006; Leunig et al., 2009). Nevertheless, studies (Kassarjian et al., 2006) have reported that patients without these etiological conditions may still have FAI.

Patients with FAI usually experience insidious onset groin pain. The pain is intermittent in the early stages and becomes worse with physical activities or prolonged sitting. Methods for FAI diagnosis include clinically physical examination and radiographic evaluation. As for physical examination of FAI, anterior impingement test is performed with a patient lying supine, as shown in Figure 2-7. The hip is passively flexed to 90° then internally rotated by the examiner. Posteroinferior impingement test is also

performed with the patient in the supine position, but the hip is externally rotated while the patient extends the hip.

Figure 2-7: A) Anterior impingement test. B) Posteroinferior impingement test (Kaplan et al., 2010).

Conventional radiographic evaluation for FAI includes radiographs in an anterior-posterior view of the pelvic, an axial "cross-table" view of the proximal femur, and a "Dunn/Rippstein" view (Meyer et al., 2006; Tannast et al., 2007b; Leunig et al., 2009). To quantitatively evaluate cam FAI, the current standard method is to measure the alpha angle on an oblique image through the axis of the femoral neck in the lateral view of the hip. A circle that best fits the femoral head is first determined and bisected by a line connecting the femoral head center (center of the circle) and the femoral neck center. Next, a second line is drawn from the center of the circle to the point where the femoral

head first exceeds the radius of the circle anteriorly. The alpha angle is then defined as the angle between these two lines, as illustrated in Figure 2-8. In a study conducted by Notizli et al. (Notzli et al., 2002), all patients with cam impingement had greater alpha angle than which in the control group, and an alpha angle of 55° was suggested as a threshold for determining the presence of cam FAI.
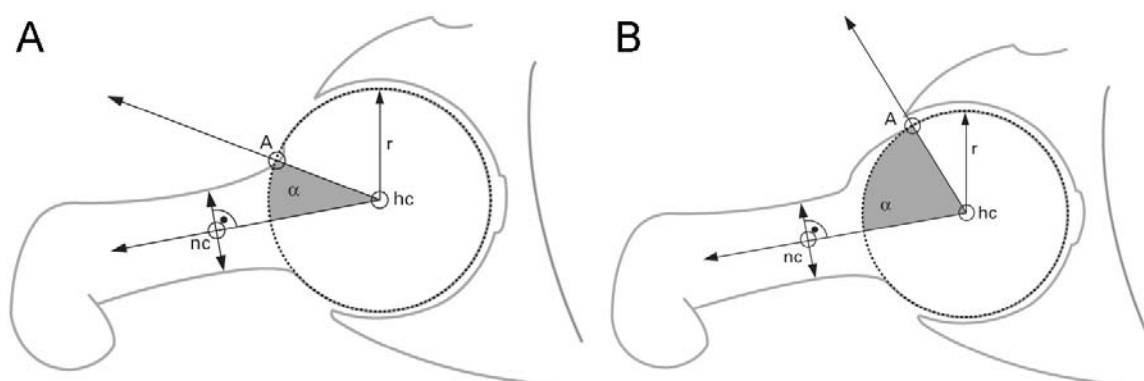
Figure 2-8: Diagrams showing the alpha angle measurement in A) normal hip and B) hip with cam FAI. Point A is where the distance from the center of the femoral head (hc) exceeds the radius (r) of the best-fit circle. Point nc is the center of the femoral neck. The alpha angle is defined as the angle between the line A-hc and line hc-nc (Notzli et al., 2002).

FAI treatment usually starts with conservative treatment, which typically includes activity modification, restriction of athletic pursuits, and reduction of excessive motion of the hip, together with appropriate nonsteroidal anti-inflammatory drugs (NSAIDs) to reduce the pain (Lavigne et al., 2004). The conservative treatment may be temporarily successful in alleviation of the pain; however, if the symptoms persist or the distinct labral and chondral damage present, surgical intervention is then considered as the treatment option.

The goals of the surgical treatment of FAI are to increase the clearance between the femoral head and the acetabular rim for hip motion, so that the abnormal contact can be eliminated. As for cam impingement, the prominent femoral neck or non-spherical portion of the femoral head is reshaped by resection osteoplasty to optimize the head-neck offset or the sphericity of the head. As for pincer impingement, the excessive acetabular rim is removed by resection osteoplasty to reduce the over coverage of the acetabulum. The surgical options include open procedures involving surgical dislocation of the hip (Ganz et al., 2001; Murphy et al., 2004; Peters and Erickson, 2006b) and minimally invasive arthroscopic procedures (Guanche and Bare, 2006; Philippon et al., 2007b; Horisberger et al., 2010). As Figure 2-9 shows, open hip dislocation provides a full 360° view of the femoral head and the acetabulum to the surgeon. The location of the impingement is identified and the lesions on the labrum and acetabular cartilage are addressed. Open technique is still the primary approach for FAI with complex abnormalities such as extra-articular impingement, major deformities, and global pincer FAI (Leunig et al., 2009).
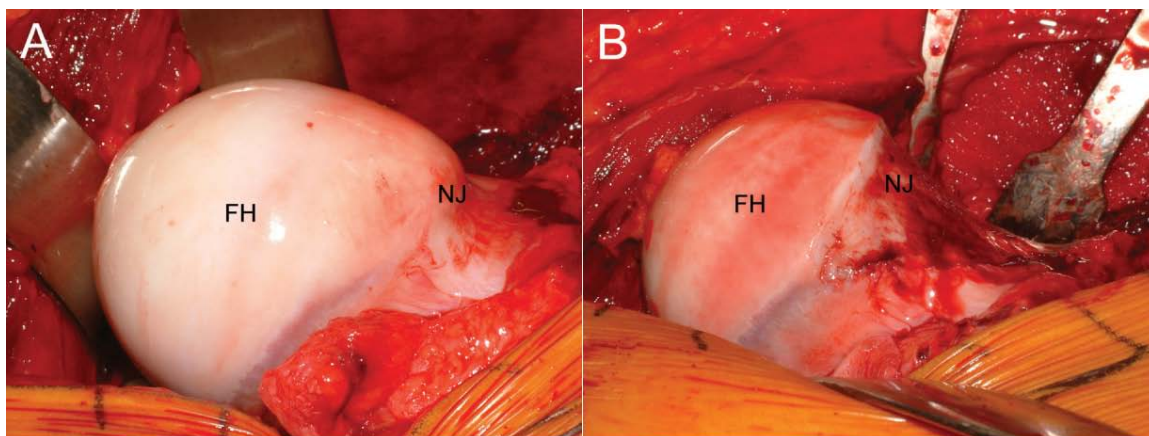
Figure 2-9: Photographs showing the open hip dislocation. A) Before the resection osteoplasty. B) After the resection osteoplasty (Bizzini et al., 2007).

In contrast, arthroscopic technique has become increasingly popular for treating cam and/or pincer impingement with minor deformities to avoid the large exposure of open technique. Arthroscopy is performed with the patient in either the lateral or the supine position. The patient is positioned on a fracture table. The operative extremity is distracted to separate the femoral head from the acetabulum and create a space within the central compartment of the hip. Three standard portals, namely anterior, anterolateral, and posterolateral portal, are then inserted into the compartment and provide access to arthroscopic instrument for resection osteoplasty (see Figure 2-10 below).

During the procedure, multiple fluoroscopic images of the surgical site are required for surgeon's evaluation before, during, and after bony resection (Byrd, 2005; Larson and Wulf, 2009). While the arthroscopic technique is less invasive and promises quicker recovery, over- or under-resection is likely to occur because it is difficult to intra-operatively assess the resection depth due to the two-dimensional yet regional visualization (Ilizaliturri, Jr., 2009; Larson and Wulf, 2009; Mardones et al., 2009;

Matsuda, 2009). In addition, over-resection can lead to femoral neck fracture, and under-resection can lead to residual impingement and may require a revision arthroscopy (Mardones et al., 2005; Heyworth et al., 2007; Philippon et al., 2007b). Therefore, arthroscopic management of FAI remains technically demanding and depends on the surgeon's level of experience (Mardones et al., 2009; Matsuda, 2009).
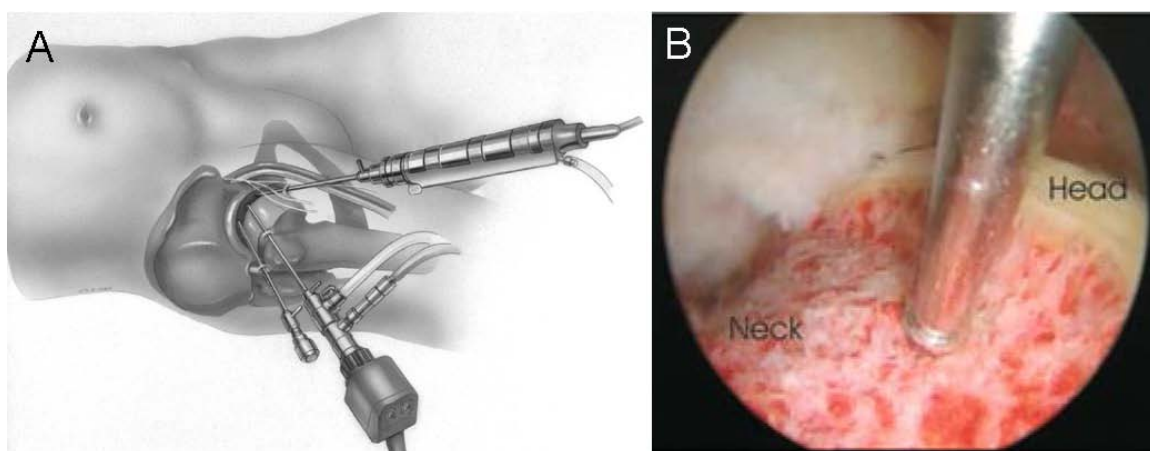
Figure 2-10: A) Portal placement for hip arthroscopy in supine position (Byrd, 2005). B) Picture of hip arthroscopy in a patient with cam FAI (Horisberger et al., 2010).

2.3 ROBOTIC SURGERY IN ORTHOPEDICS

Robotic surgery has been an emerging technology in the field of medicine. It provides surgeons with the ability to perform minimal invasive procedures accurately and reproducibly without the limitation of human hand and direct visualization. The earliest use of robotics in surgery dates back to 1985. Kwoh et al. (Kwoh et al., 1988) used an industrial robot to perform biopsy for neurosurgery. As technology has rapidly advanced, robotic surgery has been used for different applications (see details in Table 2-1) and some systems have been commercialized, such as the de Vinci Surgical System (Intuitive Surgical Inc, Mountain View, CA) for prostate cancer, hysterectomy, and mitral valve repair, and the Sensei Robotic Catheter System (Hansen Medical, Mountain View, CA) for cardiovascular procedures.

Table 2-1: Applications of robotic surgery (Lanfranco et al., 2004).

Orthopedic surgery	Neurosurgery	Gynecologic surgery	Cardiothoracic surgery	Urology	General surgery
Total hip arthroplasty: femur preparation	Complement image-guided-surgery	Tubal re-anastomosis	Mammary artery harvest	Radical prostatectomy	Cholecystectomy
Total hip arthroplasty: acetabular cup placement	Radiosurgery	Hysterectomies	CABG	Ureter repair	Nissen fundoplication
Knee surgery		Ovary resection	Mitral valve repair	Nephrectomy	Heller myotomy
Spine surgery					Gastric bypass
					Adrenalectomy
					Bowel resection
					Esophagectomy

Due to the recently evolvement of imaging technology and the rigid nature of bone, robotics in orthopedic procedures has become promising. For a period of time, orthopedic surgeons have performed surgeries based on their intuition, instinct, experience, and surgical skill (Dorr and Deshmane, 2009). In joint replacement surgery,

accurate bone preparation for precision implant placement is one of the most important maneuvers to prevent mechanical complications and increase the implant longevity. Robot-assisted surgery ensures correct bone removal and eliminates the manual error of bone preparation caused by human factors. As shown in Figure 2-11, the first surgical robot which US Food and Drug Administration (FDA) approved was ROBODOC (Integrated Surgical Systems, Davis, CA). It was designed to prepare the femur for total hip arthroplasty and first used with human patients in 1991. Since the introduction of ROBODOC, many robotic system for orthopedics have been developed, including ACROBOT (Acrobot Co Ltd, London, UK), a six degree-of-freedom robot constraining the surgeon to cut within predefined safety zone for unicompartmental and total knee arthroplasty; BRIGI Bone Resection Instrument Guide (Zimmer, Inc., Warsaw, IN), an imageless system with a positioning arm assisting the surgeon in placing the bone cutting guide for total knee arthroplasty; CASPAR (Ortho-Maquest/URS, Schwerin, Germany), an image-guided robotic system used for total hip arthroplasty and total knee arthroplasty; iBLOCK (PRAXIM, East Taunton, MA), a miniature bone-mounted robot with automatically positioned cutting guide for total knee arthroplasty; and PI GALILEO ACCULIGN (Smith & Nephew, London, UK), a system with two motorized joints to navigate and position a cutting guide for total knee arthroplasty (Adili, 2004; Bargar, 2007; Hagag et al., 2010).

Figure 2-11 Photograph of the ROBODOC system (Bargar, 2007).

In addition, Robotic Arm Interactive Orthopedic System (RIO, MAKO Surgical Corp., Fort Lauderdale, FL) has been commercialized and widely used in practical applications. The RIO surgical system, as can be seen in Figure 2-12, is a six degree-of-freedom robot, which features haptic force feedback and provides the surgeon with intuitive tactile feedback during human-machine interaction. The system consists of three major hardware components: a robotic arm, a camera stand, and a guidance module. The robotic arm is attached with a cutting system and interactively guides the surgeon to create desired resections of bone. The camera stand supports both a computer monitor which provides operative information for the surgeon, and a digital tracking camera

system which tracks the patient's anatomy. The guidance module functions as a control console. It is operated by an assistant or a technician to assist the surgeon through the procedure.
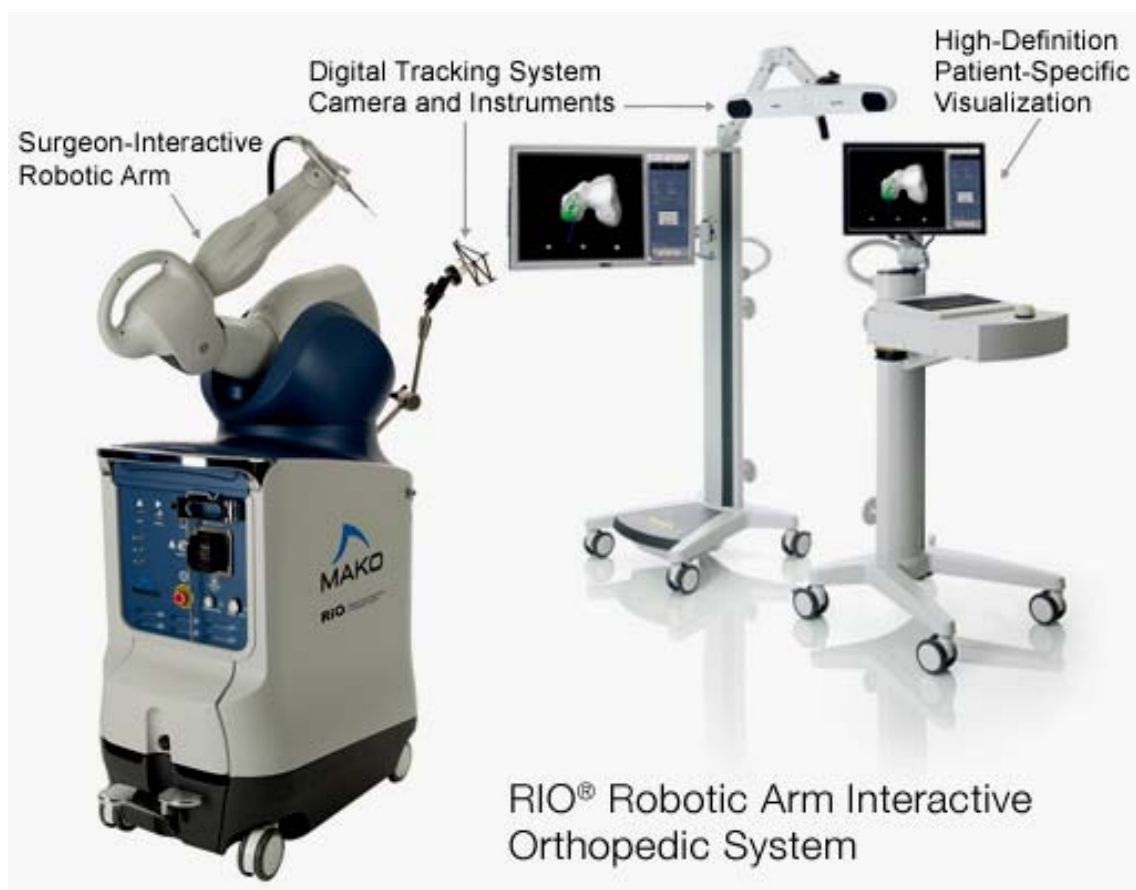
Figure 2-12: MAKO RIO Robotic Arm Interactive Orthopedic system (Copyright MAKO Surgical Corp. Picture retrieved June 19, 2011, from http://www.makosurgical.com/site/index.php/physicians/products/rio-robotic-arm/).

The surgical procedures and techniques of using the RIO surgical system are described as follows. For all patients, pre-operative CT scans covering specific anatomical landmarks in proper slice thickness are firstly obtained. The scans are saved in Digital Imaging and Communications in Medicine (DICOM) format and transferred to the RIO system. These images are then segmented in the software to generate 3D bone surface models in the stereolithography (STL) format. Next, the implant models and the bone models are displayed on the computer monitor, which allows the surgeon to virtually position the implant on the bone model and create patient-specific pre-operative planning (see Figure 2-13 below). The system provides the information of component alignment and kinematics for the surgeon to define the optimal implant position. Prior to the operation, the system has been positioned based on the operative anatomy and surgeon's preference.

At the beginning of the procedure, the patient's operative site undergoes conventional positioning and sterile draping. Then the robot is calibrated and tracking arrays are attached to the patient's operative anatomy. Initial registration is performed before the incision by registering the anatomical surface landmarks to the corresponding locations on the CT images. After the incision, the bone models are registered by using tracking probes to collect data points directly on the bone surfaces, as shown in Figure 2-14. These data points are then matched with the CT model. The registration transform for the optimal matching is returned.
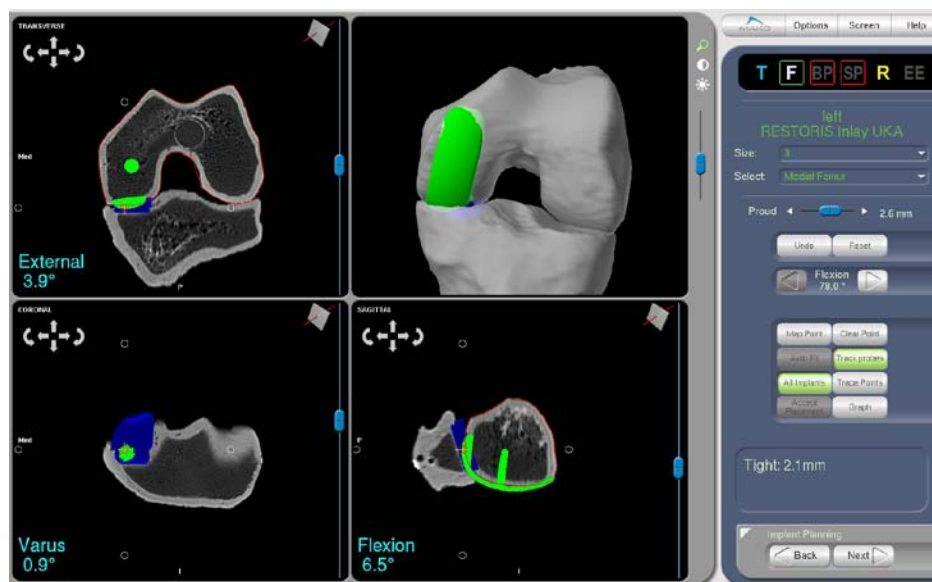
Figure 2-13: The CT-based patient specific pre-operative planning from MAKO RIO system (Hagag et al., 2010).

Figure 2-14: Bone registration is performed by using a tracking probe to collect data points directly on the bone surface (Copyright. Picture retrieved June 19, 2011, from http://www.texashealth.org/body.cfm?id=4169).

An interchangeable cutting instrument, such as a high-speed burr or a router, is attached to the end of the robotic arm. As shown in Figure 2-15, during the bone resection, the robotic arm can be moved freely by the surgeon as long as the tip of the cutting tool is within the pre-defined boundary. If the end effector is beyond the boundary, the arm resists the movement and restricts the tip inside the boundary with tactile force feedback. With the assistant of the robotic arm, the surgeon resects the bones by following the pre-operative plan, resulting in cavities which accurately match the shapes of the implants. The implants are then placed and cemented to the cavities and the surgical site is sutured.

Figure 2-15: Photography of MAKO RIO system used in operating room (Copyright Gray Whitley. Picture retrieved June 19, 2011, from http://www.flickr.com/photos/gray_whitley/5439904479/).

RIO system has been in widespread use for unicompartmental knee arthroplasty (UKA) in the US. Investigators (Coon et al., 2008; Roche et al., 2008; Sinha et al., 2008; Hagag et al., 2010; Lonner et al., 2010; Pearle et al., 2010) have also published its clinical results. They report that UKA using the robotic arm can result in accurate and precise reconstruction of patient's anatomy as well as low complications (see Figure 2-16 for details). Furthermore, compared with the standard manual technique, robotically guided UKA can lead to better bone preservation and improved clinical outcomes.
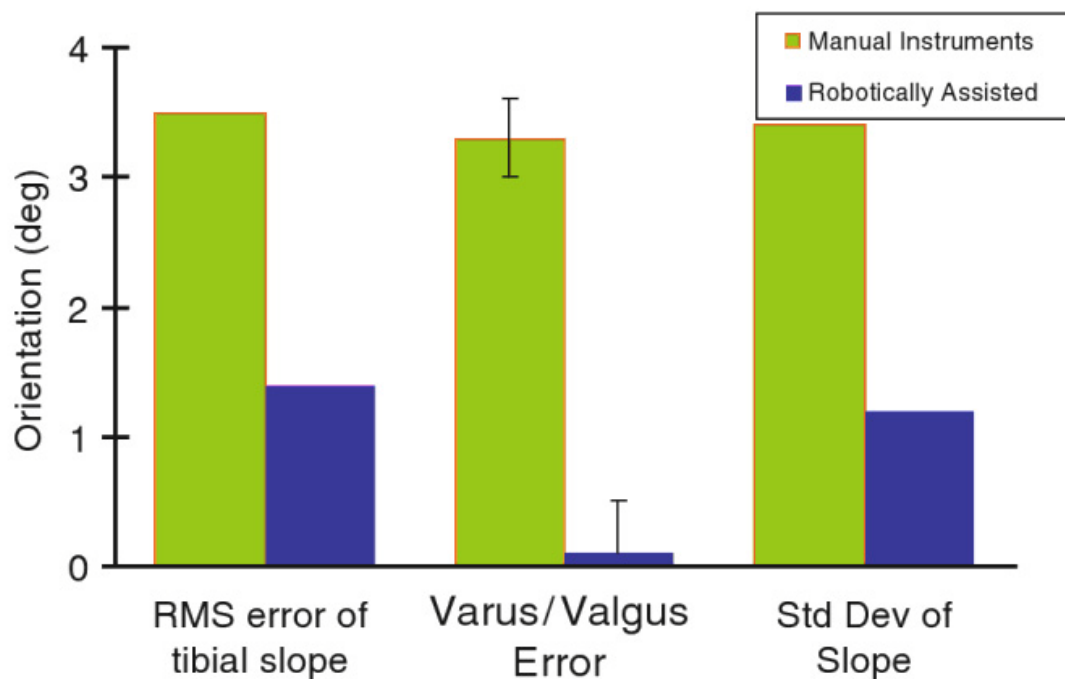
Figure 2-16: Comparison of the tibial slope error and variance between the manual and robot-assisted UKA (Coon et al., 2008; Hagag et al., 2010).

CHAPTER 3

A-MODE ULTRASOUND CALIBRATION

In this chapter, an enhanced calibration method for an A-mode US probe designed for noninvasive bone registration in robot-assisted FAI arthroscopy is described. The A-mode US probe is custom made and is intended to replace the conventional mechanical probes used for bone registration. The accuracy and robustness of the calibration method are also investigated. It is hoped that with successful calibration, registration errors are reduced. Thus accurate and minimally invasive bone registration can be achieved.

This chapter is structured as follows. It begins with a brief introduction and background review of A-mode US registration, followed by a discussion of the configuration and 3D transformation (see Appendix A) of the US system. Next, the calibration method and the experiment protocol are described. Finally, the result of the accuracy and robustness of the calibrated US probe are presented.

3.1 INTRODUCTORY REMARKS

The goal of robot-assisted orthopedic surgery in FAI arthroscopy is to provide minimal invasiveness and precision bone resection. In robot-assisted orthopedic surgery, the system establishes three 3D Cartesian coordinate spaces, namely "camera space," "anatomic space," and "image space." Camera space is the coordinate system created by the tracking system. Anatomic space is the coordinate system of the patient's surgical region. Image space is the coordinate system of the CT images and the bone surface

32

model. Registration links the therapeutic object (the anatomical feature of the surgical site) in camera space and the virtual object (the surface model) in image space. An accurate registration is critical because it is required for the system to provide the intra-operative details to the surgeon about how the surgery is being executed on the actual anatomy (Hufner et al., 2003; Ma and Ellis, 2003).

Conventional registration methods for robot-assisted orthopedic surgery are usually referred to point-based and surface-based registrations (Sugano et al., 2001; Amiot and Poulin, 2004; Docquier et al., 2009). Point-based registration, or point-pair registration, usually involves attaching fixed landmarks on skin surface or implanting bone-implanted fiducial markers prior to the surgery. In the intra-operative stage, point-based registration is achieved by using a tracked probe to poke the fiducial markers and collect data points. These points are then matched with the corresponding points in the pre-operative CT or MRI scans and yield a registration transform, which provides a linkage between the camera space and image space. However, one of the drawbacks of the point-based registration is that the pre-operative fiducial attachments limit the patient's freedom of daily activities. They also require extra incision and therefore increase the chance of infection.

Surface-based registration, also called surface matching registration, takes advantage of optimization routines, e.g., iterative closest point (ICP) algorithm (Besl and Mckay, 1992), and does not require pre-operative fiducial implantation. The registration is performed intra-operatively by using a tracked mechanical probe directly touching the surgically exposed bone surface to collect data points. These points are then best-fit with the surface models segmented from the pre-operative CT scans and yield the registration

transform. However, surface-based registration usually requires extensive incisions in order to directly access the bone surface. This approach may not be ideal for FAI arthroscopic surgery because of the limited bone access area. Therefore, a noninvasive bone registration method is highly desired.

US techniques have been proposed as a possible solution to achieve noninvasive bone registration (Kozak et al., 2002; Amin et al., 2003; Kowal et al., 2007). According to the principle of speed of sound, US waves propagate through mediums with different densities at different speeds (Luwig, 1950). When US waves reach the border of two mediums with different densities, a reflection signal is generated. Therefore, if the speed of sound of a homogenous medium A is known, the distance from the US transducer origin to the border between mediums A and B can be calculated by detecting the reflection signal and measuring the traveling time of the US waves.

A-mode US has been suggested as a feasible approach for bone registration in different applications, such as hip (Heger et al., 2005; Heger et al., 2007; Oszwald et al., 2008), skull (Amstutz et al., 2003; Fieten et al., 2009), spine (Moulder et al., 2003), and knee (Mozes et al., 2010). An A-mode US transducer attached to an optically tracked probe yields accurate measurement of bone surface points noninvasively. The advantages of using A-mode US includes that it emits a one-dimensional US beam and can be interpreted as a direct distance measurement, which can be utilized in the same manner as a mechanical probe. Therefore, an A-mode US probe can be easily integrated to a robot-assisted surgical system with slightly modification. Furthermore, the A-modes US signal is less complicated and requires less efforts for signal processing than the two-

dimensional US image (e.g., B-mode US). A-mode US is also relatively inexpensive compared with other image modalities such as CT or MRI.

US calibration has been addressed as an important issue for freehand 3D US systems, and different calibration methods have been proposed (Mercier et al., 2005). Successful calibration has also been indicated that it can greatly reduce the errors caused by the acoustic variation of soft tissue and geometric difference between US signal and physical location (Barratt et al., 2001; Barratt et al., 2006). However, at the time of writing, limited information has been described regarding A-mode US calibration for robot-assisted orthopedic surgery.

In this chapter, an enhanced calibration method using an A-mode US probe with a 3D optical tracking system is investigated. The A-mode US probe was custom made and intended to replace the conventional mechanical probes. We investigated our calibration method in terms of accuracy and robustness. With our approach, the A-mode US probe could be successfully calibrated and the registration errors could be minimized. Thus, accurate and minimal invasive bone registration for robot-assisted FAI arthroscopy could be achieved.

3.2 MATERIALS AND METHODS

Three major tasks were completed in order to demonstrate a robust calibration method for A-mode US bone registration. First, the pre-developed A-mode US bone registration system (Mozes et al., 2010) was set up, which consists of an A-mode US probe and an optical tracking system based on a commercial available robot-assisted

orthopedic surgical system. With the US registration system, the position and orientation of the US probe in space as well as the 3D coordinate of the surface point on an object were obtained. Next, in order to minimize the registration error, a method to calibrate the location of the transmitting/sensing element inside the US transducer housing was developed. Finally, the US calibration was repeated five times and the robustness of the calibration method was evaluated.

As shown in Figure 3-1, RIO Robotic Arm Interactive Orthopedic System (MAKO Surgical Corp., Fort Lauderdale, FL) was utilized for this study. The robotic system was equipped with a personal computer (PC) (Precision T5400, Dell Inc., Round Rock, TX) with Linux operating system (Red Hat Enterprise Linux 5.3, Red Hat Inc., Raleigh, NC), and a passive 3D optical tracking system, Polaris Spectra (Northern Digital Inc., Waterloo, Ontario, Canada), with an accuracy of 0.25 mm root mean square (RMS) error. The tracking system continuously monitored optical tracking markers and returned the positions and orientations of the markers in space. Each optical marker was attached with infrared reflective spheres (11.5 mm in diameter) arranged in a unique pattern (see Figure 3-2 below). The tracking system therefore distinguished each individual marker and returned the spatial information of the marker origin based on this specific pattern.
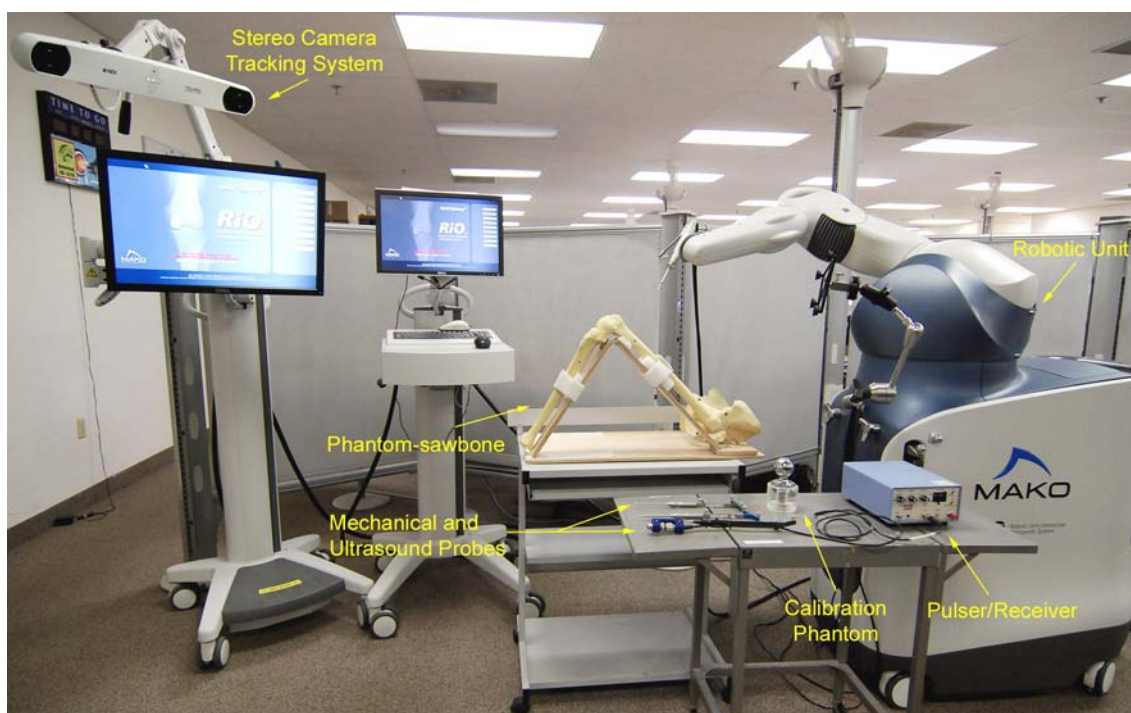
Figure 3-1: Photograph of the A-mode ultrasound registration system used in the present study.

Marker Origin

Figure 3-2: Picture of a mechanical probe. Three reflective spheres are attached in a unique pattern and form an optical marker.

Three 3D Cartesian coordinate spaces (in the unit of mm) were established by the system: namely camera space, anatomic space, and image space. The RIO software navigation platform (MAKO Surgical Corp., Fort Lauderdale, FL) integrated the spatial information of the optical tracking markers in camera space, the patient's surgical site information in anatomic space, and the virtual bone model information in image space.

A 10 MHz spherically focused A-mode US immersion transducer (Panametrics-NDT V312-SU, Olympus NDT Inc., MA) was used for this study. The US element size was 6 mm and the point target focus length was 25 mm. The transducer was powered by a US pulser-receiver (Panametrics-NDT 5072PR, Olympus NDT Inc., MA) with 9 MHz pulse frequency and 0.42 mm axial resolution. The pulser-receiver was connected to an 8 bit, 50 MHz sampling rate A/D acquisition card (ATS850, AlazarTech, Pointe-Claire, QC, Canada), which was installed in the PC for US signal digitization.

The US transducer received the electric signals from the pulser-receiver and converted the signals to sound waves. The sound waves propagated through the medium and generated reflected signals once they reached the boundary of two mediums with different densities. The reflected signals traveled back for the same distance and were detected by the pulser-receiver. The distance from the US transducer to the reflective surface boundary was calculated according to the time-of-flight equation:

$$d = v\frac{t}{2}$$

(3-1)

where d is the distance from the transducer to the reflective surface boundary; v is the speed of sound in the medium; and t is the time delay between the emitted and received pulses.

Custom software, as shown in Figure 3-3, was written in Tcl/Tk providing the graphical user interface (GUI) for the US calibration. In order to correctly measure the location of the reflective surface boundary, a dynamic processing window with adjustable width was created (see Figure 3-4). With the window, the signal was processed by a simple threshold filter. The peak of the reflected signal within the window was automatically detected. If the amplitude of the peak was larger than a pre-defined threshold, then the peak was determined to be the reflection of the target surface. By using equation 3-1, the surface reflection signal could then be converted into the US distance (d_{US}), which was from the transducer to the surface reflection.

The A-mode US probe was made by attaching the US transducer to the tip of a mechanical probe. The US transducer was carefully fixed on the probe. The direction of the US beam was aligned to the long axis of the mechanical probe, which was the z-axis of the coordinate system of the probe in probe space, as illustrated in Figure 3-5. The measured US distance was therefore a length extension in z-axis of the probe.
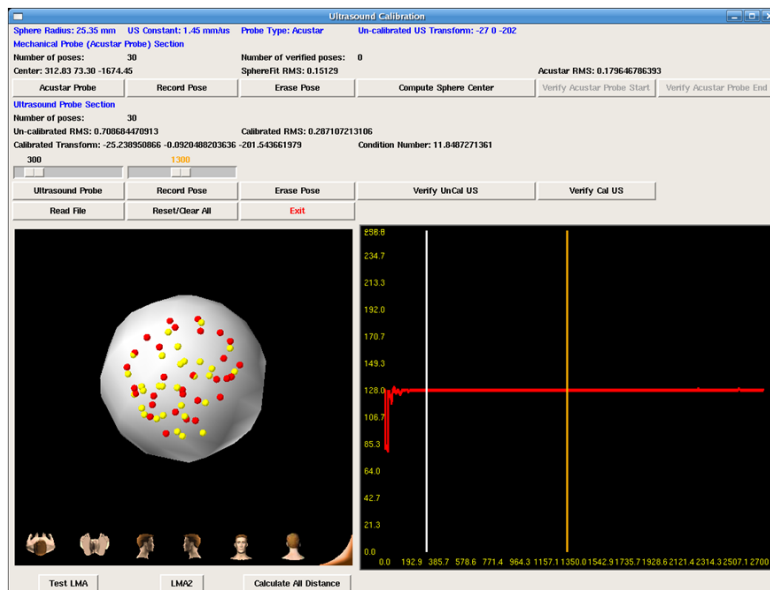
Figure 3-3: Picture of the US calibration software.
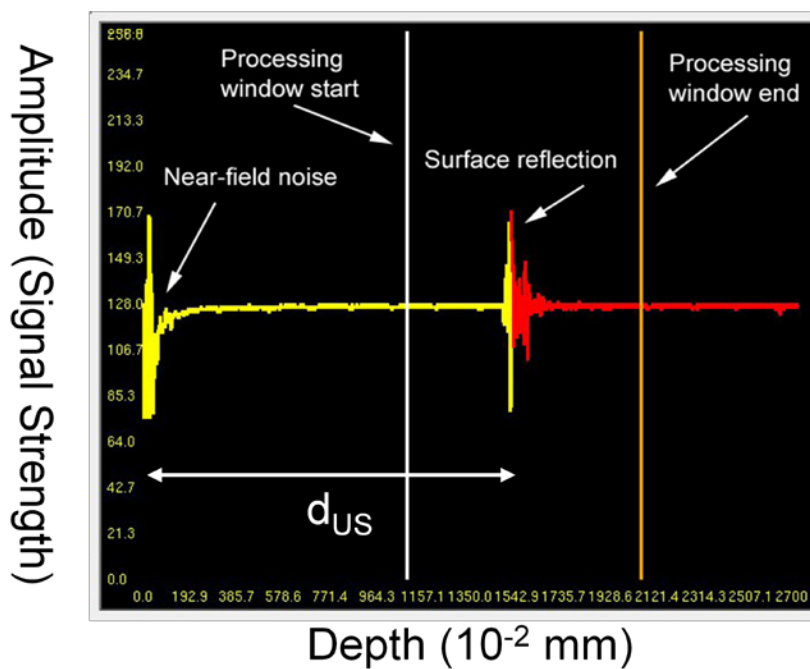
Figure 3-4: Illustration of an A-mode US signal. The yellow line represents the captured signal, which is used to calculate the distance from the US transducer to the surface reflection.

Figure 3-5: A-mode US probe was made by attaching the US transducer to the tip of a mechanical probe along the long axis.

Theoretically, the US transducer had to be positioned as perpendicular as possible to the reflection surface in order to achieve the maximum strength of the reflected signal. To address this issue, a stainless steel sphere phantom (25.35 mm in radius) was used in the present study. The nature of the spherical surface ensured that the strong reflected signal occurred only when the US beam was perpendicular to the reflection surface. The sphere phantom was submerged into water bath, which was selected as the US propagation medium (US speed constant: 1450 m/s in water and 1540 m/s in soft tissue (Luwig, 1950) because of its uniform density and easy accessibility.

3D data points on the sphere phantom surface were collected by using the US probe pointing to the phantom. The coordinate of a surface point in image space was computed through a series of transforms, as illustrated in Figure 3-6. First, the navigation system established the transform $T_{Camera-To-Image}$ from the optical tracking system in camera space to the model in the computer in image space. In this study, the surface

model of the phantom and all the surface points were generated and processed in camera space, so that the transform $T_{Camera-To-Image}$ became an identity transform. Secondly, as described earlier, the US probe was designed by attaching the US transducer aligned with the z-axis of the probe coordinate system in probe space. When the US probe marker was detected by the camera, the spatial information of the probe was returned by the transform $T_{Marker-To-Camera}$. Thirdly, the transformation from the transducer head to the US probe marker origin in probe space could be described as the transform $T_{Transducer-To-Marker}$, which was simply a translational offset $[T_x \quad T_y \quad T_z]$ measured by a coordinate measurement machine (CMM). Next, while the US distance from the transducer to the reflection surface d_{US} was measured, transform $T_{Surface-To-Transducer}$ was yielded and could be described as $[0 \quad 0 \quad d_{US}]$ since the offset d was in the z-axis direction. By above transforms, the transformation from the surface point P to the US probe marker in probe space could be derived as:

$$T_{Surface-To-Marker} = T_{Surface-To-Transducer} \times T_{Transducer-To-Marker}$$

(3-2)

The translational offset from the surface point to the marker origin then became $[T_x \quad T_y \quad T_z + d_{US}]$. Finally, the coordinate of the surface point in image space could be computed as:

$$\left(P_x, P_y, P_z\right)_{Image} = \left(P_x, P_y, P_z\right)_{Probe} \times T_{Surface-To-Marker}$$

$$\times T_{Marker-To-Camera} \times T_{Camera-To-Image}$$

(3-3)
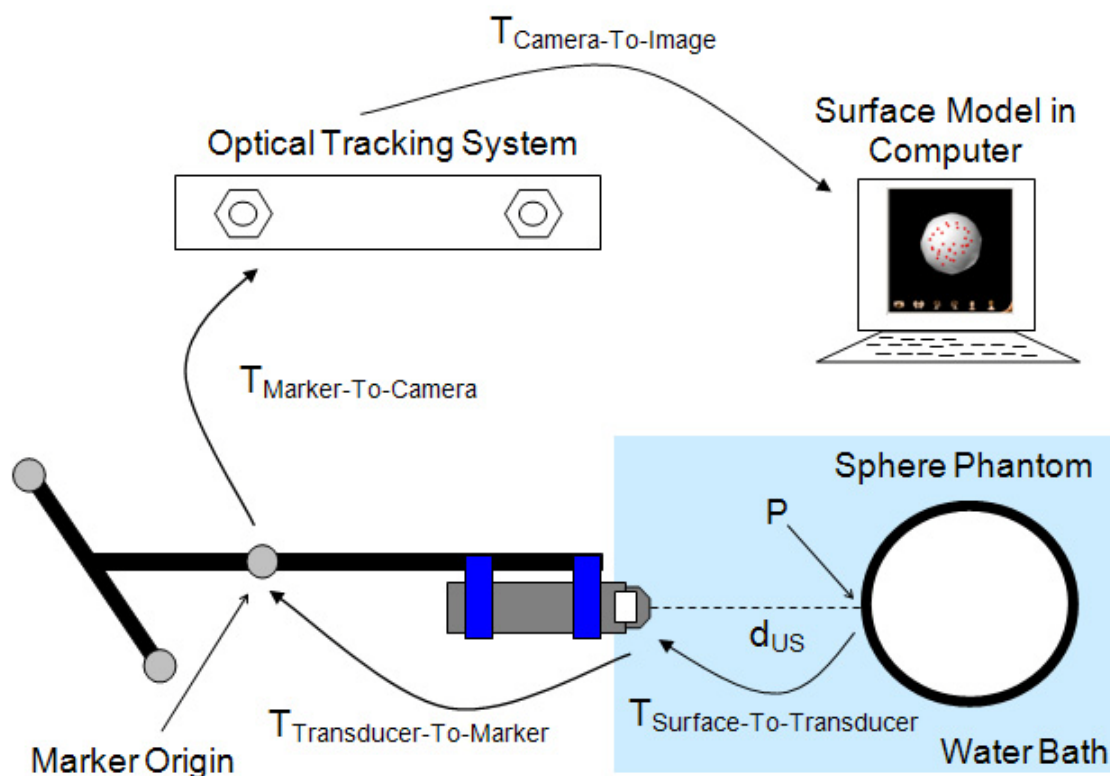
Figure 3-6: Illustration of the 3D transformation of the A-mode US calibration. The position of the phantom surface point in image space is calculated through a series of transforms.

In the present study, the goal of the A-mode US calibration is to find the small distance difference between the location of the transmitting/sensing element inside the US transducer housing and the US transducer head, as illustrated in Figure 3-7. A nonlinear least-squares optimization algorithm, Levenberg–Marquardt algorithm (LMA) (Levenberg, 1944; Marquardt, 1963), was implemented for the US calibration.

The calibration method is briefly described as follows. By knowing the coordinate of the tracked marker origin (O_x, O_y, O_z), the surface point (P_x, P_y, P_z) could be calculated as:

$$(P_x, P_y, P_z) = (O_x, O_y, O_z) \times T_{Transducer-To-Mar\,ker} \times [0 \quad 0 \quad d_{US}]$$ (3-4)

For each surface point (P_{xi}, P_{yi}, P_{zi}), the distance D_i from the sphere center (C_x, C_y, C_z) to the surface point was described as:

$$D_i = \sqrt{(P_{xi} - C_x)^2 + (P_{yi} - C_y)^2 + (P_{zi} - C_z)^2}$$ (3-5)

The distance error E_i of each surface point was calculated as the difference between the measured sphere radius r and the D_i:

$$E_i = r - D_i$$ (3-6)

The initial $T_{Transducer-To-Mar\,ker}$ transform was measured as the translational offset $[T_x \quad T_y \quad T_z]$ from the US transducer head to the marker origin by the CMM. The LMA applied a small difference $[\delta_x \quad \delta_y \quad \delta_z]$ to the measured $T_{Transducer-To-Mar\,ker}$ transform, so that the measured $T_{Transducer-To-Mar\,ker}$ became $[T_x + \delta_x \quad T_y + \delta_y \quad T_z + \delta_z]$. The LMA then continuously changed the value of the small difference to minimize the total distance error E. This iterative process yielded an optimized $T_{Transducer-To-Mar\,ker}$ transform, which represented the calibrated location of the transmitting/sensing element inside the US transducer housing. A detailed mathematical derivation of the US calibration with LMA is described in Appendix B.
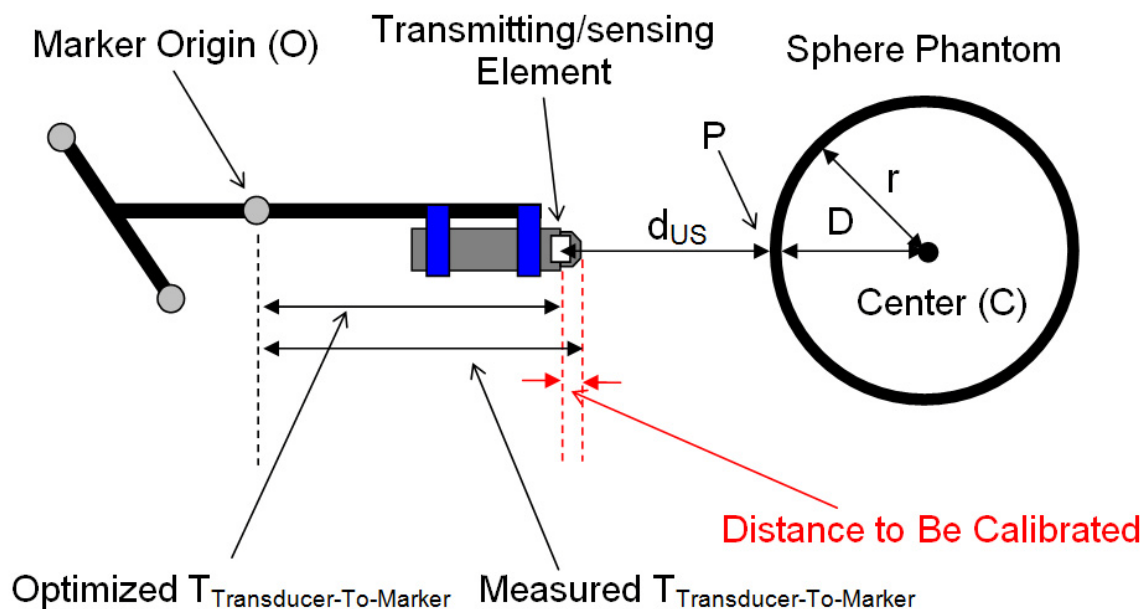
Figure 3-7: Illustration of the US probe calibration. The location of the transmitting/sensing element inside the US transducer housing is calibrated using the Levenberg-Marquardt algorithm.

The US calibration consisted of four steps. Since the center of the sphere was untouchable, the first step of calibration was to determine it. During the calibration, the sphere phantom had to be remained at the same position because there was no optical marker on the phantom providing the phantom's spatial information. 30 surface points were randomly collected by using the mechanical probe. The center of the sphere phantom was then computed based on the collected surface points using the least-squares sphere fitting algorithm. The calculated center was assumed as the gold standard through the calibration process. The accuracy of the sphere fitting could be described as the RMS error yielded by the algorithm as the equation:

$$RMS = \sqrt{\frac{\sum_{i=0}^{N}(D_i - r)^2}{N}}$$

(3-7)

where N is the number of the surface points; r is the measured radius of the sphere phantom (25.35 mm); and D_i is the distance from each surface point to the fitted center.

The second step of the calibration was to verify the accuracy of the mechanical probe itself. Same to the process defining the sphere center, 30 surface points were randomly collected by using the mechanical probe, and the RMS error was returned. Next, the accuracy of the un-calibrated US probe was verified by randomly collecting 30 surface points using the US probe. In order to capture satisfactory reflected signal, the US transducer was positioned as perpendicular as possible to the phantom surface. The US distance of the captured signal was calculated and the coordinate of the surface points were computed based on the measured $T_{Transducer-To-Mar\,ker}$ transform. These collected surface points then underwent sphere fitting and the RMS error of the un-calibrated US probe was yielded. Lastly, the LMA calibration was employed resulting in an optimized $T_{Transducer-To-Mar\,ker}$ transform. The RMS error of the calibrated US probe was then calculated with the optimized transform.

3.3 RESULTS

The initial $T_{Transducer-To-Mar\,ker}$ transform was measured by CMM as (-27 mm, 0 mm, -202 mm). The calibration process was repeated for totally five times. The results of the sphere fitting for defining the sphere center as well as the accuracy verification for the

mechanical probe are both shown in Table 1. The mean RMS error of sphere fitting was 0.14 mm with standard deviation 0.05 mm. The mean RMS error of mechanical probe accuracy verification was 0.20 mm with standard deviation 0.11mm.

Table 3-1: The results of the mechanical probe sphere fitting and accuracy verification (n = 30; SD = standard deviation).

Calibrations	Mechanical Probe	
	Sphere Fitting RMS Error (mm)	Accuracy Verification RMS Error (mm)
1	0.15	0.18
2	0.21	0.38
3	0.09	0.13
4	0.14	0.09
5	0.10	0.21
Mean	0.14	0.20
SD	0.05	0.11

The results of accuracy verification of the un-calibrated and calibrated US probe can be found in Table 3-2. The mean RMS error of the un-calibrated US probe was 0.75 mm with standard deviation 0.05 mm; the mean RMS error of the calibrated US probe was 0.40 mm with standard deviation 0.10 mm. An illustrated example of the US calibration result is displayed in Figure 3-8. The results of the optimized $T_{Transducer-To-Mar\ker}$ transforms are given in Table 3-3. The mean $T_{Transducer-To-Mar\ker}$ transform was (-27.34 mm, -0.03 mm, -201.36 mm).

Table 3-2: The results of the US probe accuracy before and after calibration (n = 30; SD = standard deviation).

Calibrations	Ultrasound Probe	
	Un-calibrated RMS Error (mm)	Calibrated RMS Error (mm)
1	0.71	0.33
2	0.76	0.36
3	0.69	0.40
4	0.83	0.35
5	0.75	0.58
Mean	0.75	0.40
SD	0.05	0.10
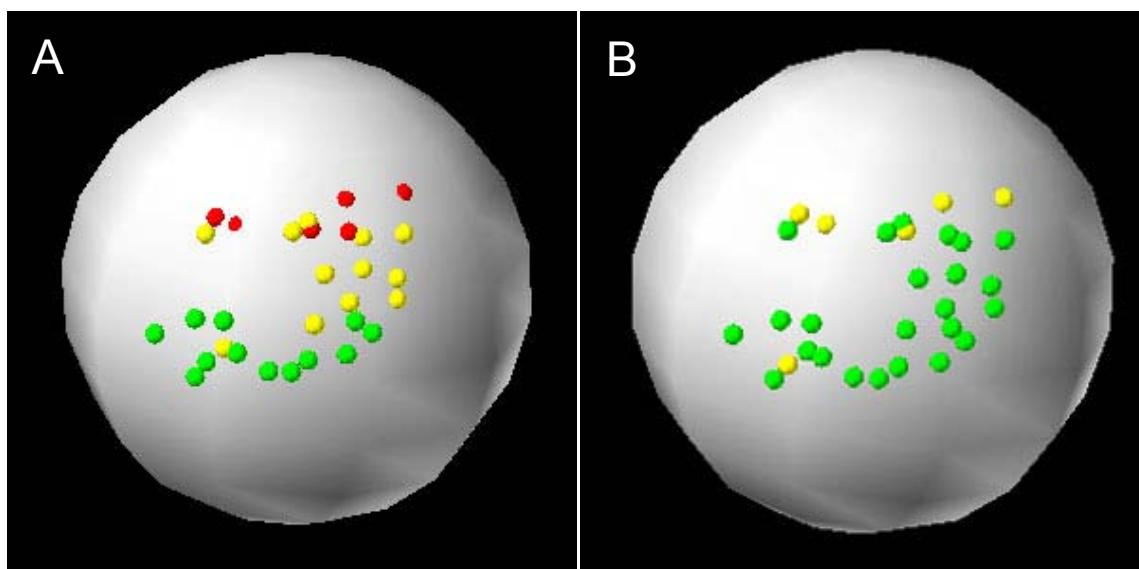
Figure 3-8: Picture of the first test result of the US probe calibration. A) The un-calibrated probe with RMS error of 0.71 mm. B) The calibrated US probe with RMS error of 0.33 mm. Green color represents the distance error < 0.5 mm; yellow represents the error between 0.5 mm and 1 mm; and red represents the error > 1 mm.

Table 3-3: The results of the optimized $T_{Transducer-To-Mar\ker}$ transforms of five calibrations.

Calibrations	$T_{Transducer-To-Mar\ker}$ Transform (mm)		
	T_X	T_Y	T_Z
Measured	-27	0	-202
1	-27.07	0.09	-201.38
2	-27.62	0.14	-201.29
3	-27.38	-0.17	-201.41
4	-27.49	-0.17	-201.23
5	-27.12	-0.02	-201.51
Mean	-27.34	-0.03	-201.36

3.4 DISCUSSION

Registration is a key step in robot-assisted FAI arthroscopic surgery. Conventional method for bone registration requires extensive incisions using mechanical probes. The A-mode US probe described in this chapter provides an alternative approach for noninvasive bone registration. To obtain an accurate registration by the US probe, a robust calibration is highly desirable.

Unlike the mechanical probes, which can be easily calibrated by measuring the physical 3D dimension, the US probe generates invisible sound wave and therefore it is difficult to obtain the 3D measurement directly. In addition, in order to correctly measure the US distance, the perpendicularity between the US signal and the reflection surface has to be guaranteed. In this study, a sphere phantom is used to ensure that the reflective signal is measured only when the perpendicular relationship is established. The center of the sphere phantom is chosen as the reference point for calibration, which is a fixed 3D coordinate but untouchable. The physical coordinate of the phantom center is determined

by a number of sampled data points on the sphere surface through a surface-fitting algorithm. The calibration of the A-mode US system is not complicated to perform and it allows sufficient accuracy (sub-millimeter level) for the registration process. While the system should be recalibrated for each operation clinically, the system has been proved to be robust enough to last through procedures.

A previous study has reported that the general registration RMS error for CAOS is between 0.5 mm to 5 mm (Barratt et al., 2006). Our results show that the RMS errors of the mechanical probe in all calibrations are better than the reported data. For the calibrated US probe, there is only one calibration (out of five measurements) has RMS error slightly over 0.5 mm, while the mean error is still better than the acceptable range. In addition, by comparing to the un-calibrated US probe, the US calibration greatly improves the sphere registration RMS error by 46%. The difference between the mean error of the mechanical probe and which of the calibrated US probe is 0.20 mm. It is considered to be acceptable since the calibrated US probe still results in the RMS error within the generally accepted range. The standard deviations of the mechanical probe and the calibrated US probe are close in value. This indicates that there might be a constant offset between the US probe and mechanical probe. With further calibration, the US probe can achieve the similar registration accuracy as the mechanical probe.

Ideally, the errors introduced by data sampling can be eliminated as long as the collected data points cover a large enough area of the sphere surface and the number of data points is large enough (30 in this study). However, the US probe has a smaller access area on the phantom surface than the mechanical probe in data point collection. This is due to the limitation of keeping a clear view between the camera and the optical marker

while maintaining the perpendicularity between the US transducer and the phantom surface at the same time. This might result in undesired errors and should be addressed in the future study.

Further improvements including US signal processing, a sphere phantom with optical markers, and various transducer selection will be applied. A custom designed adapter for fast surface point collecting is also under development and will be utilized in future experiments. In addition, the calibration method will be evaluated by performing bone registration with sawbones and cadaver specimens using the US probe.

In summary, this chapter presents an enhanced calibration method for an A-mode US probe, which is designed for noninvasive bone registration in robot-assisted FAI arthroscopy. The accuracy and robustness of the calibrated US probe are evaluated and both of them are within the acceptable range. With further modifications, the A-mode US probe is feasible for noninvasive bone registration and can be used to replace the conventional mechanical probes.

CHAPTER 4

REGISTRATION POINT-PATTERN SIMULATOR

A software-based bone registration point-pattern simulator for robot-assisted FAI arthroscopy is discussed in this chapter. A point-pattern consists of numbers of 3D data points arranged in a unique pattern. To facilitate following discussion, the phrase "point-pattern" specifically regards above mentioned 3D data points. During bone registration, the point-pattern provides the spatial information to the surgeon about where to collect the registration points on the bone surface. The purpose of this study presented in chapter 4 is to evaluate different registration point-patterns in terms of the resulting registration accuracy and consistency. The simulator simulates physical bone registration based on the surface-based ICP registration technique. A sawbone femur surface model is loaded into the simulator. Various point-patterns designed for FAI arthroscopy are registered to the bone model, and the registration accuracies are then assessed. The developed simulator can help the user to determine an optimized registration point-pattern for FAI arthroscopy.

This chapter starts with a brief introduction of the surface-based registration in FAI arthroscopy. The development of the registration simulator based on the ICP algorithm and Monte Carlo method is then described. Next, the processes of the bone model generation and the design of the registration point-patterns for FAI arthroscopy are presented. The experimental results of registering the point-patterns to the bone model with the developed simulator are finally discussed.

52

4.1 INTRODUCTORY REMARKS

In robot-assisted orthopedic surgery, registration establishes the relationship between the patient's anatomical feature and the 3D computer data set, so that guidance and predesigned procedures can be performed accurately. As mentioned previously in section 3.1, conventional registration methods are usually referred to point-based and surface-based registrations. Point-based registration requires a preliminary surgical procedure to place the fiducial markers on the bones of the patient. The patient is CT scanned and the location of the fiducial markers in image space is established. In the intra-operative stage, the surgeon "digitizes" these fiducial markers using a tracked mechanical probe to collect the location of the fiducial markers in camera space. A registration transform matrix is then calculated and then yielded by matching the coordinates of the fiducial markers in image space and those in camera space. However, the fiduciary approach is not minimally invasive because it requires an additional operation before the surgical procedure.

On the other hand, surface-based registration does not require pre-operative fiducial implantation. In the pre-operative stage, a virtual bone model is generated from segmented CT images and is stored in a computer. The registration is then performed intra-operatively by the surgeon using a tracked mechanical probe to directly touch the surgically exposed bone surface to collect data points. These points are then matched with the bone model based on a surface matching algorithm and a registration transform matrix is yielded.

One of the most commonly used surface registration techniques in robot-assisted surgery is the ICP algorithm, presented by Besl and McKay (Besl and Mckay, 1992). The

algorithm registers a data set digitized from an unfixtured rigid object to a 3D geometric model, and it is capable of handling different types of 3D shapes such as points, lines, curves, and triangles. The ICP algorithm converges to the nearest local minimum on the complex shapes in a least-squares manner. In short, by given the data set of the registration point cloud, the algorithm first finds the corresponding closest points on the surface of a given model. It then tries to match these two sets of points by applying a transformation matrix to the given point cloud, and yields a residual RMS error. The above processes are repeated by changing transformation parameter values iteratively until the change in RMS error falls below a pre-defined threshold. In this way, a final transformation matrix representing the optimal matching between the initial given point cloud and the 3D model is calculated. The flowchart of the ICP algorithm is illustrated in Figure 4-1.

In order to be minimally invasive, the digitized points for surface-based registration have to be limited to a small area near the surgical site that can be accessed by the mechanical probe. In addition, in order to minimize the registration time, the number of the digitized points has to be as small as possible but enough to result in acceptable registration accuracy. Therefore, during digitization, the data points are usually collected by following a specific "point-pattern" to achieve a satisfactory accuracy and an acceptable registration time period. During bone registration, the point-pattern provides the spatial information to the surgeon about where to digitize the registration points on the bone surface. The point-pattern is usually designed by arranging multiple 3D points based on the shape of the bone, and thus these points form a unique

pattern in space. In addition, the number of the points is the smaller the better in order to reduce the time for point digitization.
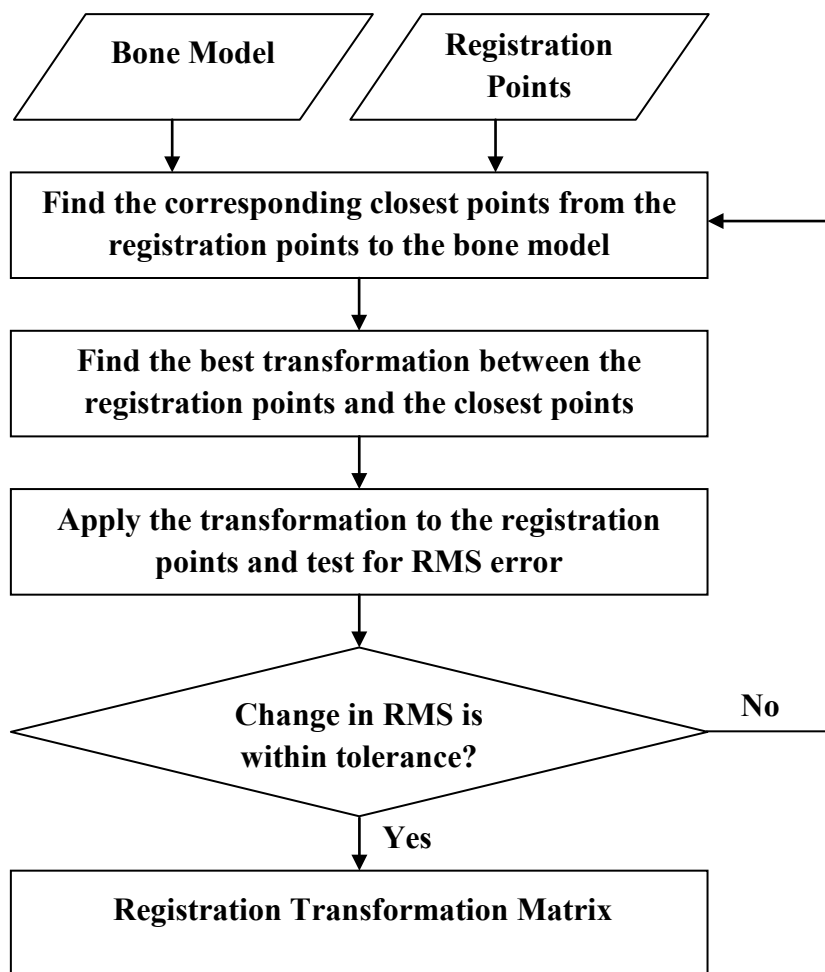
Figure 4-1: The flowchart of the ICP algorithm.

Arthroscopic technique has become increasingly popular for treating FAI with minor deformities. Arthroscopy is performed by the surgeon inserting multiple portals into the hip capsule. The arthroscopic instruments for resection osteoplasty are then inserted through the portals to access the surgical site. However, to keep the invasiveness of FAI arthroscopic procedure minimal, only very limited areas of the bone are accessible

for collecting registration points. Therefore, in order to get an idea of the registration accuracy resulted from the point-pattern designed for FAI arthroscopy, a registration point-pattern simulator is highly desired.

In this study, a surface-based registration simulator developed for evaluating the registration accuracy of a given registration point-pattern in robot-assisted FAI arthroscopy is discussed. The simulator accommodates different registration parameters and randomly generated noises to simulate the physical registration process. The accuracy of various point-patterns created with different point locations and number of points are tested with the simulator. In addition, the effect of perturbation by different parameters on registration is also discussed. The developed simulator not only provides the accuracy information for evaluating a designed point-pattern for FAI arthroscopy, but also can be used to determine an "optimized" point-pattern, which yields the best registration accuracy and requires only the minimal number of data points within the accessible areas.

4.2 MATERIALS AND METHODS

A registration point-pattern simulator was created by MATLAB (MathWorks, Natick, MA). The simulator took a bone model and a point-pattern as the inputs, and registered the data points generated based on the imported point-pattern to the bone model. The simulator also consisted of a GUI so that the user could enter and modify easily different registration parameters, as shown in Figure 4-2. The registration simulation could be described as five different steps, including a) data importing, b) point

digitization, c) initial registration, d) ICP registration with perturbed starting positions, and e) Monte Carlo simulation. These steps are explained later.
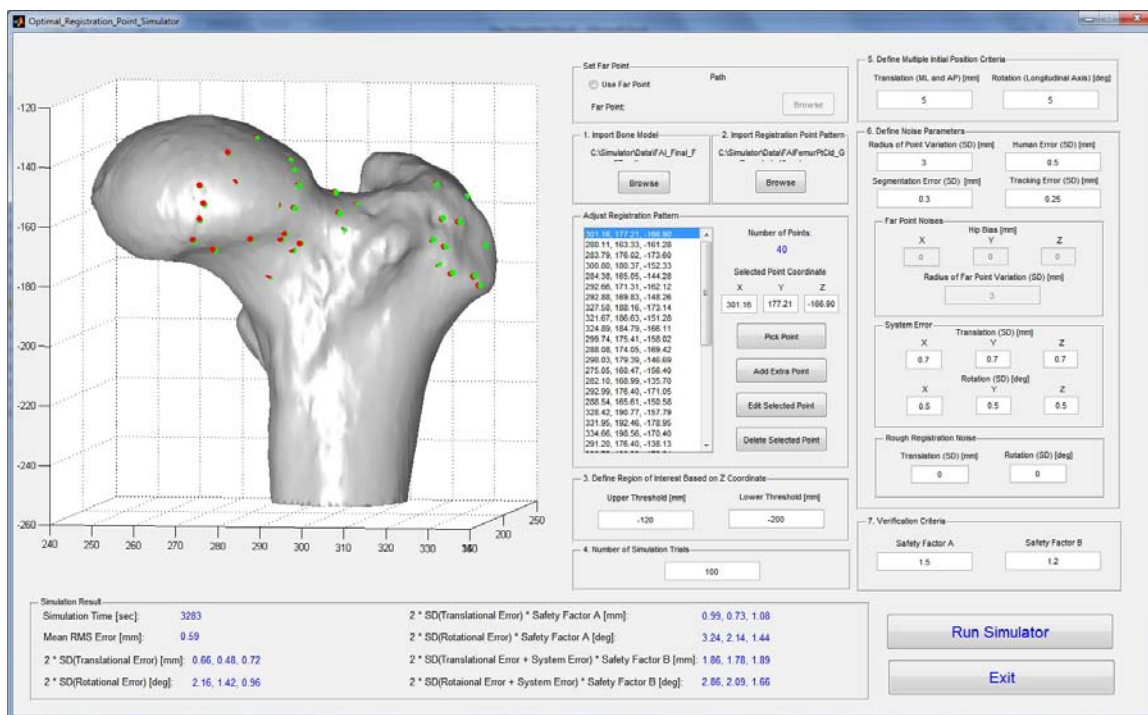
Figure 4-2: Picture of the registration point-pattern simulator.

The registration simulation began with importing a bone model and a point-pattern into the simulator. The simulator allowed the user to create or edit a point-pattern by digitizing the points directly on the surface of the bone model by moving and clicking the mouse cursor. In order to avoid the expensive computation on non-interested bone regions during the ICP registration, a region of interest (ROI) of the bone model was determined by the user. The ROI was defined as the region between an upper threshold and a lower threshold of the long axis (z-axis in this study) of the model.

Next, in order to simulate the physical process of point digitization, various registration noise parameters were defined. The first parameter was the "radius of point variation," which simulated the 3D error between the "should-be-digitized" location of the point defined by the point-pattern and the "real-digitized" location of the point collected by the user. The input value of the radius of point variation was defined as the standard deviation of a Gaussian noise in the unit of millimeter. The radius of point variation was then added to each point of the point-pattern, but in this way the noise-added points might not locate exactly on the surface of the bone model. To tackle this problem, the closest point on the model surface of each corresponding noise-added point was calculated.

Three other noise parameters were also defined to simulate the errors related to the point digitization, namely "human error," "segmentation error," and "tracking system error." These noises were 3D errors and the input values of them were also represented as the standard deviation of a Gaussian noise in the unit of millimeter. A combined noise of these three parameters was calculated as:

Combined Noise $=$

$$\sqrt{(\text{Human Error})^2 + (\text{Segmentation Error})^2 + (\text{Tracking System Error})^2} \quad (4\text{-}1)$$

This combined noise was then added to the previously calculated closest points. These noise-added closest points together formed the registration points, and the simulation of the point digitization was now completed.

As mentioned in section 4.1, the ICP algorithm converges to the local minimum of the cost function in a least-squares manner, i.e., the RMS error between the registration

points and the closest points. In the present study, the local minimum usually located on the 3D shape where closed to the starting position of the registration points. Hence, in order to find the global minimum, an initial registration that brought the registration points in camera space to the correct starting position in image space was needed before employing the ICP algorithm. The initial registration required at least three paired points, i.e., three points in camera space and three corresponding points in image space, to lock the 3D translation and rotation. By registering these two sets of paired points, a transformation matrix of the initial registration was calculated.

For the registration simulation, since the point-pattern was created based on the bone model, the registration points were already in a close starting position in image space for the ICP algorithm, and therefore the initial registration transform was an identity matrix. To simulate the errors from the initial registration, two noise parameters were determined to represent the translational error and rotational error. The input values of these two parameters were defined as the standard deviation of a Gaussian noise in the unit of millimeter. These two noises were applied to the initial registration transform, and the noise-added transform was then applied to the registration points generated from the point digitization.

Next, the ICP algorithm was employed by the registration simulation, and the steps were described as follows. 1) The algorithm searched the closest triangle facet on the surface of the bone model for each registration point; 2) The corresponding closest point from the closest facet for each registration point was found; 3) A rigid transformation matrix was computed by least-squares fitting the registration points and the closest points; 4) The registration points were then transformed by applying the

transformation matrix, and a residual RMS error between the transformed registration points and the closest points was also calculated; and 5) Steps 1 to 4 were iterated until the RMS error was below a pre-defined threshold value (i.e., 10^{-5} in this study).

To avoid the ICP algorithm converging to a local minimum, the starting position of the registration points was perturbed both in translation (δ) and rotation (θ) to eight different positions, as shown in Table 4-1. In this study, the coordinate system was defined as the x-axis pointing laterally, the y-axis pointing posteriorly, and the z-axis pointing superiorly. The perturbation scheme was designed to find the global minimal by perturbing the starting position around the z-axis. The ICP algorithm was then repeated with these eight starting positions plus the original starting position. Among these nine different starting positions, the one that results in the lowest RMS error was chosen, and the transformation matrix of this starting position was considered as the best solution.

Table 4-1: The eight different starting positions with translational perturbation of δ mm and rotational perturbation of θ degree.

Starting Positions	Translational Perturbation δ (mm)			Rotational Perturbation θ (Degree)		
	X-Axis	Y-Axis	Z-Axis	X-Axis	Y-Axis	Z-Axis
Original	0	0	0	0	0	0
Perturbation 1	- δ	- δ	0	0	0	θ
Perturbation 2	- δ	δ	0	0	0	θ
Perturbation 3	δ	- δ	0	0	0	θ
Perturbation 4	δ	δ	0	0	0	θ
Perturbation 5	- δ	- δ	0	0	0	- θ
Perturbation 6	- δ	δ	0	0	0	- θ
Perturbation 7	δ	- δ	0	0	0	- θ
Perturbation 8	δ	δ	0	0	0	- θ

In addition, because the registration simulation involved a lot of variables as well as the noises generated randomly in a Gaussian distribution, the Monte Carlo simulation (Metropolis and Ulam, 1949) was utilized in this study. The Monte Carlo method involves a large number of iterations of the registration procedures to simulate how the variables and noises affect the registration accuracy based on the given registration point-pattern. A flowchart of the registration simulation procedures is illustrated in Figure 4-3.

To evaluate the registration point-patterns using the developed simulator, a STL surface model of the left femur of a patient diagnosed with cam FAI was generated. The CT images scanned at 1 mm slice thickness were segmented to generate the model by using the commercial available segmentation software (Mimics 13.1, Materialise, Leuven, Belgium). Only the proximal portion (approximately 12 cm) of the femur was segmented because the access areas of FAI arthroscopy were limited to the proximal end of the femur.

As illustrated in Figure 4-4, three clinically determined access areas were identified by an experienced orthopedic surgeon specialized in FAI arthroscopy, namely the "direct-access" region, the "intermediate-access" region, and the "lateral" region. The direct-access region represented the area where the surgeon had a clear visualization directly from the arthroscope image. The intermediate-access region represented the area where the surgeon had a limited view and it required the surgeon to manipulate the arthroscope with extra efforts to get a clear view. Finally the lateral region represented the lateral portion of the proximal femur which could be reached by the surgeon by using a sharp probe poking on the bone percutaneously.
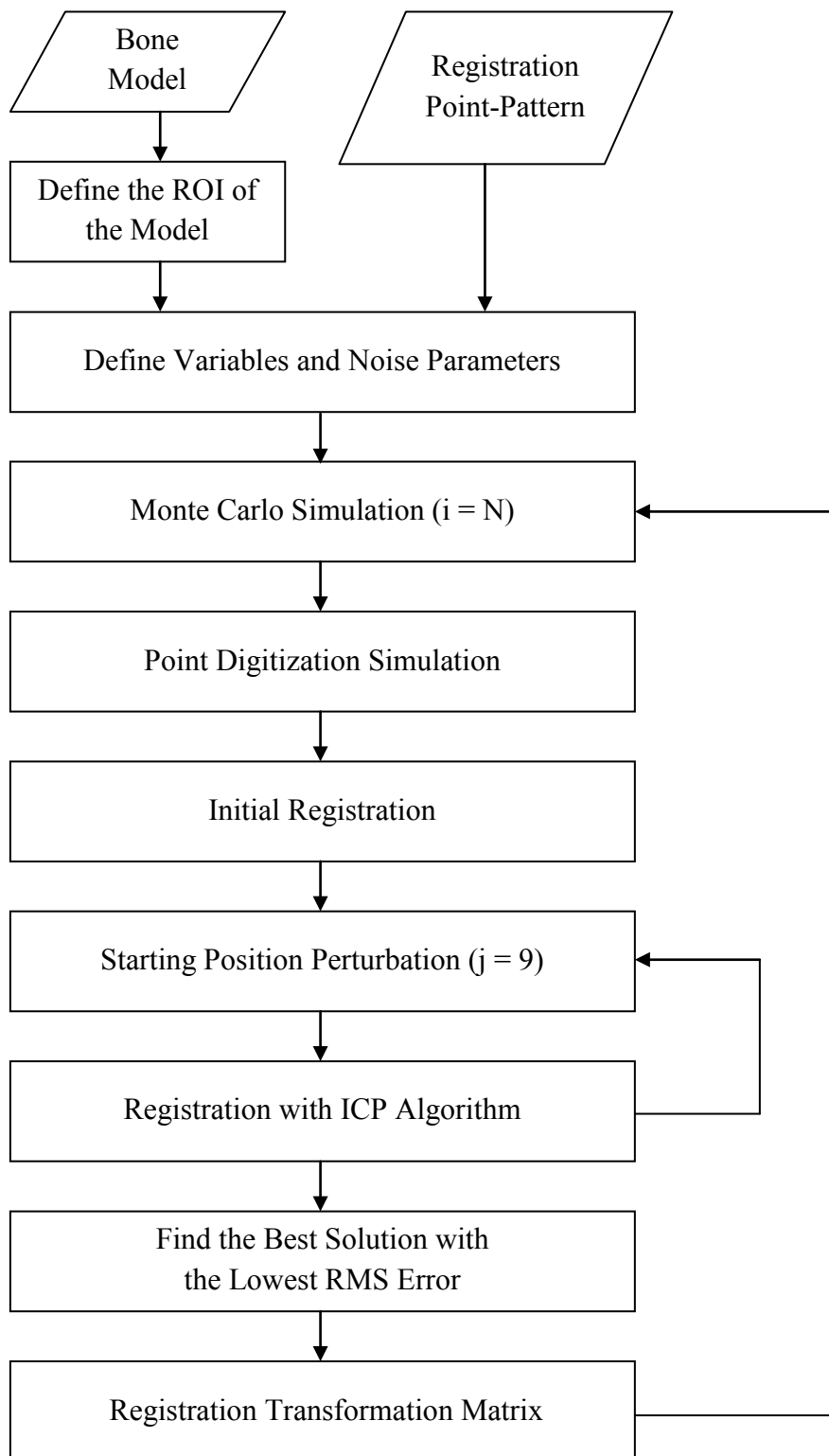
Figure 4-3: The flowchart of the registration simulation procedures.
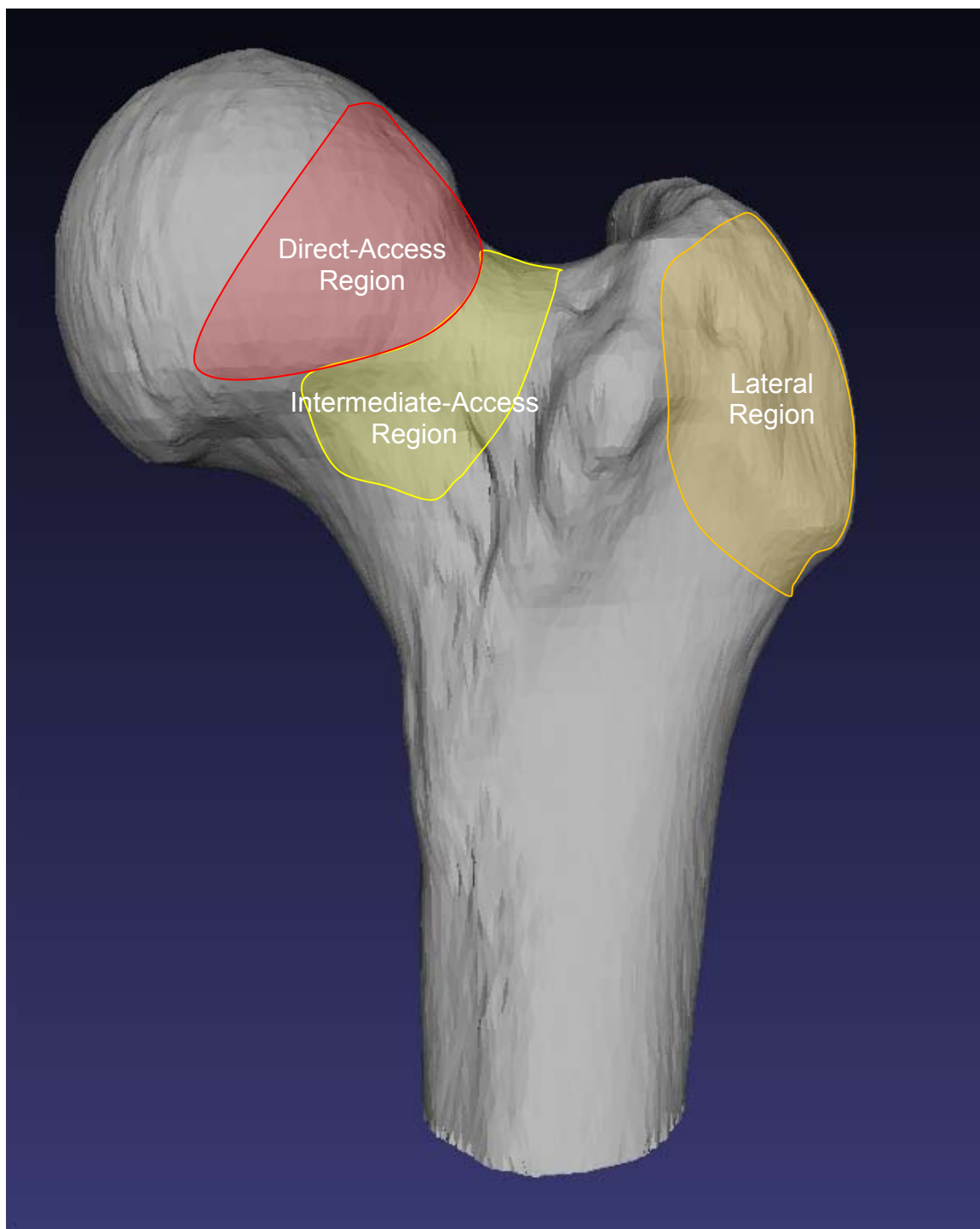
Figure 4-4: Illustration of the access areas of FAI arthroscopy.

Four different combinations of the access areas were designed to evaluate the corresponding registration accuracy, as illustrated in Figure 4-5. Each combination consisted of a point-pattern of 40 points. The first combination included the direct-access region only; the second combination included the direct-access region and the intermediate-access region; the third combination covered the direct-access region and the lateral region; and the fourth combination consisted of all the direct-access region, the intermediate-access region, and the lateral region. Furthermore, in order to test whether the number of points affected the registration accuracy, three more point-patterns were created based on the fourth combination but with different number of points of 10, 20, and 30, as shown in Figure 4-6.

These point-patterns then underwent the registration simulation with following variables. The noise parameters were set as the radius of point variation in 3 mm, human error in 0.5 mm, segmentation error in 0.3 mm, and the tracking system error in 0.25 mm. The translational and rotational errors for the initial registration were set to zero. The translational perturbation was set to 5 mm and the rotational perturbation was set to 5 degrees. The number of iterations for the Monte Carlo simulation was tested and then set to 100.
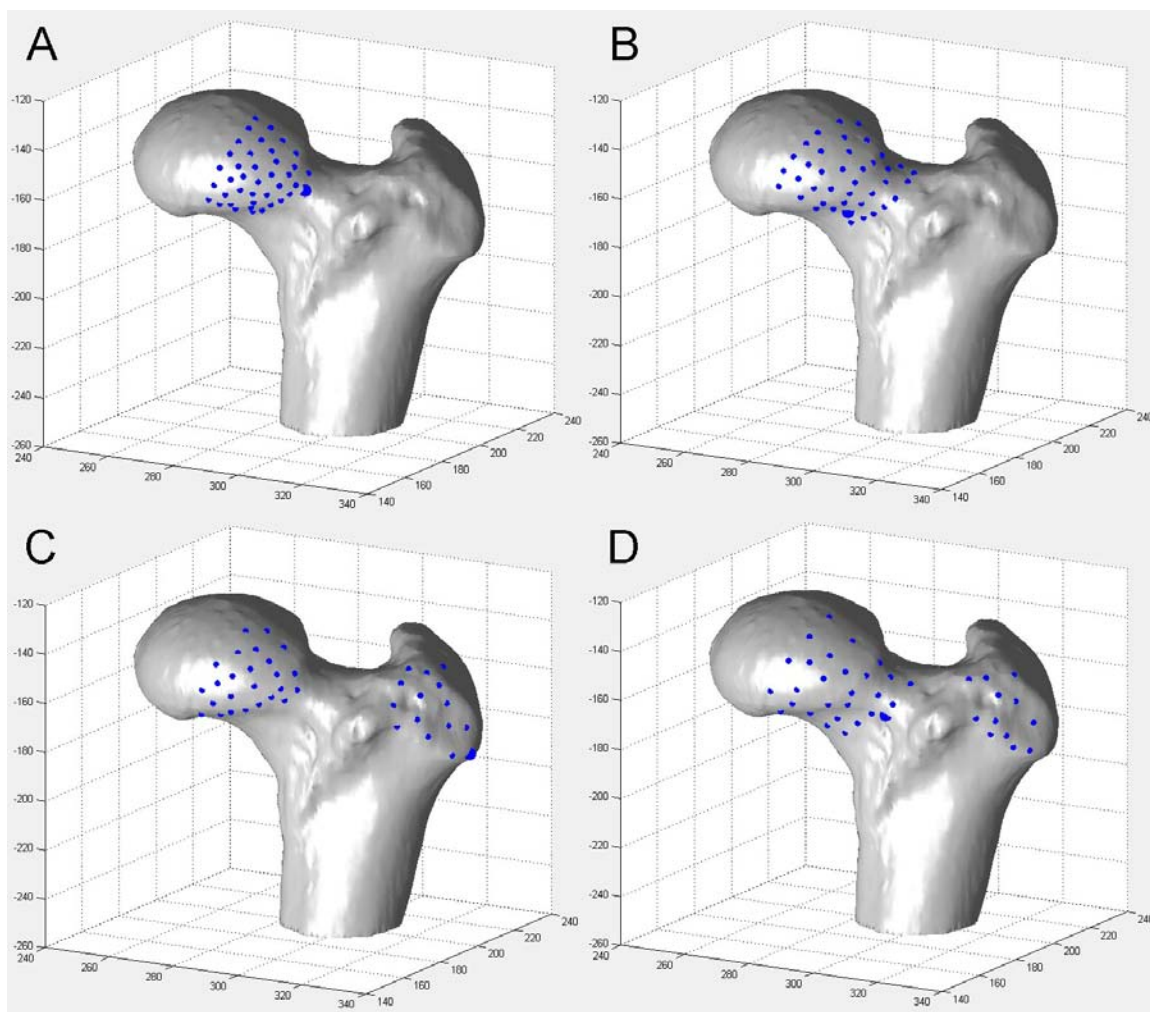
Figure 4-5: Picture of the different combinations of the access areas. A) The first combination includes the direct-access region only. B) The second combination includes the direct-access region and the intermediate-access region. C) The third combination covers the direct-access region and the lateral region. D) The fourth combination consists of all the direct-access region, the intermediate-access region, and the lateral region.
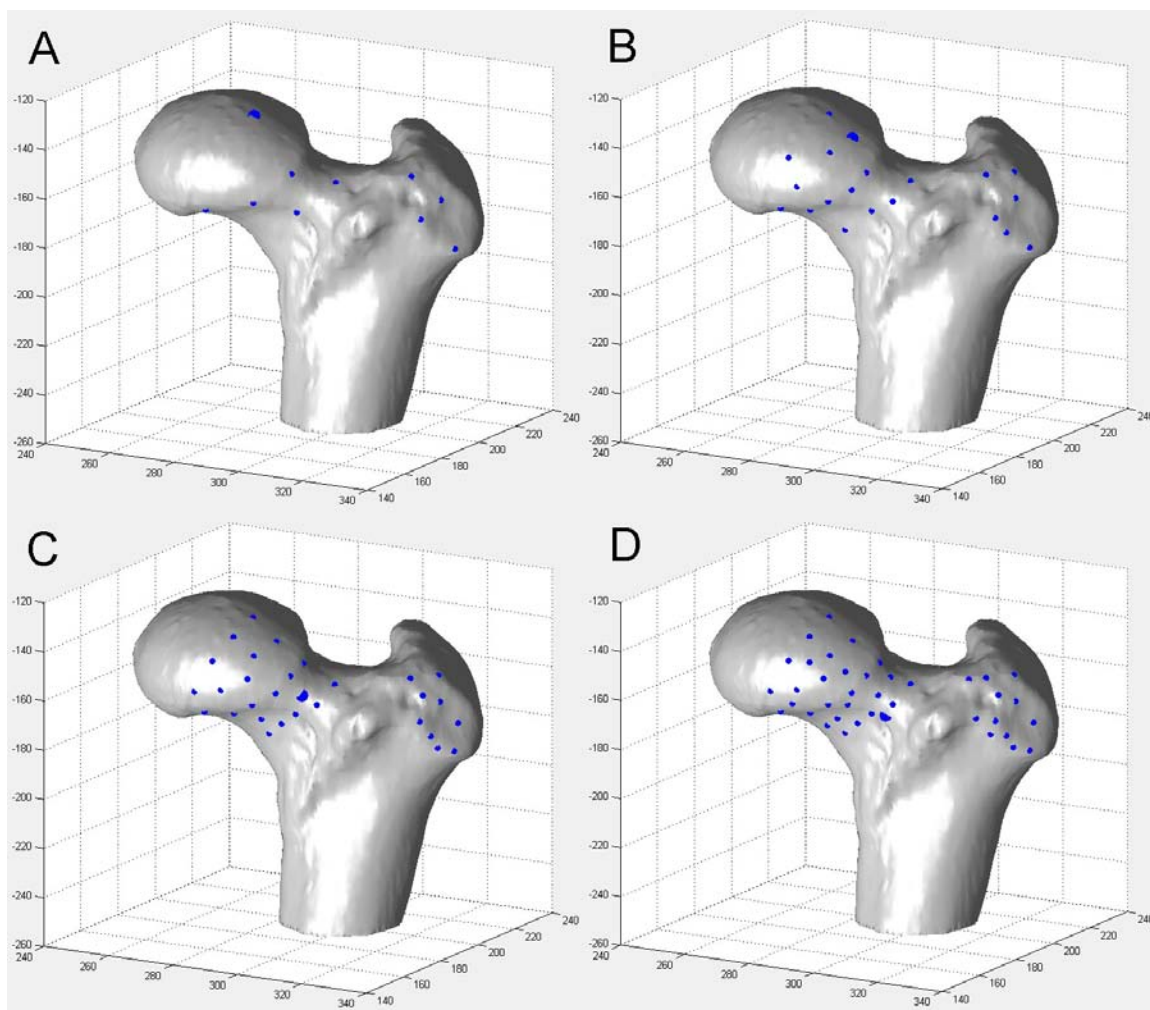
Figure 4-6: Picture of the point-patterns based on the fourth combination of the direct-access, intermediate-access, and lateral regions with different number of points of A) 10, B) 20, C) 30, and D) 40 (the original point-pattern of the fourth combination).

Next, to test whether the perturbation process affected the registration accuracy, the point-pattern based on the fourth combination of access areas with 40 points underwent the registration simulation. The noise parameters and variables were the same as those used for the point-pattern evaluation described above, but with different perturbation values: 1) the translational perturbation in 0, 3, 5, 10, and 15 mm with the

rotational perturbation in 5 degrees; and 2) the translational perturbation in 5 mm with the rotational perturbation in 0, 3, 5, 10, and 15 degrees.

The accuracy of each registration simulation was calculated as the average RMS error of all the Monte Carlo iterations. In the ideal case of the registration simulation, i.e., without any introduced noise, the registration points exactly match with the closest points on the bone; in other words, the RMS error is zero, and the resulting transformation matrix is an identity transform that is used as the gold standard transformation. In the present study, the translational and rotational errors in x, y, and z-axes were calculated by comparing the transformation matrix yielded from the registration simulation with the gold standard transformation. To evaluate the consistency of the registration simulation, two standard deviations (95% confidence) of both the translational error and the rotational error of all the Monte Carlo iterations were computed.

4.3 RESULTS

The results of the registration simulation with different combinations of access areas are described as follows. The registration accuracy in terms of the RMS error is illustrated in Figure 4-7. It shows that the combination consisting of the direct-access region and the intermediate-access region resulted in the lowest RMS error at 0.57 mm. Figure 4-8 and Figure 4-9 show respectively the results of the registration consistency in translation and rotation. The combination consisting of the direct-access region and the lateral region led to the lowest two standard deviations of both the translational error of all axes at 1.08 mm and the rotational error of all axes at 2.55 degrees.
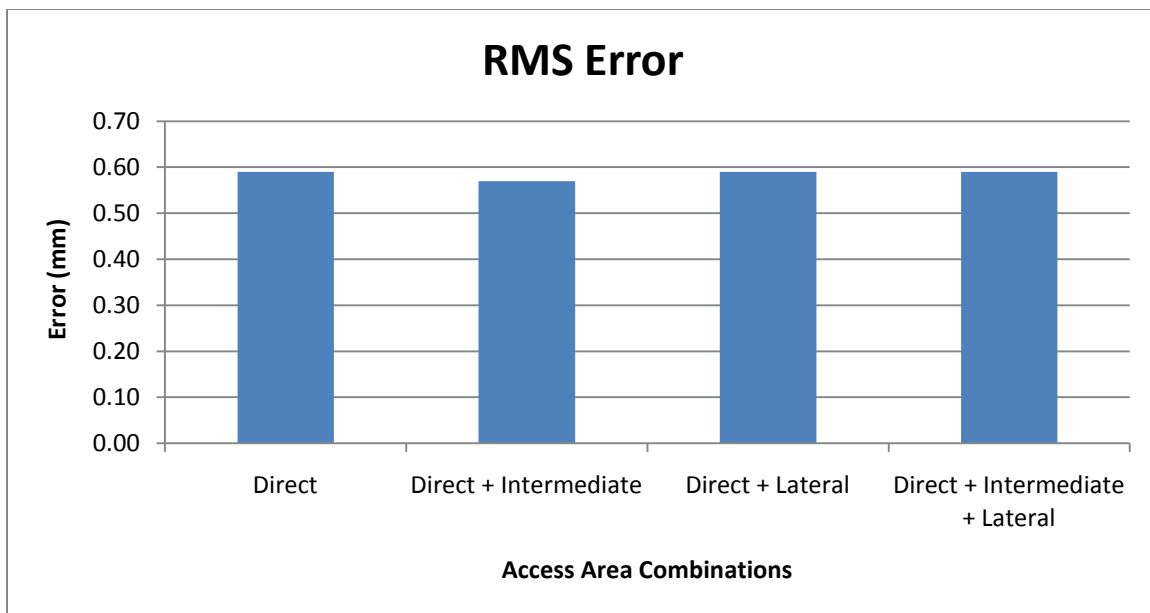
Figure 4-7: The results of the registration simulation accuracy of different access area combinations.
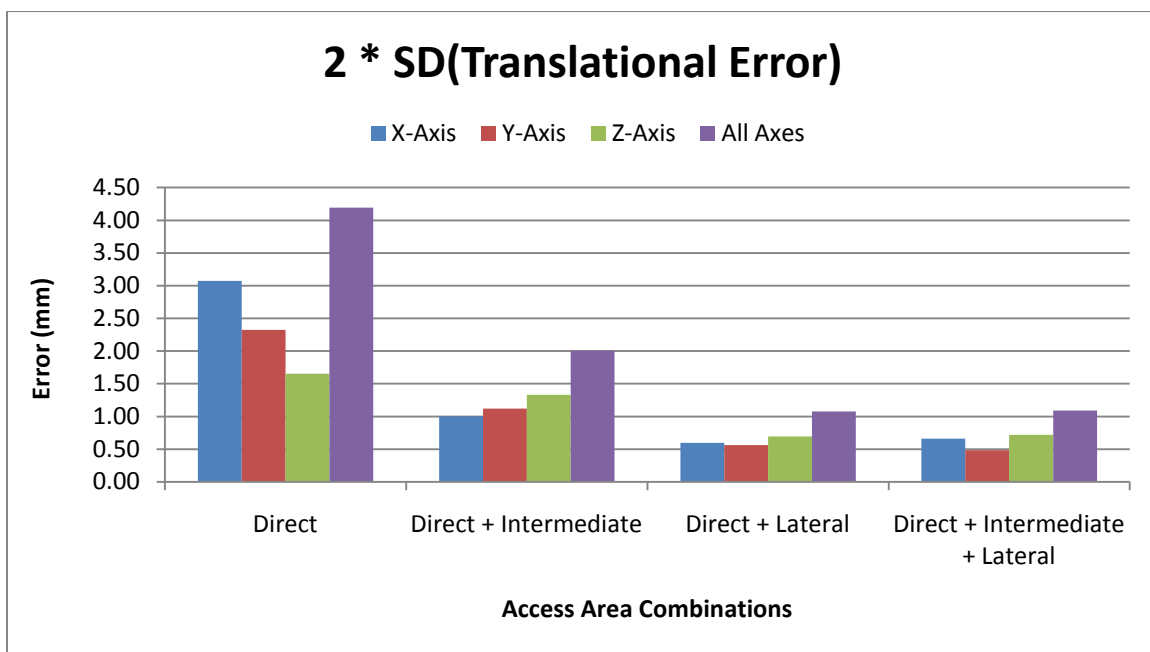
Figure 4-8: The results of the registration simulation consistency in translation of different access area combinations.
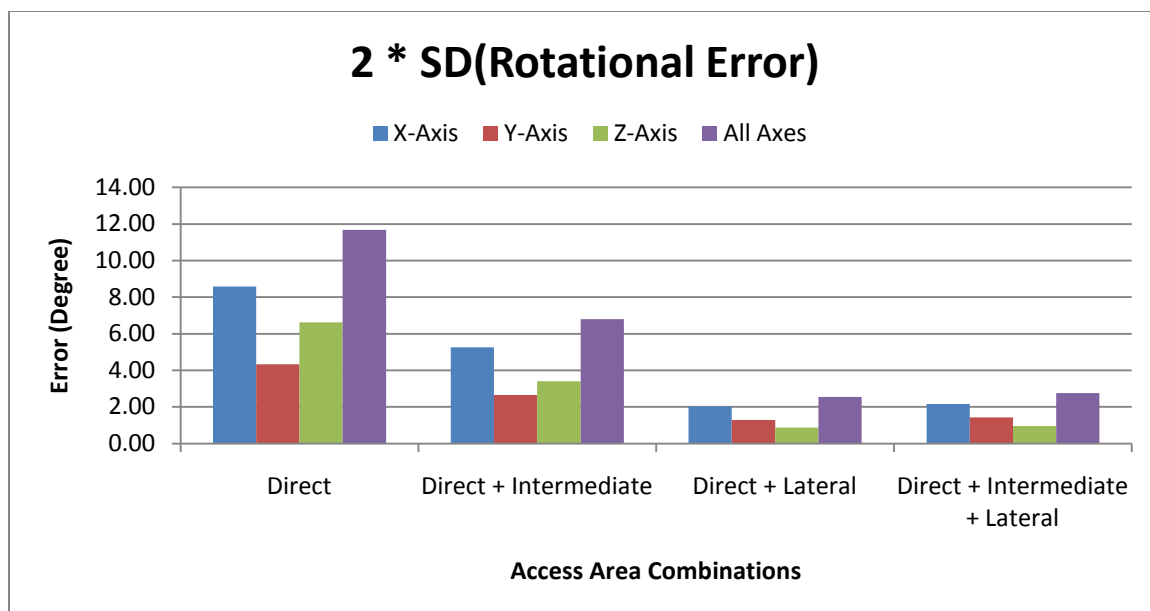
Figure 4-9: The results of the registration simulation consistency in rotation of different access area combinations.

The results of the registration simulation of the combination covering all the direct-access region, the intermediate-access region, and the lateral region but with different number of points are presented as follows. The registration accuracy, in terms of the RMS error, is illustrated in Figure 4-10 and it shows the point-pattern with 10 registration points led to the lowest RMS error at 0.42 mm. The results of the registration consistency in translation and rotation are shown respectively in Figure 4-11 and Figure 4-12. The point-pattern with 40 registration points resulted in the lowest two standard deviations of both the translational error of all axes at 1.09 mm and the rotational error of all axes at 2.76 degrees, as can be found in Figures 4-11 and 4-12.
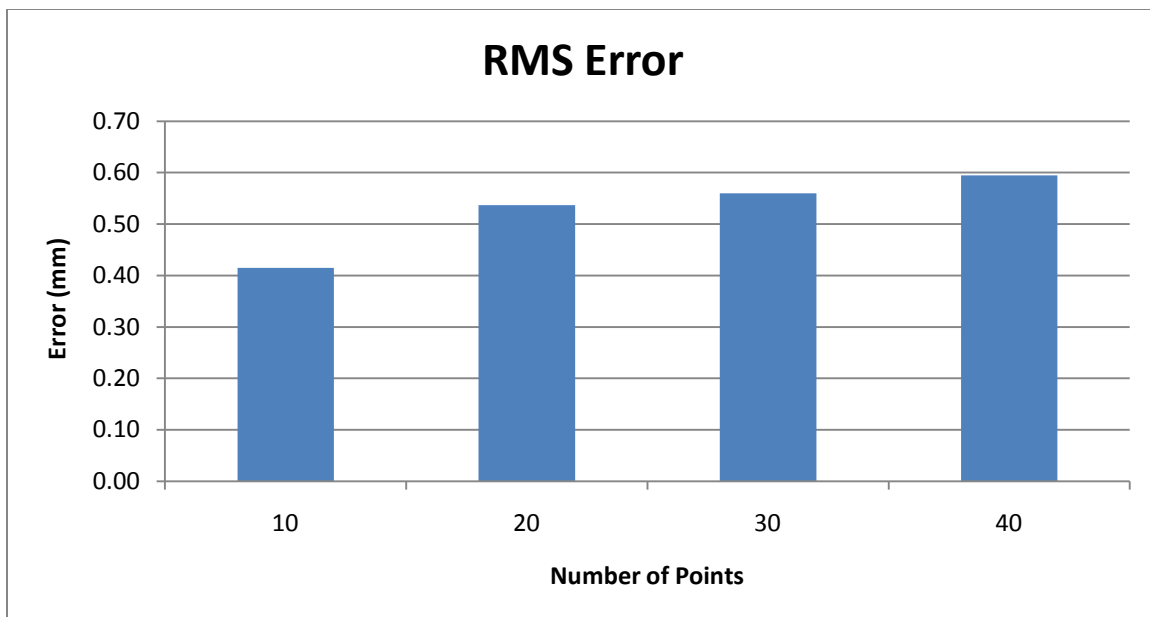
Figure 4-10: The results of the registration simulation accuracy of the patterns consisting of different number of points.
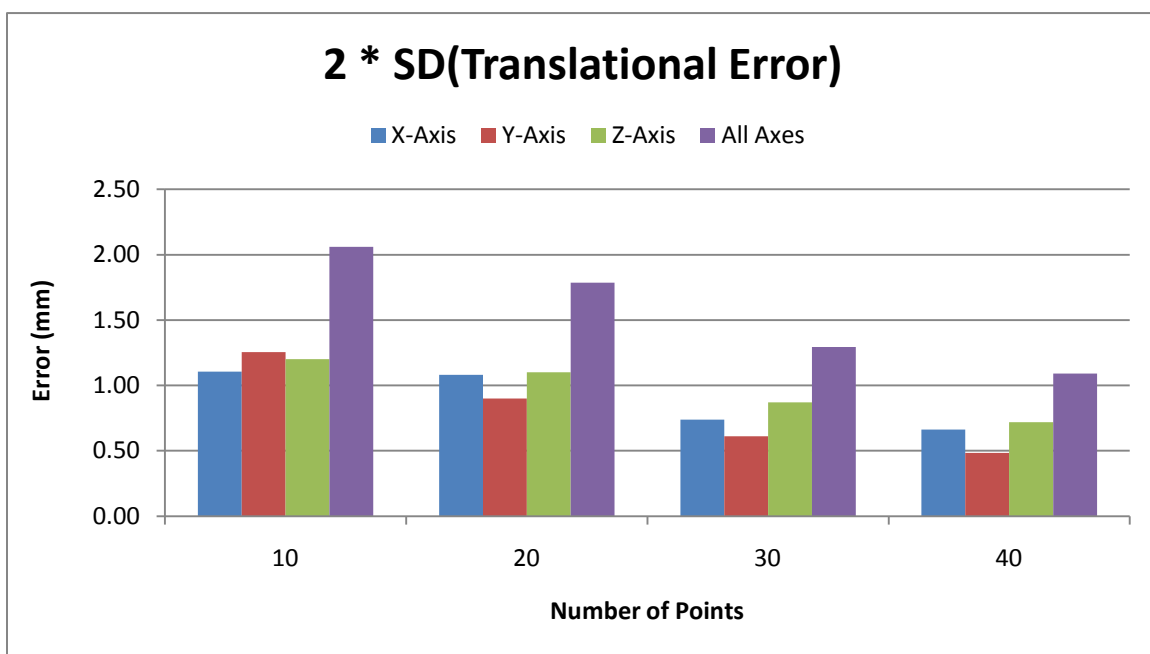
Figure 4-11: The results of the registration simulation consistency in translation of the patterns consisting of different number of points.
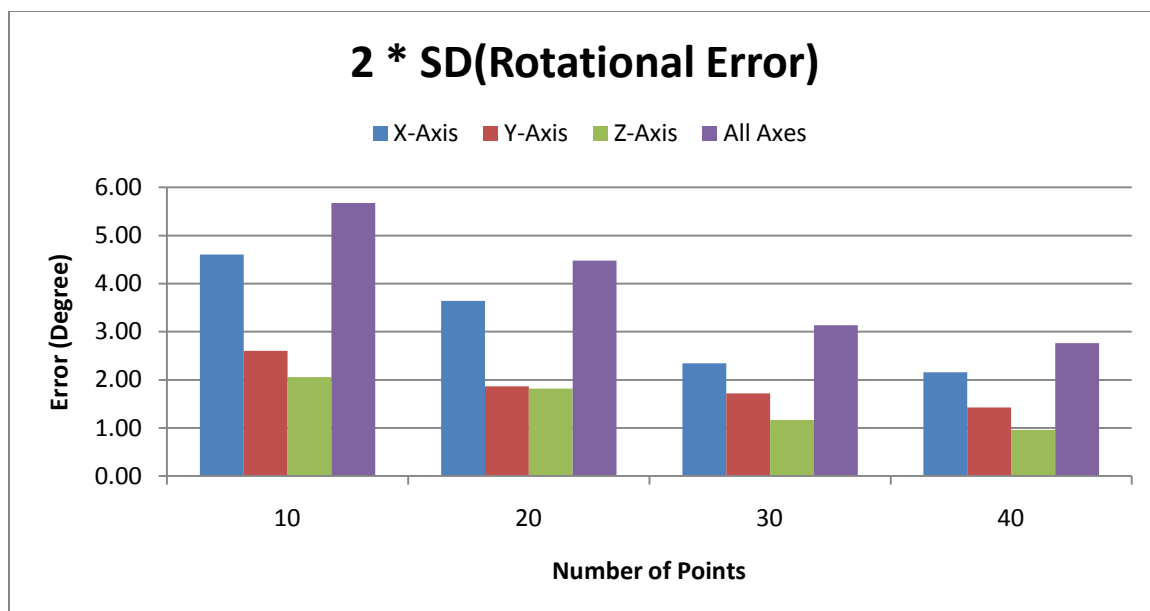
Figure 4-12: The results of the registration simulation consistency in rotation of the patterns consisting of different number of points.

The results of the registration simulation for combining the direct-access region, the intermediate-access region, and the lateral region with different translational perturbation are described as follows. Figure 4-13 shows the registration accuracy in terms of the RMS error: the translational perturbation at 3 and 5 mm both resulted in the lowest RMS error at 0.57 mm. Figure 4-14 illustrates the results of the registration consistency in translation, and it shows that he translational perturbation at 0 mm led to the lowest two standard deviations of the translational error of all axes at 0.97 mm. The results of the registration consistency in rotation are given in Figure 4-15. The translational perturbation at both 0 and 5 mm resulted in the lowest two standard deviations of the rotational error of all axes at 2.50 degrees (see Figure 4-15).
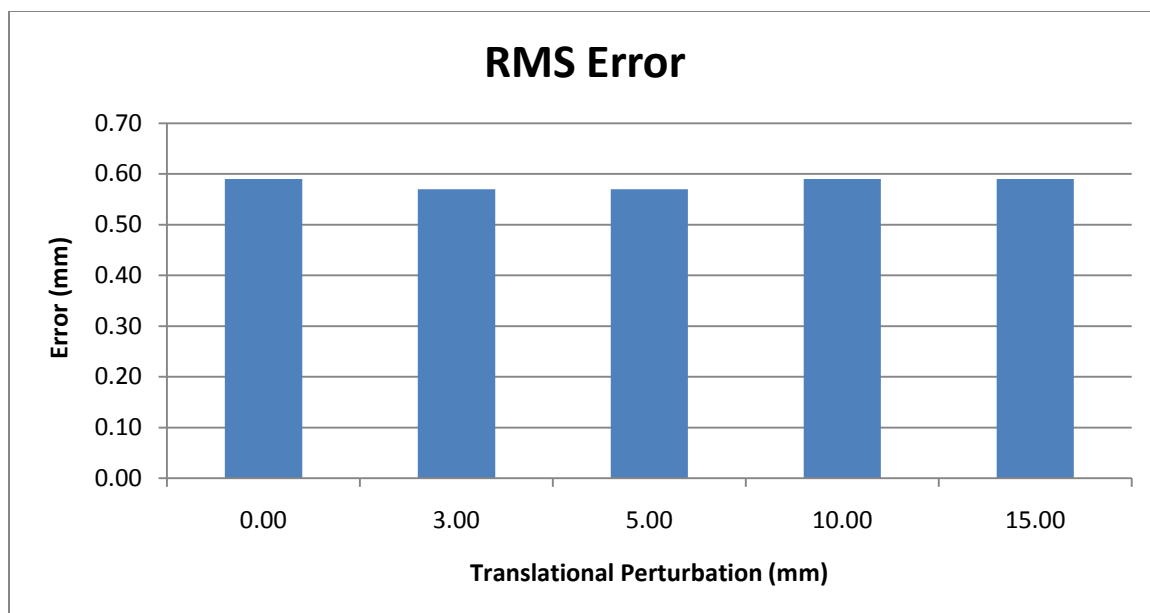
Figure 4-13: The results of the registration simulation accuracy of different translational perturbations.
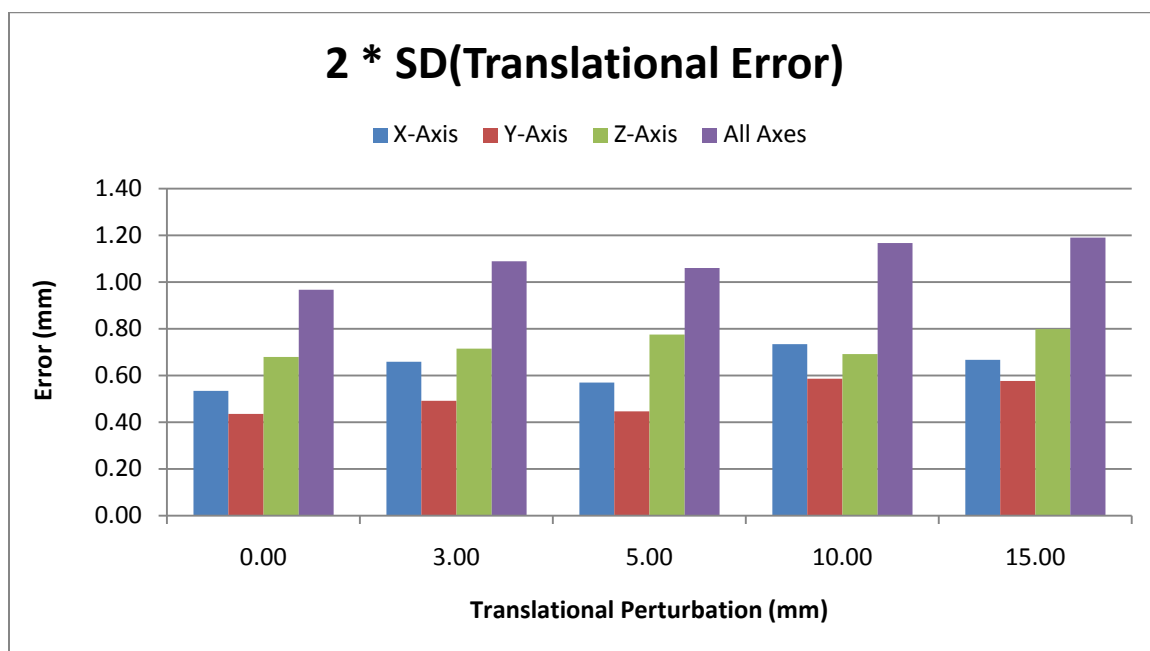
Figure 4-14: The results of the registration simulation consistency in translation of different translational perturbations.
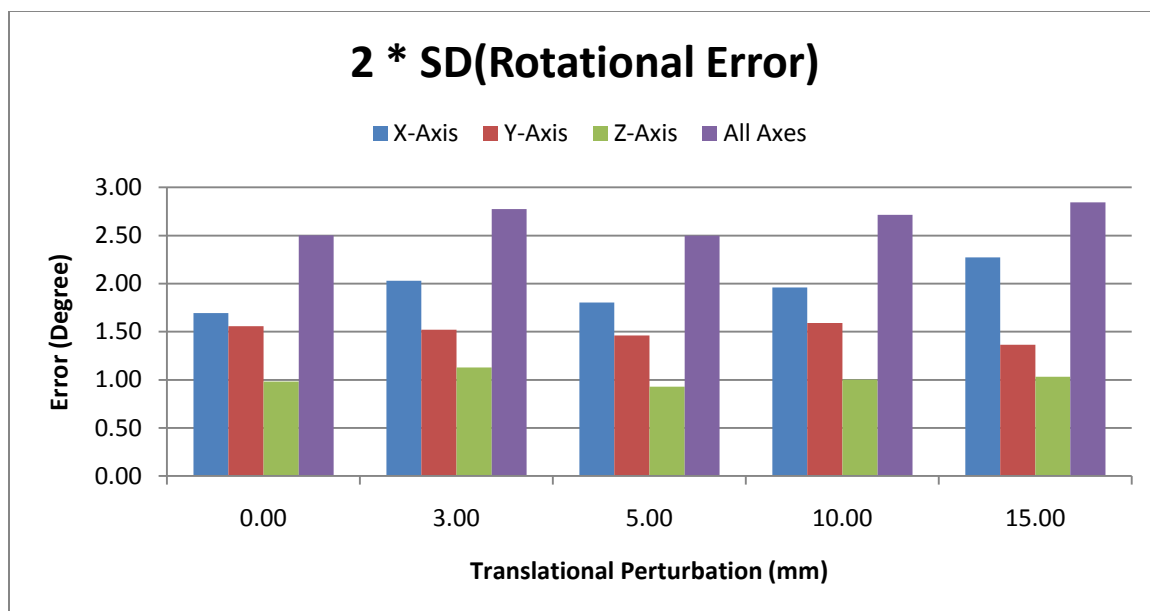
Figure 4-15: The results of the registration simulation consistency in rotation of different translational perturbations.

Lastly, the results of the registration simulation of the combination covering all the direct-access region, the intermediate-access region, and the lateral region with different rotational perturbation are described as follows. Figure 4-16 shows the registration accuracy in terms of the RMS error, and the rotational perturbation at 10 degrees resulted in the lowest RMS error at 0.57 mm. The results of the registration consistency in translation are shown in Figure 4-17, and it can be seen that the rotational perturbation at 10 degrees resulted in the lowest two standard deviations of the translational error of all axes at 1.03 mm. Figure 4-18 illustrates the results of the registration consistency in rotation. It shows that the rotational perturbation at 15 degrees led to the lowest two standard deviations of the rotational error of all axes at 2.51 degrees.
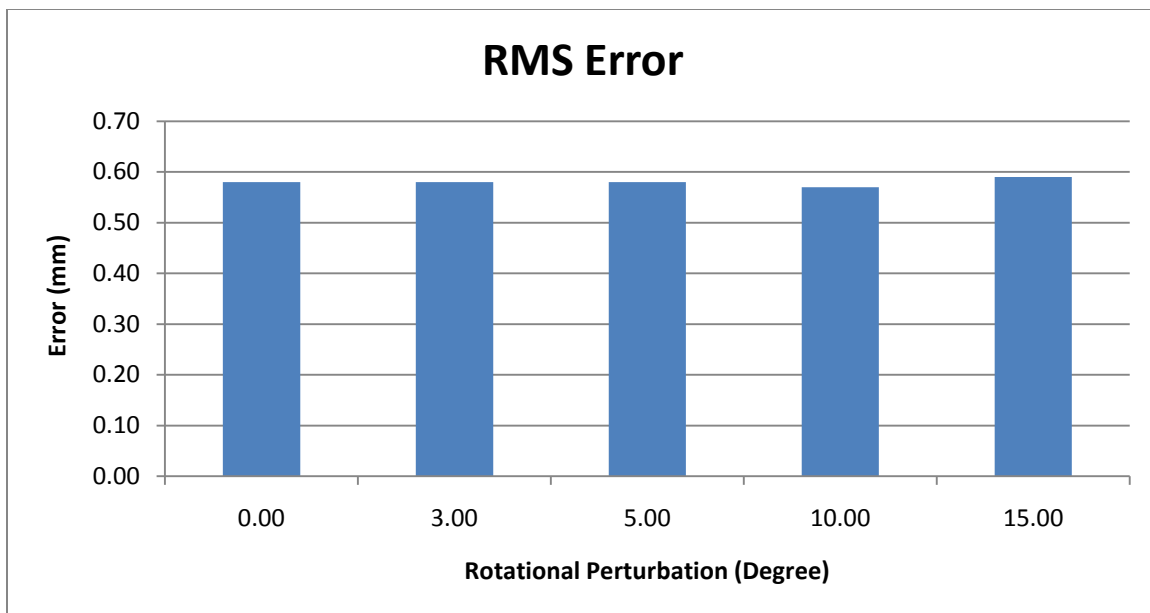
Figure 4-16: The results of the registration simulation accuracy of different rotational perturbations.
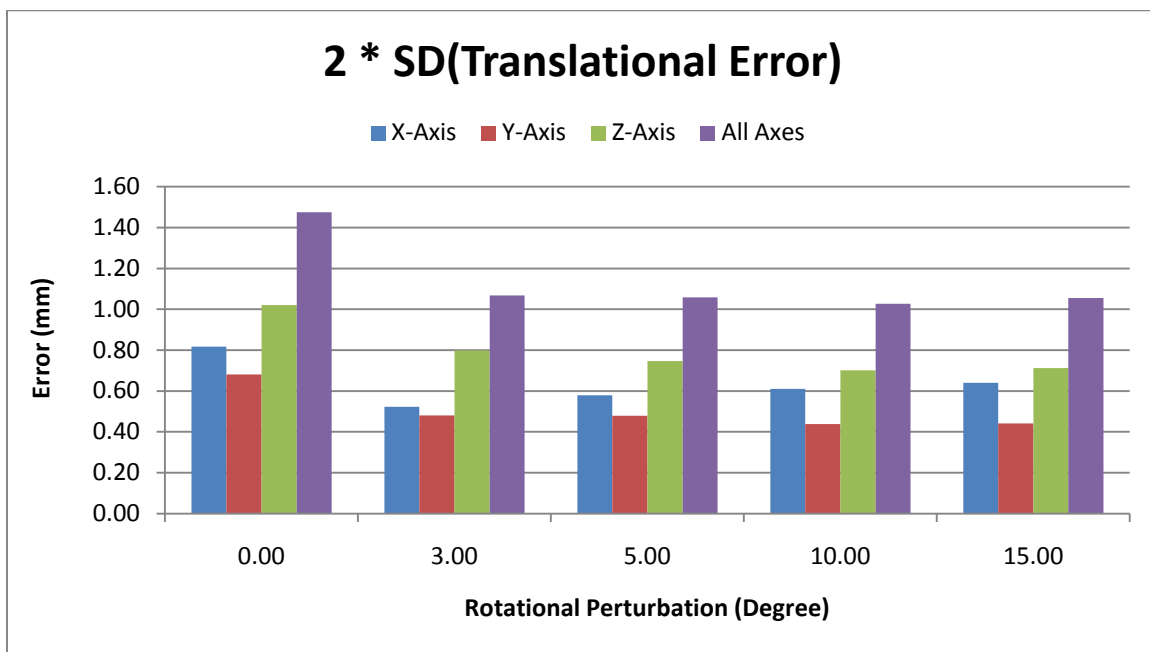

Figure 4-17: The results of the registration simulation consistency in translation of different rotational perturbations.
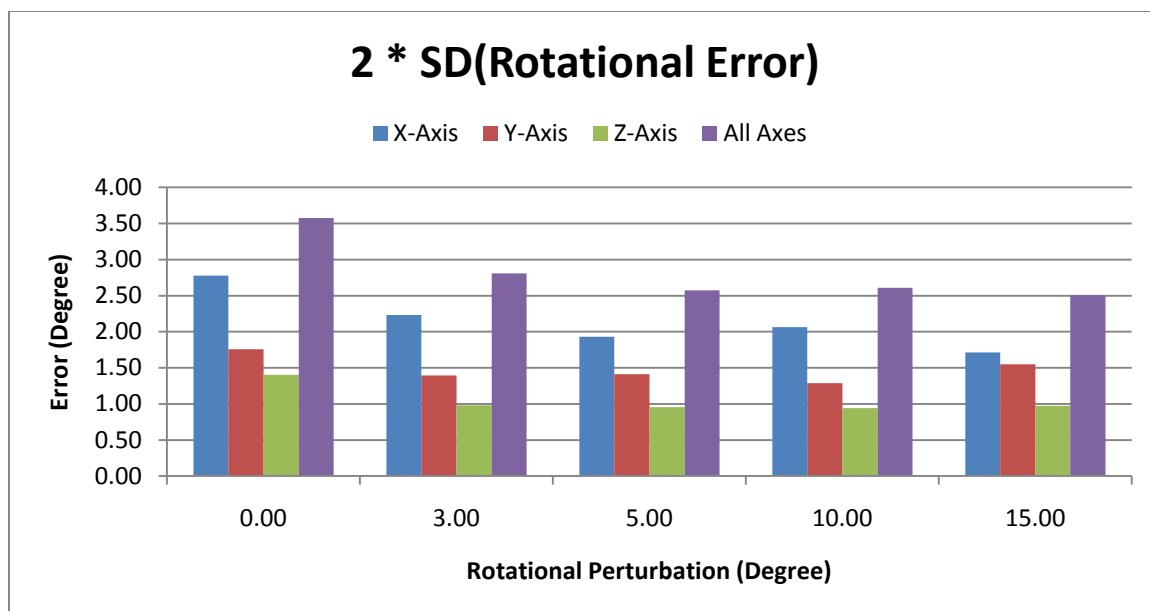
Figure 4-18: The results of the registration simulation consistency in rotation of different rotational perturbations.

4.4 DISCUSSION

For robot-assisted FAI arthroscopy, the surface-based registration allows only limited access areas on the bone for collecting registration points. In addition, the smaller number of points to result in acceptable accuracy, the better. Therefore, in order to get an idea of the registration accuracy of the different registration point-patterns, a registration simulator is developed in this study.

For the point-patterns generated with different access area combinations, the hypothesis is that the combination with more widely distributed points should result in better accuracy (i.e., the lower RMS error) and consistency (i.e., the lower translational and rotational errors). From the results, the RMS errors of all the four designed testing combinations are all within a similar range and no significant difference is found.

However, both the third and the fourth combinations containing the lateral region result in much lower variations of translational and rotational errors than those combinations without covering the lateral region. Thus, a point-pattern with well scattered points should be considered.

In addition, for the point-patterns generated with different number of points, the hypothesis is that the pattern with more points leads to better accuracy and consistency. The results of consistency in the present study correspond with the hypothesis; however, the results of accuracy appear to contradict it. One of the possible reasons is that the pattern with small number of points provides merely little information about the shape feature of the model. Although this gives the ICP algorithm more flexibility in 3D fitting to achieve a lower RMS error, it also results in higher variations of translational and rotational errors. The results suggest that a trade-off between the number of points and the transformation error should be taken into account while designing a pattern for FAI arthroscopy.

For the registration simulation with 1) perturbation of 5 degrees in rotation and various translations and 2) perturbation of 5 mm in translation and various rotations, our results show that all the tests converge to the global minimal and result in the accuracy within a similar range between 0.57 mm to 0.59 mm. This might be due to that the original starting position used in the simulation is close to a good initial guess, so that the global minimal can be easily found either with 5 degree rotational perturbation or 5 mm translational perturbation.

Furthermore, in terms of the consistency, interestingly, for the simulation with perturbation of 5 degrees in rotation and various translations, the tests with 0 mm and 5

mm translational offset lead to slightly lower variation both in translational and rotational errors. However, for the simulation with perturbation of 5 mm in translation and various rotations, all the tests with translational perturbation show clearly lower variations both in translational and rotational errors. These might suggest that perturbation in rotation has more effect than that in translation in terms of registration consistency.

It should be noted that the values of the noise parameters in the present study are determined based on our previous experiences and experimental results from MAKO. These values may be changed time to time and result in different simulation results. In addition, the point-patterns used in this study are arbitrarily generated based on the operator's opinion, and they might not cover all the shape features of the model. The noises of the initial registration are also ignored to simplify the simulation circumstance. However, inaccurate initial registration with noises can greatly affect the starting position used for ICP algorithm and result in low registration accuracy. Furthermore, the perturbation scheme used in this study is designed originally for MAKO's knee application to avoid that the ICP algorithm converges to a local minimal caused by the rotation around the long-axis of the femur. A better perturbation scheme for FAI can be further developed.

Future works include a comprehensive study to determine the values of the noise parameters, an objective method of defining the point-patterns, and an extensive study to simulate the initial registration errors. To verify the simulator, the point-pattern should be physically tested on sawbones and cadavers, and the results should be compared with those from the simulation. The point-pattern should also be tested with the bone models in different sizes to evaluate the usability and reliability of the pattern.

To conclude, this chapter presents a preliminary study on registration simulation for robot-assisted FAI arthroscopy. The registration simulator is developed to evaluate the registration accuracy for any given point-pattern. Various registration parameters and randomly generated noises are determined to simulate the real registration process. The registration point-pattern with points widely distributed in different bone access areas results in better registration accuracy and consistency. The experimental results also suggest that a trade-off between the number of points and the registration consistency should be considered while designing a point-pattern for FAI application. Furthermore, translational perturbation may have more effect on registration consistency than rotational perturbation dose. The developed simulator can be further improved and may be used to determine an optimized point-pattern, which yields the best registration accuracy and requires only the minimal number of data points.

CHAPTER 5

HIP RANGE OF MOTION SIMULATION AND VERIFICATION

This chapter presents a software simulation system developed for pre-operatively predicting the functional hip ROM for robot-assisted FAI arthroscopy. This system virtually detects the impingement between bones based on the bounding sphere collision detection computer graphics algorithm. The ROM of the imported surface model, such as healthy or FAI diseased bones, is returned by the system to provide the surgeon with a better understanding of the normal or pathological hip kinematics. The suggested resection volume is also computed by the system according to the degree of ROM that the surgeon plans to restore. The developed system serves as a useful tool for the surgeon to pre-operatively evaluate the hip kinematics and decide the surgical plan.

The present chapter is organized as follows. A brief introduction and literature review are firstly discussed. We then present how the bounding sphere collision detection is applied to the impingement detection system. A verification process for evaluating the precision and accuracy of the impingement detection system is also described. After this, an example of hip ROM simulation based on the developed system is presented. The simulated ROM is verified by manual manipulation of the sawbones under optical tracking system navigation. Lastly, the method used to generate the resection volume which restores the desired degree of ROM is explained. The results and a discussion are provided in the end of the chapter.

5.1 INTRODUCTORY REMARKS

As discussed earlier in Chapter 1, FAI is described as an abnormal impingement caused by bony deformities, between the proximal femur and acetabular rim during hip movement. FAI reduces hip ROM and produces pain in patients during daily activities. Two distinct types of FAI have been classified: namely pincer impingement, which is characterized by acetabular deformities; and cam impingement, which is characterized by femoral deformities. Surgical intervention for FAI includes soft tissue and bony repair in order to restore hip ROM. FAI arthroscopy is a minimally invasive approach and has become increasingly popular for treating cam impingement. For robot-assisted FAI arthroscopy, in order to virtually evaluate the surgical outcome of the pre-operative plan, a system capable of simulating hip ROM by given bone models is desirable.

Studies have been conducted to evaluate the ROM of the hip joint. Kang et al. (Kang et al., 2002; Kang et al., 2003) simulated hip ROM to quantify hip kinematics as a function of hip morphology. They calculated the extreme hip ROM by moving the hip joint center while keeping a constant distance between the acetabular rim and the femoral head. V-COLLIDE (Hudson et al., 1997), a collision detection library based on oriented bounding box hierarchies, was utilized by Richolt et al. (Richolt et al., 1999) to estimate hip ROM for assessing slipped capital femoral epiphysis. Hip ROM also plays an important role for evaluating the surgical outcome of total hip replacement (THR). Kawasaki et al. (Kawasaki et al., 2004) used an adaptive refinement strategy while Sun et al. (Sun et al., 2007) used a CT image based 3D geometric method to simulate hip ROM for THR.

For the investigation of hip ROM for FAI, Cai et al. (Cai et al., 2009) described an impingement detection system that used spherical coordinates for data sampling to calculate the minimum distance between the acetabulum and femur. Arbabi et al. (Arbabi et al., 2007; Arbabi et al., 2009; Arbabi et al., 2010) proposed a collision detection method using a "ball-and-socket" mechanical model that mimicked the human hip joint. Unlike commonly used collision detection algorithms in computer graphics, these methods involved finding the curvilinear and radial penetration depth to evaluate hip ROM for FAI. Nevertheless, Kubiak-Langer et al. and Tannast et al. (Kubiak-Langer et al., 2007; Tannast et al., 2007a) utilized a voxel based impingement detection method (Hu et al., 2001) which used a linear transform to convert surface information from one lookup table to another. A cell in the lookup table holding two voxels' information indicated a collision occurrence.

The above impingement detection methods (Kawasaki et al., 2004; Arbabi et al., 2007; Arbabi et al., 2009; Cai et al., 2009; Arbabi et al., 2010) were primarily focused on improving the computation performance by taking advantage of the ball-and-socket model of hip anatomy. These methods may enhance the computation efficiency; however, they are not ideal for non-ball-and-socket models of anatomies such as the knee, spine, and wrist. The methods discussed in Hu et al., Kubiak-Langer et al., and Tannast et al. (Hu et al., 2001; Kubiak-Langer et al., 2007; Tannast et al., 2007a) did not provide penetration depth of the impingement for defining the pre-operative resection volume in order to restore the hip kinematics. In the present study, the intention was to develop a general impingement detection method, based on 3D computer graphical models, which

could yield a penetration depth and be implemented in any orthopedic applications not restricted to ball-and-socket movement only.

This chapter presents an impingement detection simulation system, which pre-operatively predicts the functional hip ROM of given surface models, i.e., healthy or FAI diseased bones. In the present study, an impingement detection system by implementing bounding sphere computer graphic algorithm is developed. The location of the impingement and the penetration depth between bone models are computed. Then, both the precision and accuracy of the impingement detection system are verified by using a custom-designed phantom to imitate ball-and-socket hip movement. Next, an example of hip ROM simulation based on the developed system is given. The simulated ROM is verified by manual manipulation of the sawbones under optical tracking system navigation, which provides the ground truth for calibration. Finally, the resection volume is generated by the system based on the desired degree of ROM that the surgeon wants to restore.

5.2 MATERIALS AND METHODS

The software was developed on a PC (Precision T5400, Dell Inc., Round Rock, TX) with Quadro FX 3700 graphic card (NVIDIA Corp., Santa Clara, CA), 4GB RAM, and Linux operating system, Red Hat Enterprise Linux 5.3 (Red Hat Inc., Raleigh, NC). The software was written in C and Tcl/Tk 8.3 using the installed library of the RIO software navigation platform (MAKO Surgical Corp., Fort Lauderdale, FL). The commercially available computer-assisted robotic system, RIO Robotic Arm Interactive

Orthopedic System (MAKO Surgical Corp., Fort Lauderdale, FL), was utilized for this study. The robotic system was equipped with a passive 3D optical tracking system, Polaris Spectra (Northern Digital Inc., Waterloo, Ontario, Canada), with an accuracy of 0.25 mm RMS error. The tracking system continuously monitored optical tracking markers and returned the position and orientation of the markers in space. Each optical marker was attached with infrared reflective spheres (11.5 mm in diameter) arranged in a unique pattern. The tracking system could therefore distinguish each individual marker and return the correct orientation and position based on this specific pattern.

As described in chapter 3, three 3D Cartesian coordinate spaces were defined in this study. "Camera space" was the coordinate system created by the tracking system; "anatomic space" was the coordinate system of the patient's (or sawbone's) surgical region; "image space" was the coordinate system of the CT images and bone surface models. The RIO software navigation platform integrated the spatial information of the optical tracking markers in camera space, the patient's surgical site information in anatomic space, and the virtual bone model information in image space.

The STL surface models of both healthy and pathologic proximal left femora as well as a healthy pelvis were generated from CT images. A pathologic left sawbone femur was built from the CT data of a patient, who was diagnosed with cam FAI. This pathologic left sawbone femur, a healthy left sawbone femur, together with a sawbone pelvis (Pacific Research Labs, Inc., Vashon, WA, USA) were first implanted with fiducial markers, and then scanned in supine position at 1 mm slice thickness by CT. For bone registration, eight fiducial markers were implanted on both sawbone femora and ten markers on the pelvis. In order to achieve high accuracy, fiducial markers were placed

close to the anatomic landmarks to minimize registration errors, as illustrated in Figure 5-1. The CT scan covered the entire pelvis as well as the proximal parts (approximately 25 cm) and distal parts (approximately 6 cm) of both femora so that all fiducial markers and anatomical landmarks were included (see Figure 5-2).

The 3D STL bone surface models were generated from the segmented CT images using commercial software (Mimics 13.1, Materialise, Leuven, Belgium), as shown in Figure 5-3. The highest possible segmentation quality was selected to ensure that the anatomical features were well preserved. The STL model was a triangular mesh, which consisted of "facets" and "vertices." Each facet was a triangle formed by three vertices, and all the facets were connected in a specific order represented by "indices." In order to improve the performance of the impingement detection for ROM simulation, the bone models were further processed by in-house developed software. In brief, the STL models were first remeshed so that the length of all edges of any triangle from the triangle meshes was less than 4 mm. This step ensured that all the "bounding spheres" were similar in size to avoid expensive impingement searching of two far away bounding spheres. Next, the remeshed models were compressed by removing repeated vertices and by reordering the corresponding indices. After compression, the number of vertices of each surface model was significantly reduced.
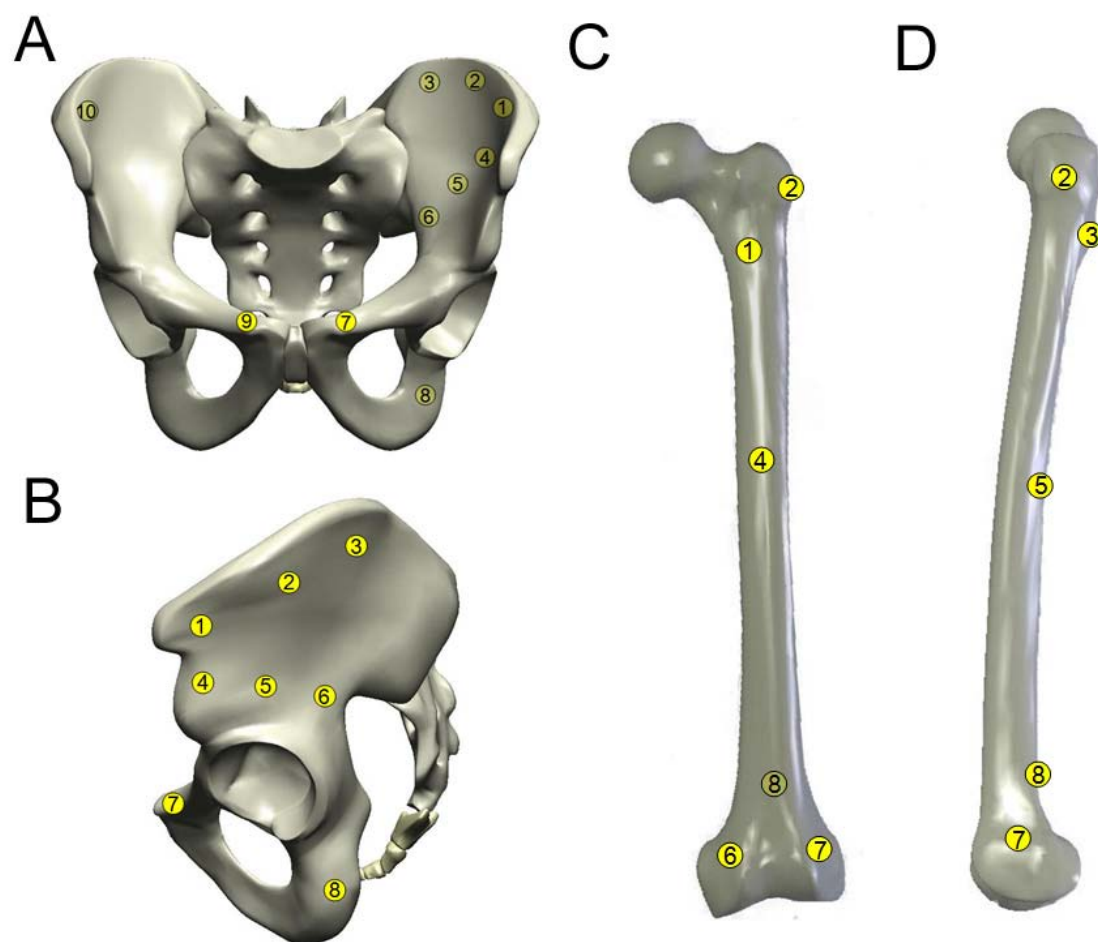
Figure 5-1: Location of the fiducial markers implemented for paired-point bone registration. Ten fiducial markers are installed on the pelvis and eight on the femur. A) and B) represent the anteroposterior and lateromedial views of the pelvis. C) and D) represent the anteroposterior and lateromedial views of the femur. Markers 1 to 6, 8, and 10 shown in A) and marker 8 shown in C) are located in the back of the bones.
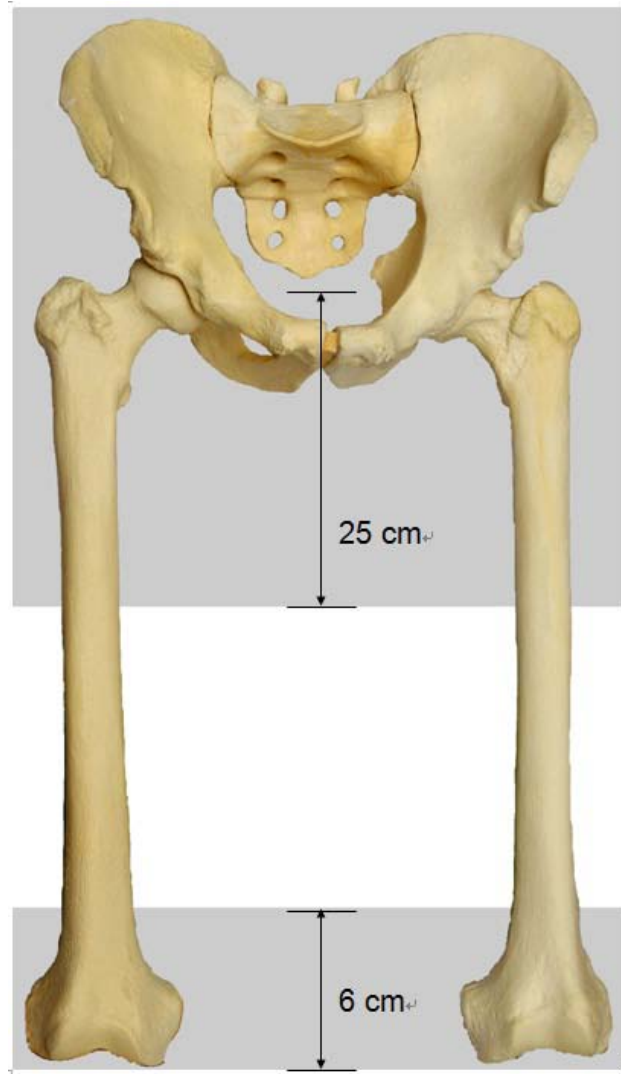
Figure 5-2: CT scan covers the entire pelvis as well as the proximal part (approximately 25 cm) and distal part (approximately 6 cm) of the femur with 1 mm slice thickness.
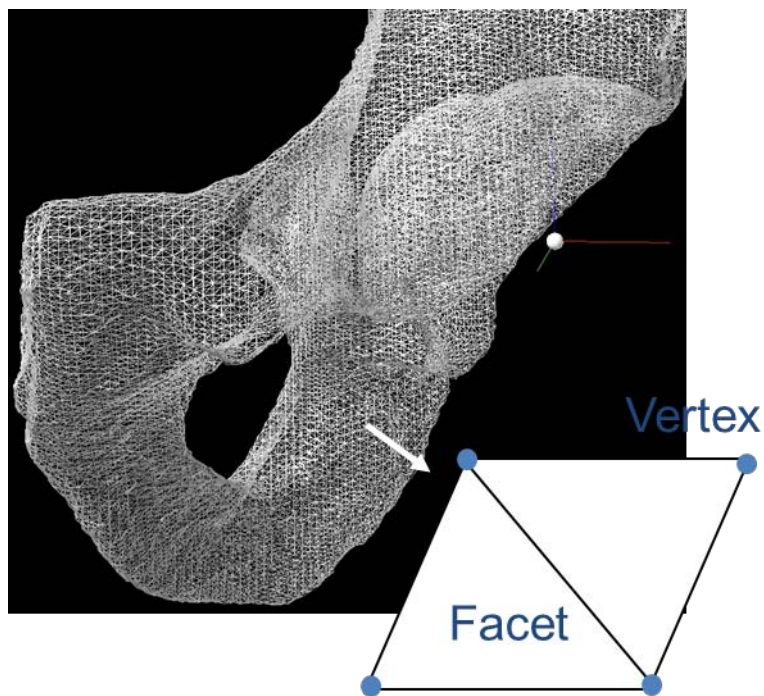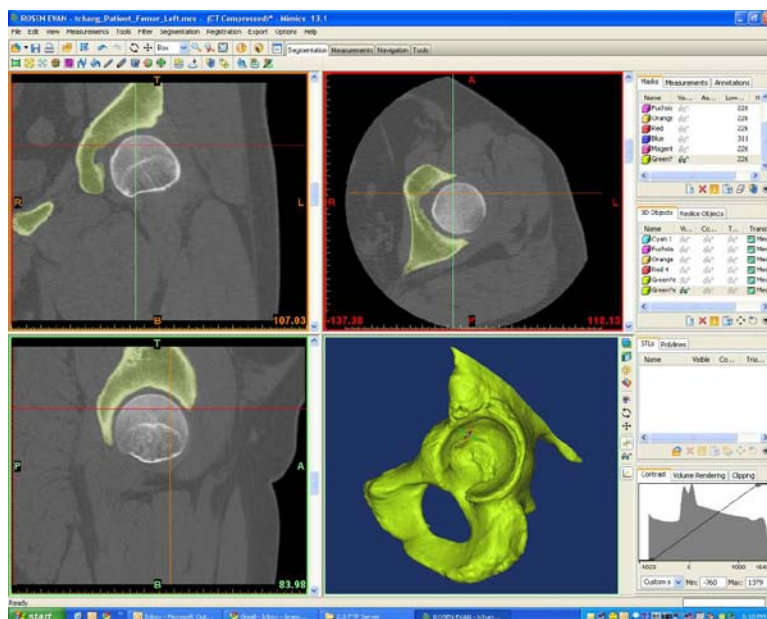
Figure 5-3: The top image shows the segmentation of a pelvis using Mimics software; the bottom image shows the STL model consisting of triangular facets and vertices.

The bounding sphere algorithm constructs two bottom-up bounding sphere "hierarchical trees" for both pelvis and femur models, as illustrated in Figure 5-4. The hierarchy is built by enclosing each triangle within a tightly fitting "bounding sphere." All bounding spheres are linked together by using a "linked list" data structure. They form the lowest level, called "leaf" nodes, of the hierarchical tree (see Figure 5-5). Next, the algorithm selects a leaf node sphere and searches for all other spheres at the same level, which are within distance d of the chosen node sphere. These found candidate spheres along with the chosen sphere are then merged into a larger bounding sphere representing a new node of the higher level. By repeating this searching and merging process, all original leaf nodes are merged into a higher bounding sphere level in the linked-list data structure. Several hierarchical levels can thus be created by using this method repeatedly until eventually all spheres are merged into the largest bounding sphere, the "root" node, which is the highest level of the tree.

Distance d represents the distance between the centers of two bounding spheres and is the sphere merging criterion. It changes constantly at the same time when different levels are generated and is computed by the equation:

$$d_i = d_0 \times 2^i \tag{5-1}$$

where i represents the level of the hierarchy and is ranged from 0 to the number of tree levels; d_0 is the initial merging threshold equal to 10 mm.
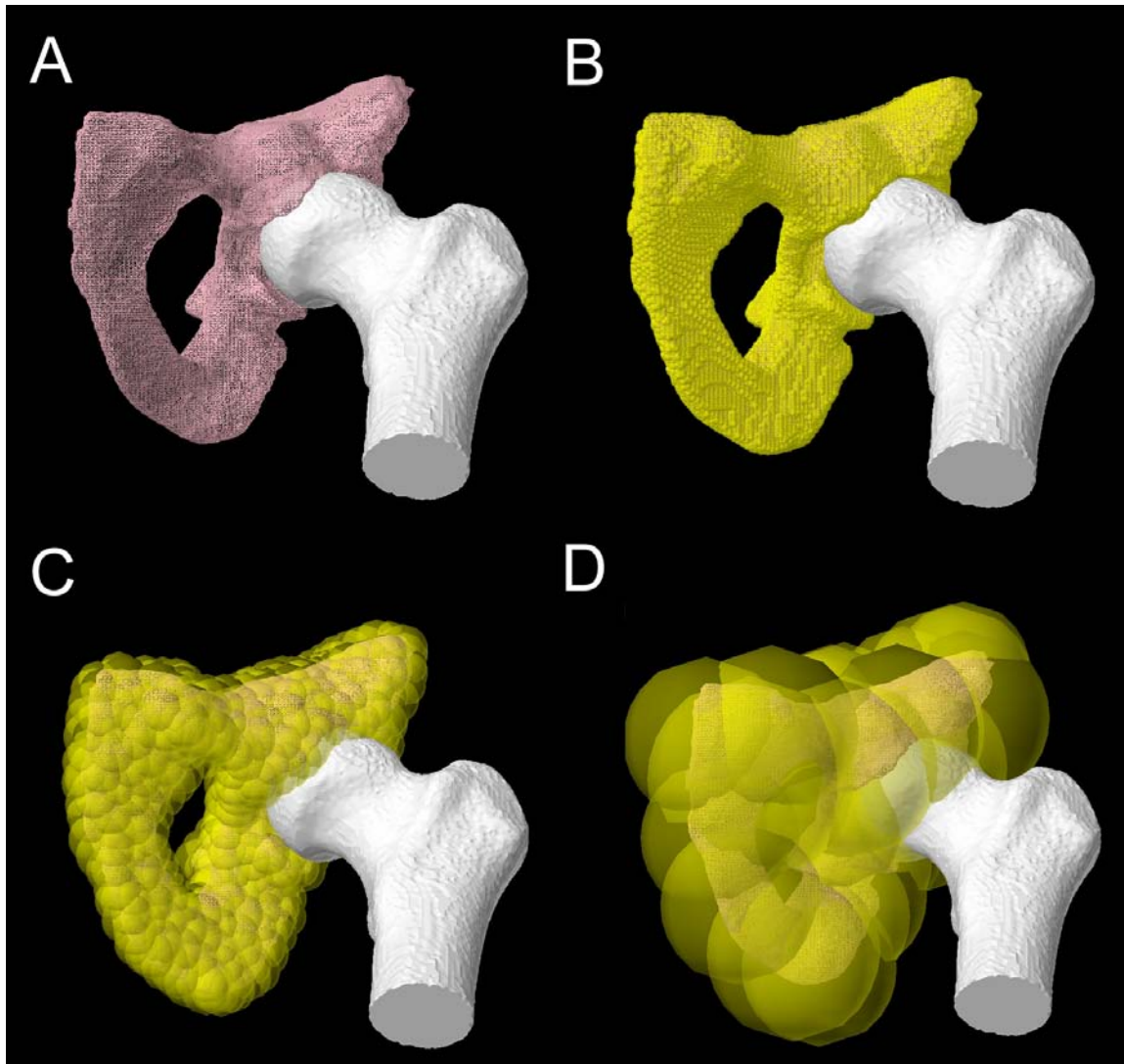
Figure 5-4: Example of bounding sphere hierarchy generated for the pelvis. A) The pelvis surface model displayed in triangle meshes; B) the 1st (leaf) level of the bounding sphere hierarchy consisting of 81200 spheres ; C) the 3rd level of the bounding sphere hierarchy consisting of 671 spheres ; D) the 5th level of the bounding sphere hierarchy consisting of 32 spheres.
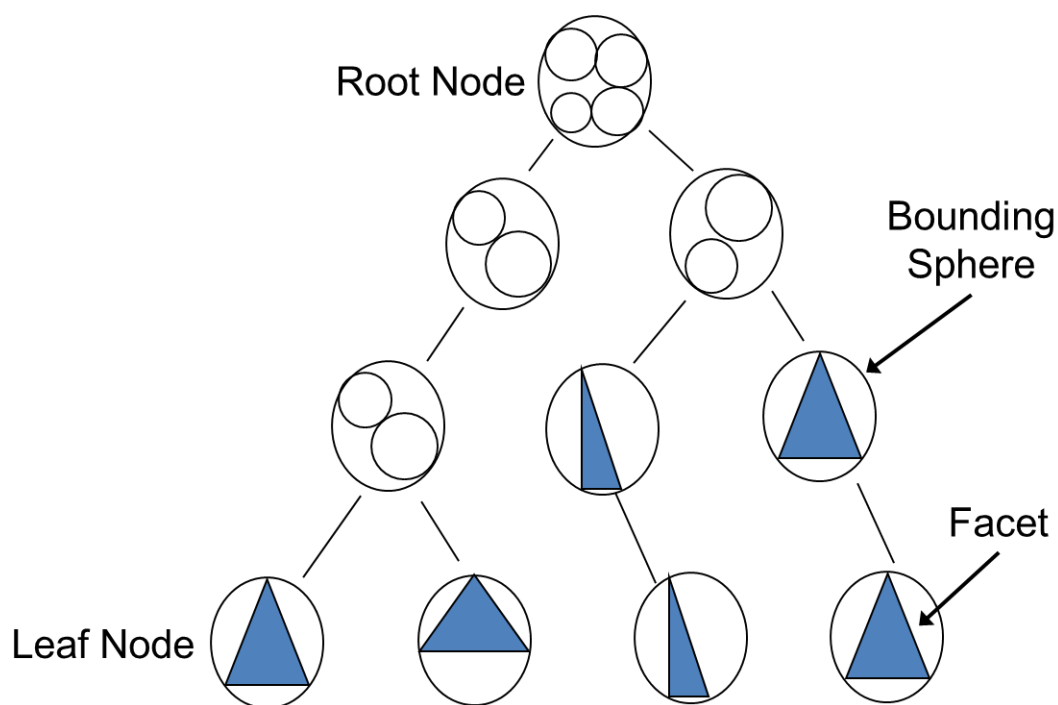
Figure 5-5: Illustration of the structure of the bounding sphere hierarchy.

The completion of this hierarchy permits the fast "broad" phase impingement detection. Starting from the root node of both hierarchies, the algorithm searches for an intersection between any two bounding spheres from different hierarchies, where impingement might be located. If an intersection is detected, the algorithm descends to a lower level and searches for the next sphere intersections. Both hierarchies descend based on the "depth-first" search, as shown in Figure 5-6. The pelvic hierarchy is fully descended before the femur hierarchy is descended. The broad phase search stops and moves to the "narrow" phase of impingement detection once the intersection is detected at the leaf level of both hierarchies. Figure 5-7 illustrates the flowchart of the broad phase search.
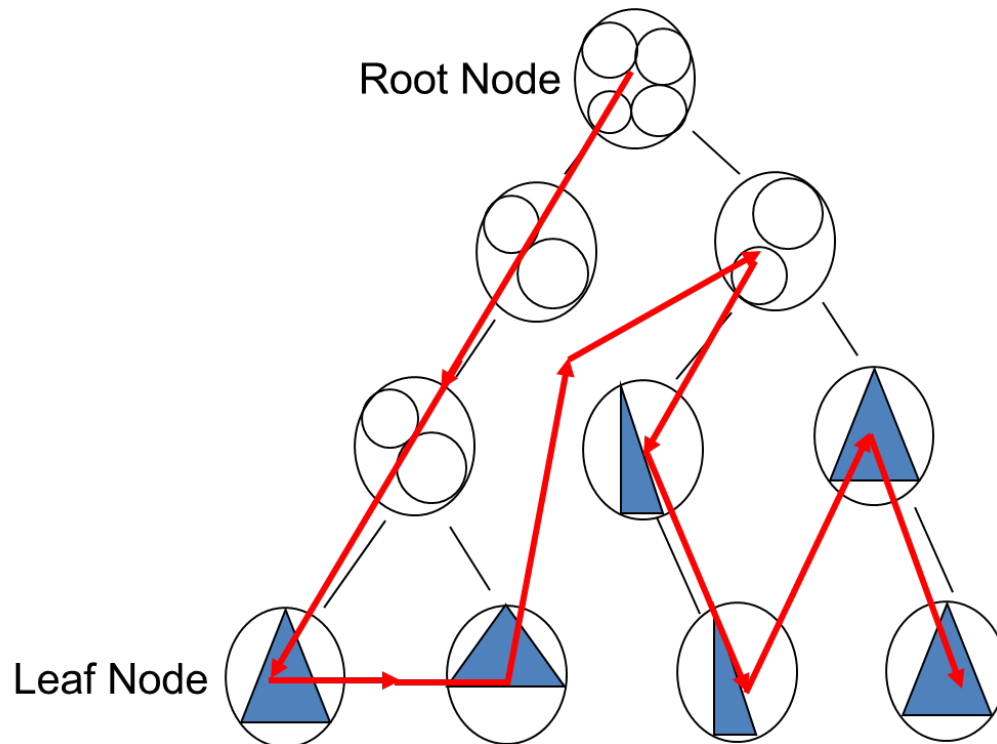
Figure 5-6: Illustration of the depth-first search. The red arrows represent the orders and directions of the searching.
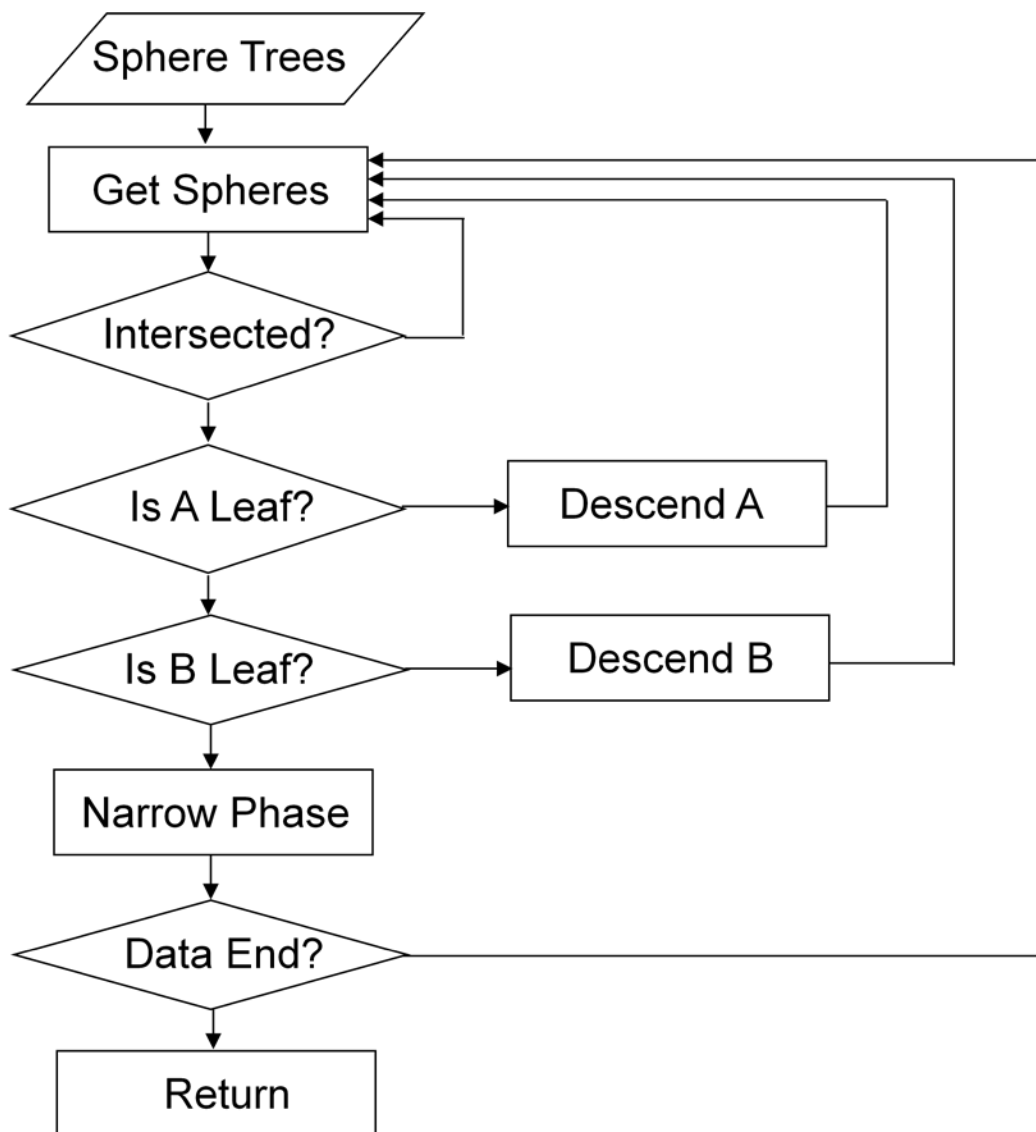
Figure 5-7: The flowchart of the broad phase search.

In the narrow phase, the distance from each vertex of the triangle enclosed by a pelvis leaf sphere ("pelvis vertex") to the triangle enclosed by a femur leaf sphere ("femur triangle") is computed using the Voronoi region method (Ericson C., 2005), as illustrated in Figure 5-8A. The vertices of the femur triangle form a plane consisting of seven regions (V1, V2, V3, E12, E13, E23 and F). A pelvis vertex is projected to the plane. The projected point must fall onto one of the seven regions. If a projected point is within region V1, V2, or V3, the closest point of the pelvis vertex on the femur triangle is located at the corresponding vertex; if a projected point is within E12, E13, or E23, the closest point is located at the corresponding edge; and if a projected point is within F, the closest point is equal to the projected point. The closest distance between each pelvis vertex and the femur triangle is defined as the distance between the pelvis vertex and its closest point on the femur triangle. The shortest distance among the three closest distances of the three pelvis vertices to the femur is hence the closest distance between the pelvis leaf sphere and the femur leaf sphere.

In brief, each pelvis vertex has its shortest distance to the femur triangle, i.e., the length of the "projection vector" defined by the Voronoi method. Among the three vertices' shortest distances, the smallest value represents the closest distance between the intersected pelvis leaf sphere and the femur leaf sphere. By continuously updating the closest distance of all intersected leaf spheres, the resulting closest distance between the pelvis and the femur is finally computed. An impingement is detected by following two scenarios: 1) If the closest distance is smaller than a predefined threshold (0.1 mm in this study), called "touching", and 2) The sign of the dot product between the projection

vector and the normal vector of the femur triangle plane is negative, called "penetrating."

Figure 5-8B illustrates the detail.
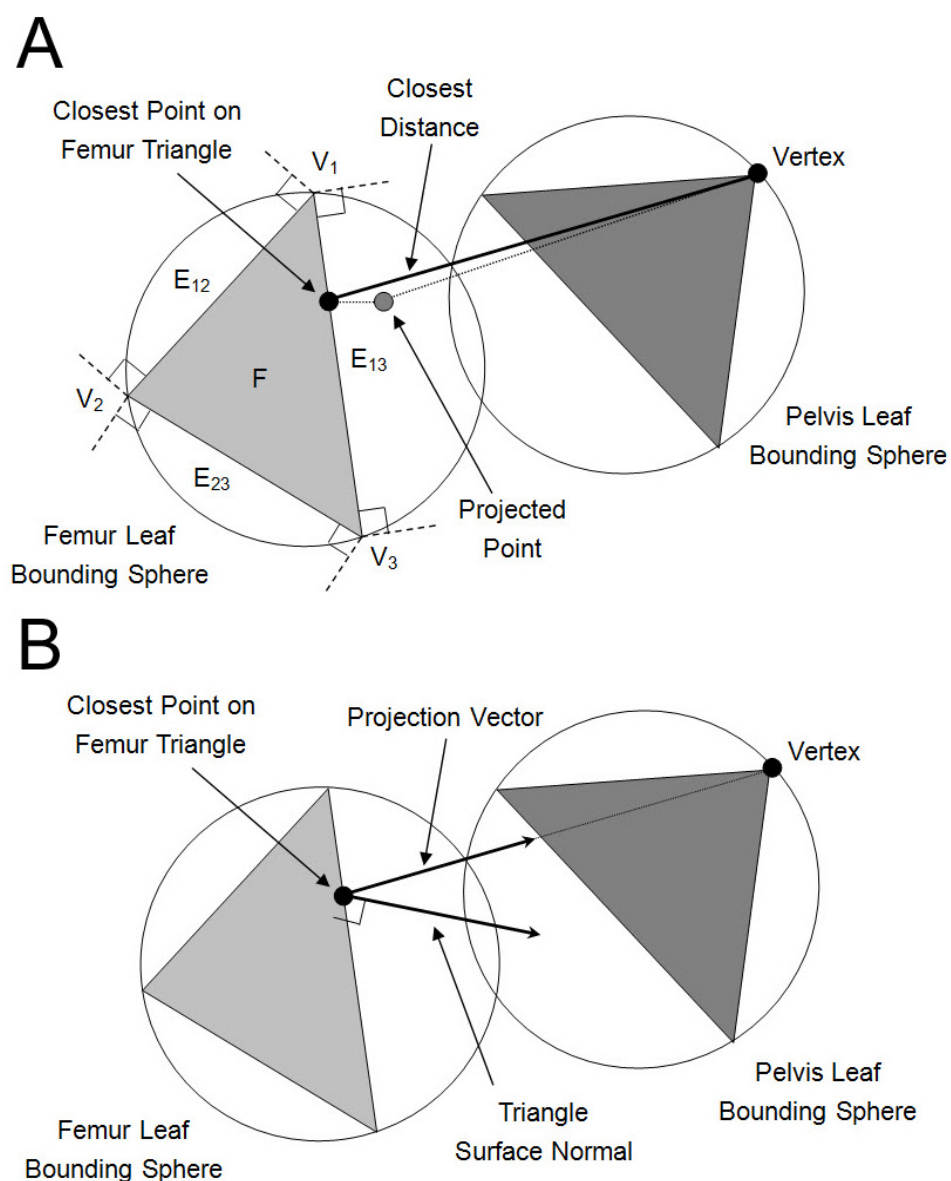
Figure 5-8: Impingement detection in the narrow phase. A) The closest distance from each pelvis vertex to the femur triangle is computed by the Voronoi region method. B) The sign of the closest distance is defined by calculating the dot product of the projection vector and the surface normal of the femur triangle.

To verify impingement detection's precision and accuracy, a phantom consisting of a rotatable shaft and a base with an extruded spike was designed to simulate the ball-and-socket hip joint movement, as shown in Figure 5-9. The phantom was made by a rapid prototyping machine. Reflective markers were attached to the phantom and tracked by the optical tracking system so that the locations of the shaft and spike in space could be determined. Impingement occurred where the shaft contacted the spike. The shaft was designed as cylindrical in shape to ensure that the contact area was as small as possible.

The precision of impingement detection was verified by comparing the measured positions and the virtually detected positions of the impingement. The translation transform from the shaft rotation center, which was the origin of the coordinate system corresponding to the anatomic space accordingly, to the tip of the spike was measured by a CMM, FARO Gage (FARO Technologies Inc., Lake Mary, FL). This transform was the gold-standard for determining the measured position of the spike tip in space, as well as the measured angle (θ) between the z-axis of the coordinate system (pointing superiorly) and a vector connecting the origin and spike tip. It was assumed that impingement occurred at the tip of the spike. When the phantom was placed under the 3D optical tracking system, the impingement virtually detected by the software (through transformations and bounding sphere algorithm) and the physical impingement were compared. The hypothesis was that the measured and detected impingement positions were the same.
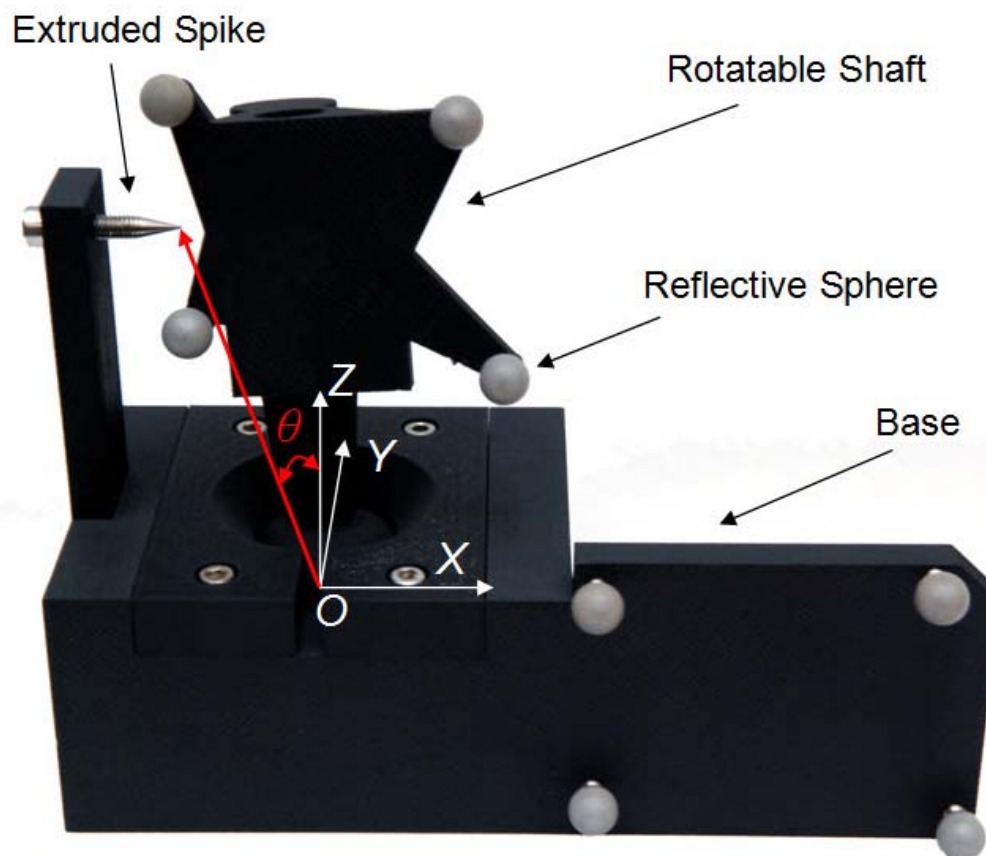
Figure 5-9: Picture of the custom designed phantom used to simulate the ball-and-socket hip joint movement.

Five tests were performed to verify impingement detection precision. The phantom stayed at the same location and the shaft remained in contact with the spike tip for all tests. In each test, the phantom position was tracked 100 times and impingement detection was performed for each position. The detected impingement positions as well as the detected angles were averaged and compared respectively to the measured position and angle.

Next, the accuracy of impingement detection was verified. In order to simulate hip ROM, the shaft was manipulated, under visual observation, to different orientations

relative to the spike. These orientations were defined as "far," "close,", and "contact" positions, representing respectively the spike and the shaft were separated more than 5 mm apart, separated less than 5 mm apart but not contacting, and contacting. Impingement detection was carried out during each manipulation. The impingement detection results were expected to correspond with the observed orientations. Three accuracy verification tests were performed. For each test, 30 arbitrary shaft positions in each orientation (far, close, and contact) for a total of 90 positions were recorded. The results of impingement detection were then compared with the visual observations.

After the completion of the verification, the impingement detection was implemented in the hip ROM simulation software. The software provided functions to simulate hip movement, detect impingements, and return the ROM information based on the pelvis and femur surface models. In order to provide the reference for the ROM, the anatomical coordinate systems were also determined, as illustrated in Figure 5-10. The pelvic coordinate system was established by using the hip center and the "anterior pelvic plane (APP)" (Lewinnek et al., 1978; Tannast et al., 2005), which was formed by the two ASISs and the center of the two pubic tubercles. The femoral coordinate system was defined by the hip center and two epicondyles located at the distal femur.

The neutral position of the simulation was defined as the pelvic and femoral coordinate systems superimposed, assuming that the hip center was the rotation center and no translation occurred. At the neutral position, the X, Y, and Z axes of the pelvic coordinate system (or x, y, and z axes of the femoral coordinate system) were respectively pointing laterally, posteriorly, and superiorly.
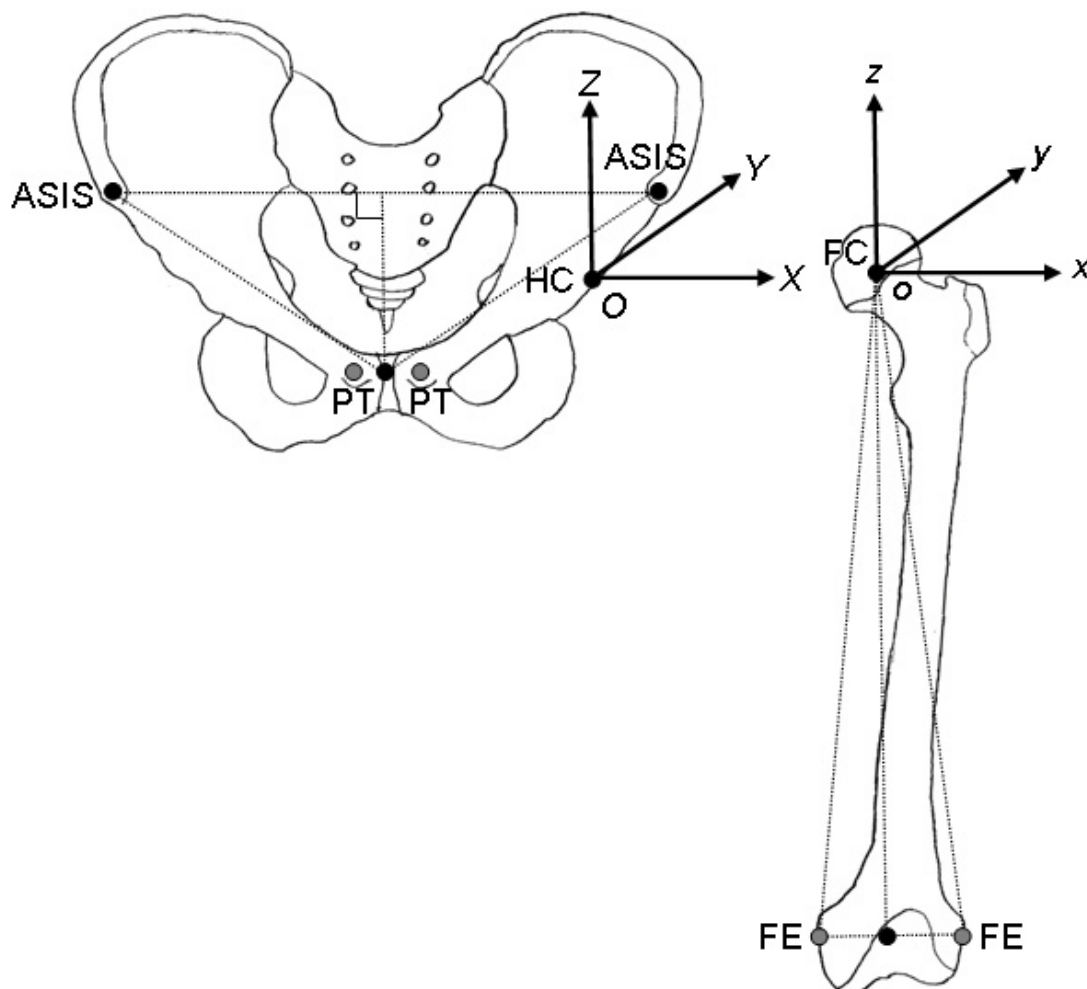
Figure 5-10: Illustration of the anatomical coordinate systems defined for hip ROM simulation. The pelvic coordinate system was defined as follows: O: hip center (HC); X: the axis parallel to the mediolateral axis of the pelvis connecting both ASISs, pointing laterally; Z: the axis perpendicular to the X and extending from the center of the pubic tubercles (PT) to the mediolateral axis, pointing superiorly; Y: the axis orthogonal to the X and Z, pointing posteriorly. The femoral coordinate system was defined as follows: o: femoral head center (FC); z: the axis connecting the center of the two femoral epicondyles (FE) and o, pointing superiorly; y: the axis perpendicular to the plane defined by o and both epicondyles, pointing posteriorly; x: the axis orthogonal to the y and z, pointing laterally.

Simulated six hip movements in this study included flexion, extension, adduction, abduction, external rotation in 90° of flexion, and internal rotation in 90° of flexion. As shown in Figure 5-11, the ROM was determined by virtually rotating the femur (in one degree increments) around the anatomical axes to simulate different hip movements starting from the neutral position. It stopped if an impingement was detected. To be more specific, flexion and extension were described as the femur rotating anteriorly and posteriorly around the X-axis; adduction and abduction were defined as the femur rotating medially and laterally around the Y-axis; external and internal rotation in 90° of flexion were simulated as the femur first rotating around the X-axis to 90° of flexion then externally and internally rotated around the Z-axis. During simulation, the effect of soft tissue and ligaments were not considered; hence only the excessive hip ROM resulting in bone impingement was recorded.

For the hip ROM verification, the RIO Robotic Arm Interactive Orthopedic System and the navigation platform were used. Optical markers were installed on each sawbone so that the position and orientation of the sawbones in space could be recorded by the tracking system. When the markers were detected by the tracking system, the 3D homogeneous matrix transforms $T_{PelvisTrac\ker-To-Camera}$ of the pelvic reference marker and $T_{FemurTrac\ker-To-Camera}$ of the femoral reference marker in camera space were returned by the tracking system (see Figure 5-12 for details). These two transforms provided the relative physical positions between the femoral and pelvic markers. Fiducial marker based paired-point bone registration was employed in this study to obtain the bone registration transform between camera space and image space. The relationship between the bone marker (in camera space) and bone model (in image space) could be established

respectively by acquiring transforms $T_{PelvisTracker-To-PelvisModel}$ of the pelvis and $T_{FemurTracker-To-FemurModel}$ of the femur, through bone registration.

The spatial relationship from the femur surface model to pelvis surface model $T_{FemurModel-To-PelvisModel}$ was established as:

$$T_{FemurModel-To-PelvisModel} = T_{FemurTracker-To-FemurModel}^{-1} \times T_{FemurTracker-To-Camera}$$

$$\times T_{PelvisTracker-To-Camera}^{-1} \times T_{PelvisTracker-To-PelvisModel} \quad (5\text{-}2)$$

Thus,

$$T_{FemurModel-To-PelvisModel} = T_{FemurModel-To-FemurTracker} \times T_{FemurTracker-To-Camera}$$

$$\times T_{Camera-To-PelvisTracker} \times T_{PelvisTracker-To-PelvisModel} \quad (5\text{-}3)$$

By transforming bone surface models using $T_{FemurModel-To-PelvisModel}$, the physical position and orientation of the sawbone femur relative to the sawbone pelvis in space were virtually displayed on the computer.
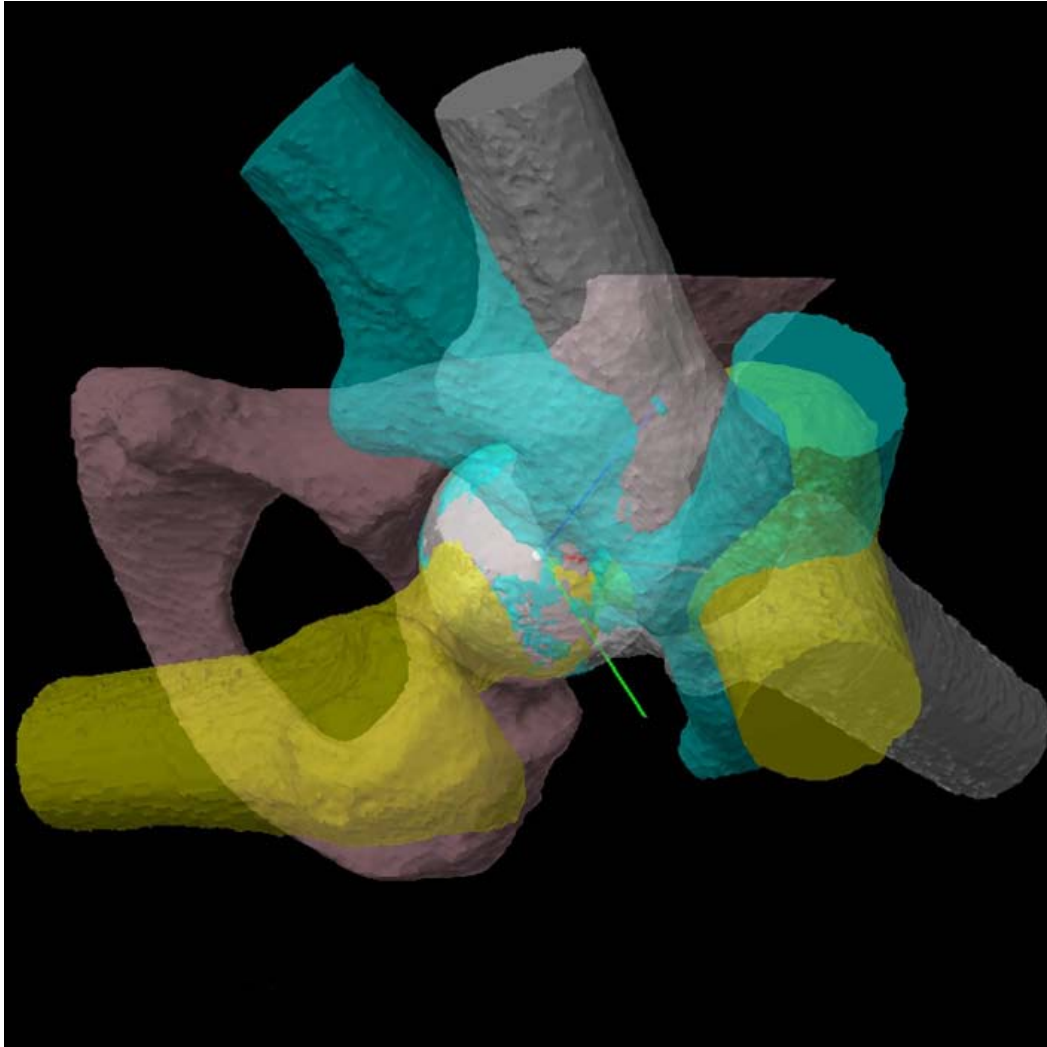
Figure 5-11: Picture of virtual hip ROM simulation. Femur models in gray, yellow, and cyan blue represent respectively the hip movements of flexion and extension, adduction and abduction, and external rotation in 90° flexion and internal rotation in 90° flexion.
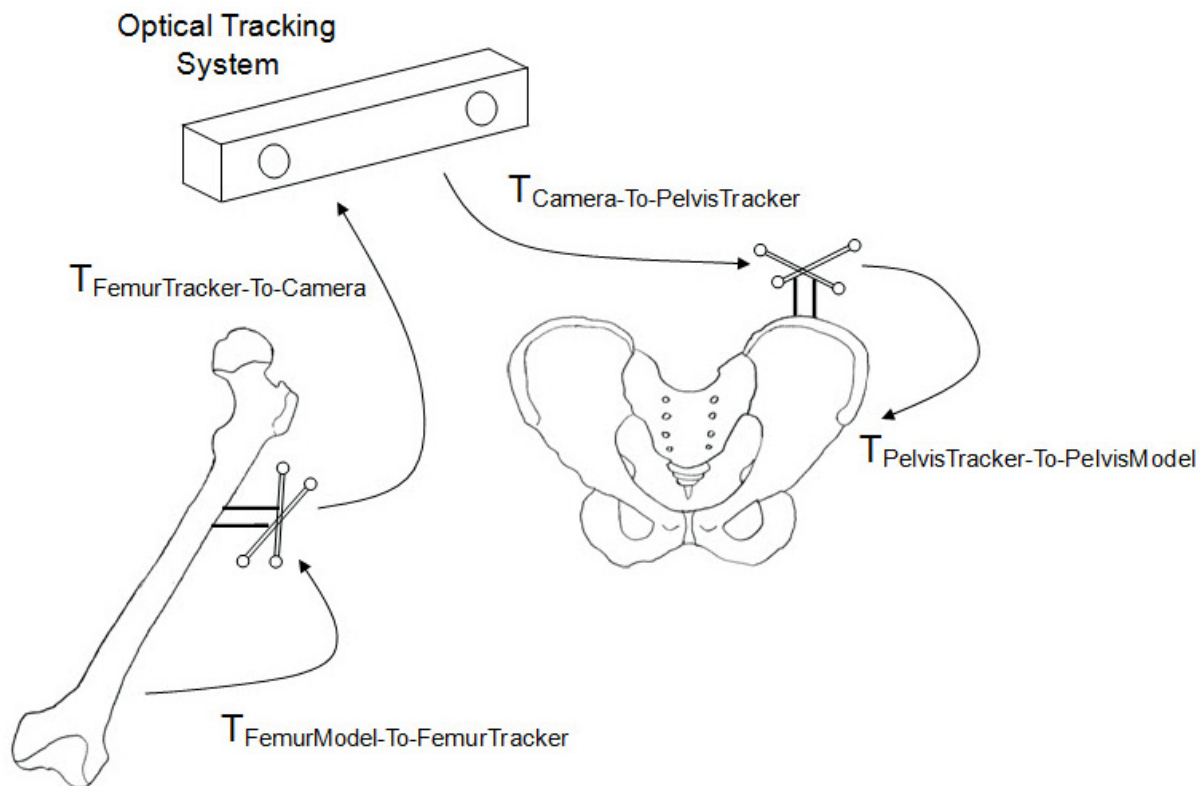
Figure 5-12: Illustration of the 3D transformation of the hip ROM verification.

ROM simulation and verification were carried out for two different groups: 1) healthy pelvis and femur models and 2) healthy pelvis and FAI femur models. The simulated ROM of each specific hip movement was recorded and verified by manual manipulation of the sawbones under the navigation of the optical tracking system, as Figure 5-13 shows. During the verification, the femur was manually rotated around the anatomical axes while the pelvis was fixed in position following the same rotation sequences previously described.
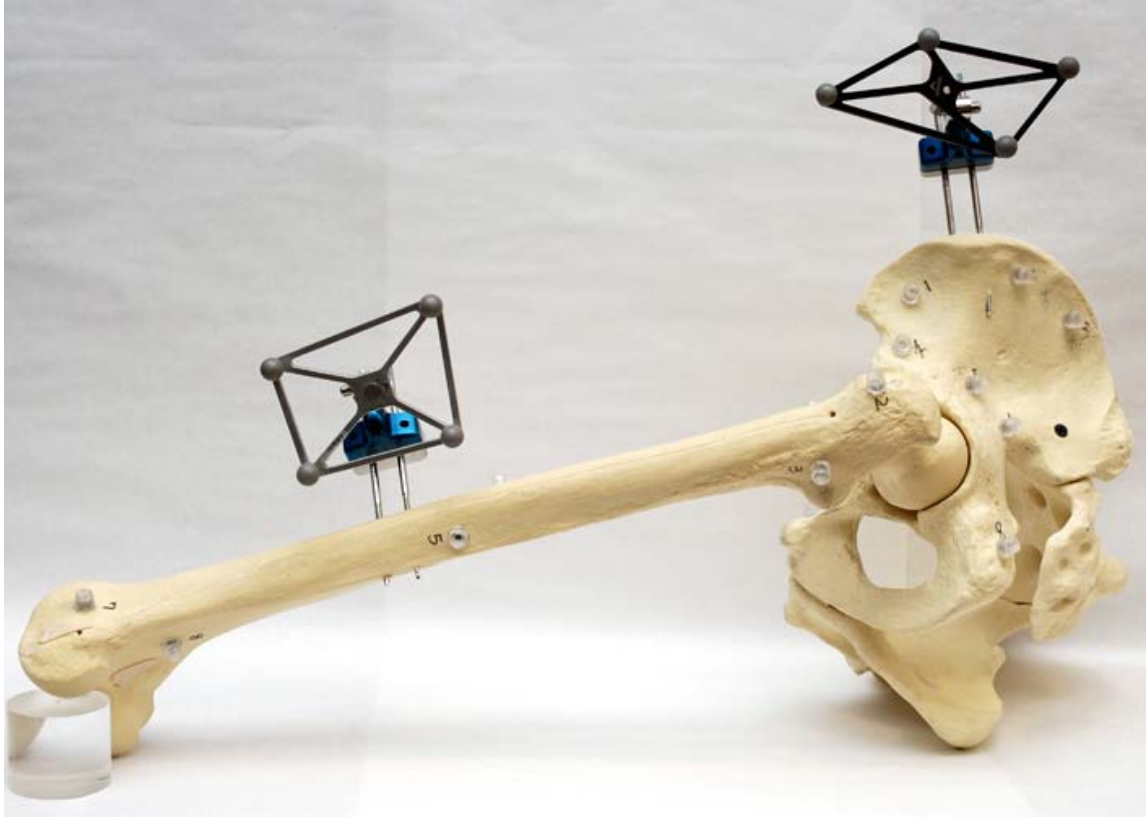
Figure 5-13: Picture of the sawbones and optical markers used for hip ROM verification.

After the completion of the hip ROM verification, a method to determine the resection volume was developed. In order to restore the normal hip ROM, the bony prominence causing the abnormal impingement has to be removed. The amount of the resection was determined based on the spatial information of the abnormal impingement, and the difference between the pathological ROM and the normal ROM defined by the surgeon. Once the resection volume was determined, a surface model of the resection volume was generated. Then, the robotic arm could guide the surgeon to precisely resect the deformities within this generated model.

Hip internal rotation in 90° of flexion was used as an example of the resection volume generation because it was one of the most representative hip movements affected by FAI, and it had been used clinically for assessing the surgical outcome (Philippon et al., 2007a). After hip ROM simulation, the degree of the internal rotation in 90° flexion was recorded and represented as the "pathologic angle." The degree of the internal rotation in 90° flexion that the surgeon wanted to restore was considered as the "to-be-restored angle." By having these two angles, the femur was rotated (in 1 degree of increment in this study) following the same movement trajectory starting from the pathologic angle and stopping at the to-be-restored angle.

All the collision points detected during the rotation between these two angles were recorded. These points formed a "cone-shape" point cloud because in each degree of increment, the collision points distributed in a contour-like formation, as illustrated in Figure 5-14. These contour-like collision points were then stacked up and they formed the cone-shape point cloud with a hollow bottom. This hollow bottom, however, could result in an open surface and became problematic for fitting the point cloud into a surface model. To address this issue, all the collision points were projected onto the bottom of the cone by transforming these points back to the pathologic angle (see Figure 5-15 for detail). Thus, all the detected and projected points could be fitted into a closed surface model representing the resection volume by using the Ball-Pivoting Algorithm (BPA) (Bernardini et al., 1999). The final output of the surface model was created by further smoothing the rough surface of the fitted model.
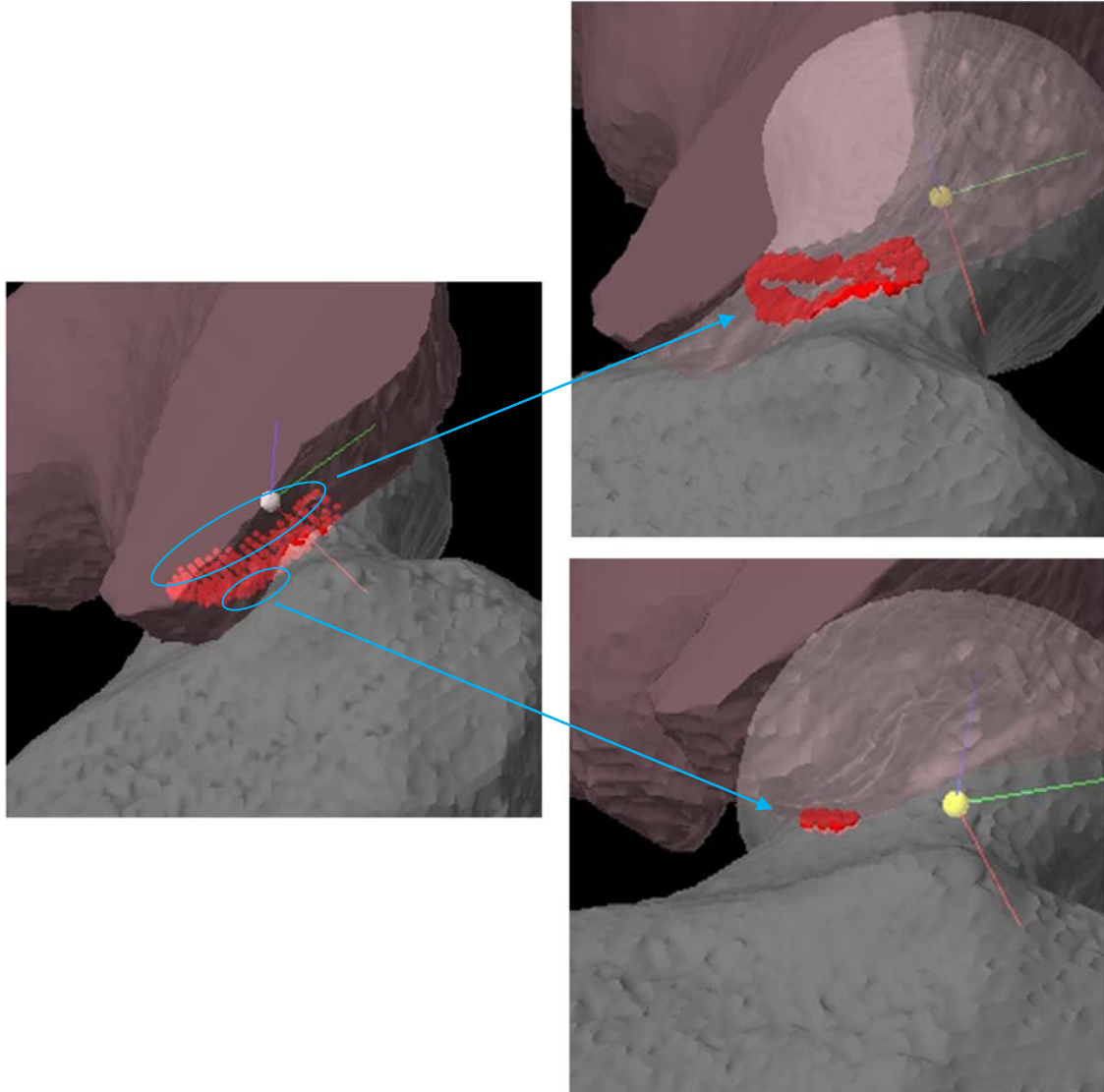
Figure 5-14: Pictures of the cone-shape point cloud. The top portion of the point cloud is formed by the collision points detected at the pathologic angle; the bottom portion is formed by which at the "to-be-restored" angle.
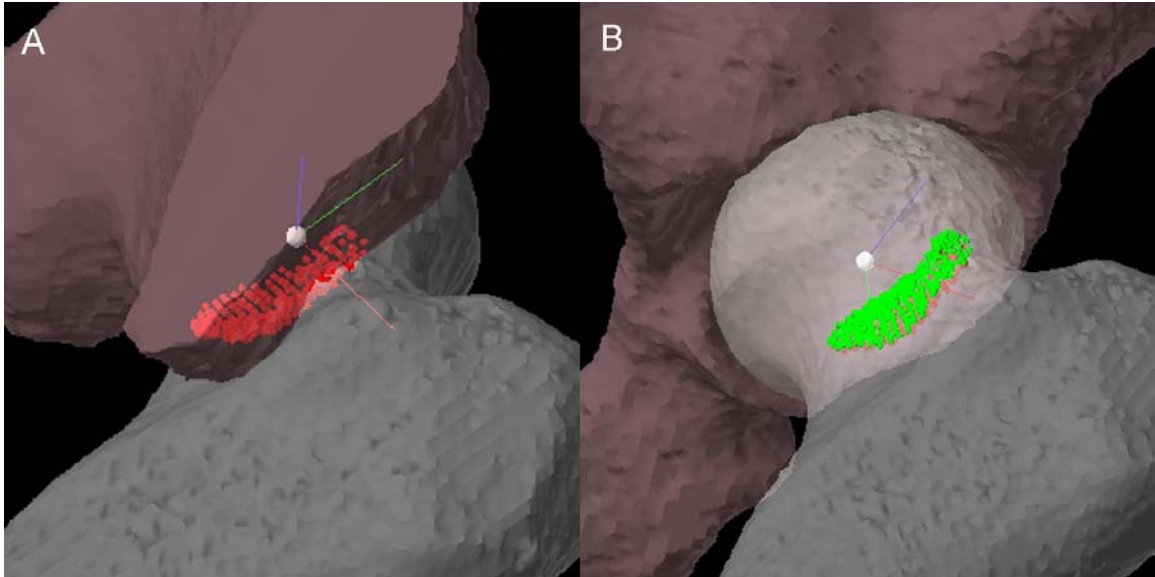
Figure 5-15: A) The point cloud (in the red color) formed by stacking up collision points of each degree of increment. B) The projected points (in the green color) form the bottom of the point cloud.

5.3 RESULTS

After data compression, the vertices of the bone models were reduced to approximate one-sixth of their original sizes. The total time of data compression and bounding sphere tree construction, which were both one-time processes, were 203 seconds and 7 seconds respectively. Table 5-1 shows the detailed computational results of bone model preparation.

For the verification of the impingement detection precision, the 3D coordinates of the measured impingement location (i.e., the spike tip) was (29.38 mm, 0.02 mm, 101.35 mm) in camera space. The mean detected location through five tests was (29.90 ± 0.07 mm, -0.01 ± 0.04 mm, 101.36 ± 0.01 mm) in camera space and the mean distance between the measured and detected impingement location was 0.53 ± 0.06 mm. The

measured angle between the z-axis of the phantom coordinate space and the vector connecting the origin of the phantom coordinate space and spike tip was 16.16°. The mean detected angle through five tests was 16.44 ± 0.03°, and the angular error was 0.28 ± 0.03°. The complete measured and detected impingement results as well as the distance and angular errors are shown in Table 5-2.

Table 5-1: Computational results of bone model preparation.

Surface Model	Pre-compression		Post-compression		Data Processing Time (millisecond)	
	Number of Facet	Number of Vertex	Number of Facet	Number of Vertex	Data Compression	Sphere Tree Construction
Pelvis	81200	243600	81200	40600	89933	4080
Healthy Femur	67224	201672	67224	33614	60168	1690
Cam FAI Femur	62612	187836	62612	31308	53044	1420
Total Time					203145	7190

Table 5-2: Results of the precision verification of the impingement detection (SD = standard deviation).

Category	Impingement Location (mm)			Distance Error (mm)	Angle (Degree)	Angular Error (Degree)
	X	Y	Z			
Measured	29.38	0.02	101.35	-	16.16	-
Test 1	29.88	-0.02	101.37	0.51	16.43	0.27
Test 2	30.01	0.02	101.34	0.63	16.49	0.33
Test 3	29.84	-0.06	101.37	0.47	16.41	0.25
Test 4	29.86	-0.01	101.37	0.49	16.41	0.25
Test 5	29.93	0.04	101.36	0.56	16.45	0.29
Mean	29.90	-0.01	101.36	0.53	16.44	0.28
SD	0.07	0.04	0.01	0.06	0.03	0.03

For the verification of the impingement detection accuracy, no impingement was detected in the "far" or "close" orientations in all three tests (true negative), and the detection accuracy was 100% in these two orientations. In the "contact" orientation, an average of 28.67 true positive detections (out of 30 detections) occurred and resulted in 96% accurate. The average accuracy among all the three orientations was 99% accurate. Table 5-3 shows the results of the accuracy verification of the impingement detection.

Table 5-3: Results of the accuracy verification of the impingement detection (n = 30; TP = true positive; TN = true negative; FP = false positive; FN = false negative).

Category	Far				Close				Contact			
	TP	TN	FP	FN	TP	TN	FP	FN	TP	TN	FP	FN
Test 1	0	30	0	0	0	30	0	0	29	0	0	1
Test 2	0	30	0	0	0	30	0	0	28	0	0	2
Test 3	0	30	0	0	0	30	0	0	29	0	0	2
Mean	0	30	0	0	0	30	0	0	28.67	0	0	1.67
Accuracy	100%				100%				96%			

The overall process time for hip ROM simulation was 7 seconds for both healthy and pathologic groups. Table 5-4 shows the detailed computational time of ROM simulation. The results of ROM simulation and manual verification for the six hip movements are shown in Table 5-5. In the healthy pelvis and femur group, the mean error between the simulated and verified ROM was $0.10 \pm 1.39°$. In the healthy pelvis and pathologic femur group, the mean error was $-2.38 \pm 3.49°$.

For resection volume generation, the internal rotation in 90° of flexion was simulated by using the healthy pelvis and pathologic femur group. The first impingement was detected at 3° of internal rotation, which represented as the pathologic angle. The to-be-restored angle was assumed as 14°. Figure 5-16 illustrates the collision points at

different internal rotation angles; Figure 5-17 shows the point cloud and the generated

surface model of the resection volume.

Table 5-4: Computational time of ROM simulation.

Movement	ROM Simulation Time (millisecond)	
	Healthy Femur	Cam FAI Femur
Flexion	1078	1051
Extension	1109	1161
Adduction	1248	1276
Abduction	1342	1334
External Rotation in 90° of Flexion	1179	1125
Internal Rotation in 90° of Flexion	1214	1191
Total Time	7170	7138

Table 5-5: Results of ROM simulation and manual verification (SD = standard deviation).

Movement	Healthy Femur ROM (Degree)			Cam FAI Femur ROM (Degree)		
	Simulation	Verification	Error	Simulation	Verification	Error
Flexion	102	103.22	-1.22	91	88.71	2.29
Extension	118	117.69	0.31	101	108.45	-7.45
Adduction	70	68.63	1.37	61	61.42	-0.42
Abduction	51	49.58	1.42	49	53.05	-4.05
External Rotation in 90° of Flexion	44	45.95	-1.95	42	46.18	-4.18
Internal Rotation in 90° of Flexion	18	17.35	0.65	3	3.49	-0.49
Mean	-	-	0.10	-	-	-2.38
SD	-	-	1.39	-	-	3.49
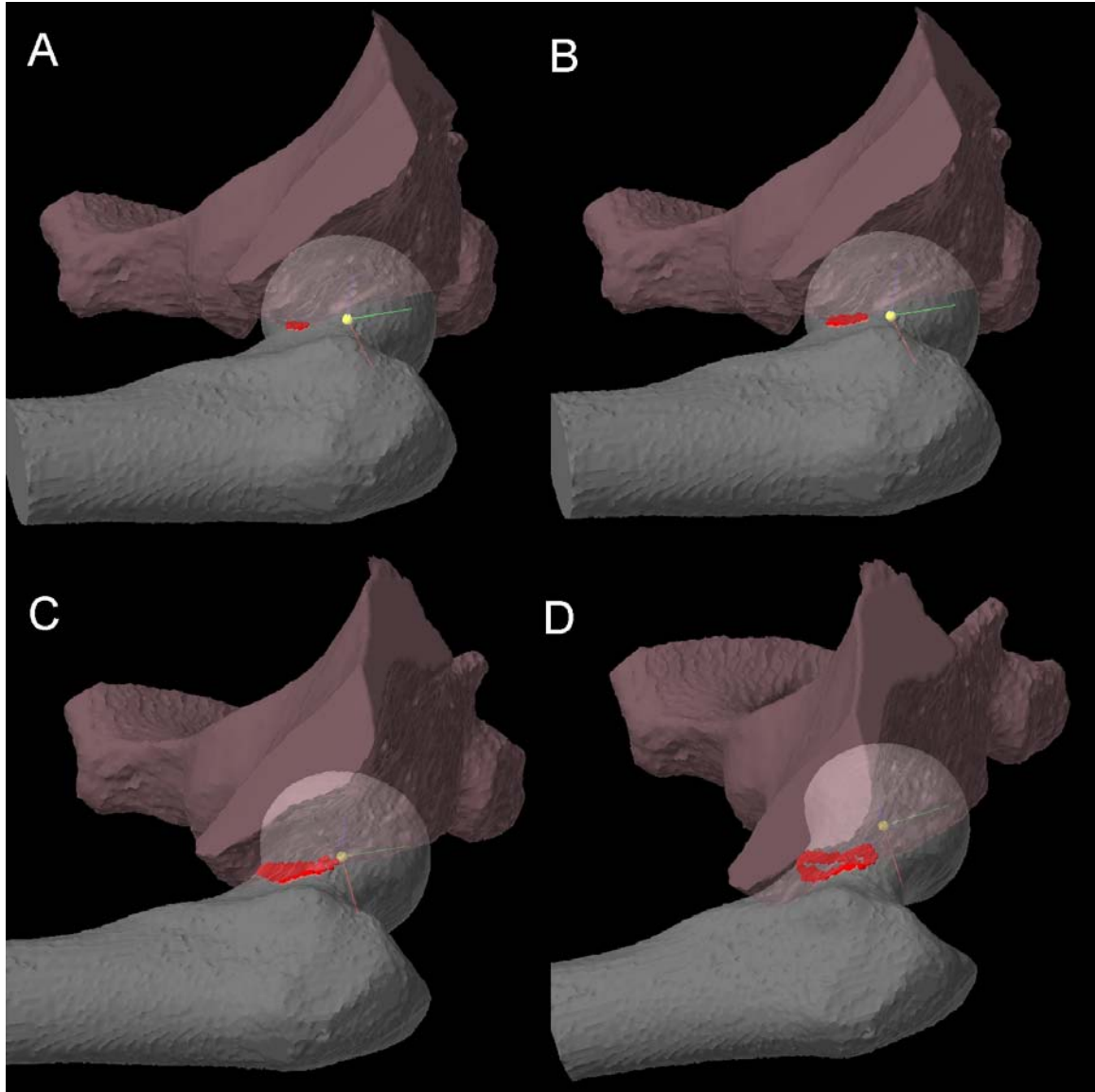
Figure 5-16: Picture of the detected collision points in A) 3 degrees, B) 5 degrees, C) 10 degrees, and D) 14 degrees of internal rotation in 90 degrees of flexion of the hip.
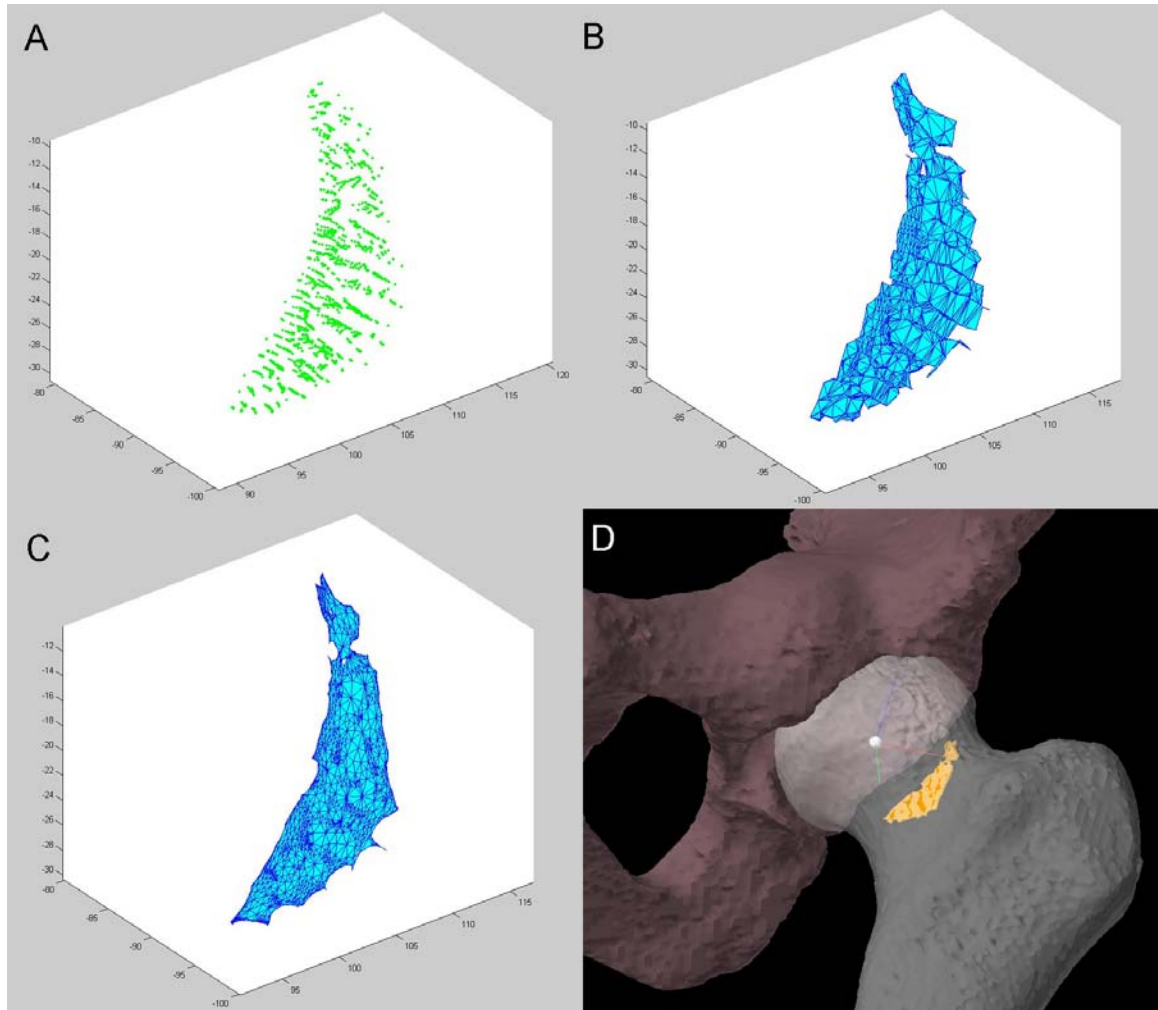
Figure 5-17: Resection volume generation. A) The collision point cloud. B) The surface model generated based on the point cloud. C) Smoothed B model. D) Picture of the resection surface model.

5.4 DISCUSSION

The impingement detection algorithm developed in this study achieves acceptable precision (distance error of 0.53 ± 0.06 mm and angular error of $0.28 \pm 0.03°$) and accuracy (99% accurate among all the three orientations). The small standard deviations in precision verification (0.06 mm and 0.03°) indicate that the distance and angular errors might be the internal errors of the algorithm and can be further calibrated. In addition, compare with the precision and accuracy of impingement detection, larger standard deviations and errors, especially the error from the extension movement in the FAI femur group, are observed in the ROM verification. These errors may result from the bone registration, the sawbone manipulation, and/or the observer's opinion. Above errors together with the existing errors that from the segmentation, the surface model quality, as well as the tracking system (RMS error ≤ 0.25 mm, according to the manufacturer) lead to the overall system error.

The ROM simulation results demonstrate large (>= 9°) decreases in flexion, extension, adduction, and coupled internal rotation in 90° of flexion in patients with cam lesions. No noticeable differences (= 2°) are observed in abduction or coupled external rotation in 90° of flexion. However, in order to reduce the simulation complexity, we assume a fixed rotation center (hip center) during hip movement and neglect the influence of soft tissue, muscles, and ligaments. These assumptions decrease anatomical reality and may result in difference between the simulated and clinically measured results. Prior to a real clinical application, the developed hip ROM simulation system will be further modified and tested with cadaveric evaluation.

In this study, sawbones are manually rotated for verification purpose without considering the influences of cartilages, muscles, or ligaments. These assumptions also reduce anatomical reality and may induce errors to mimic correct position of the joint surfaces and rotation center. To minimize the errors caused by manual manipulation, a custom-designed stretch device will be further developed for verification purpose in order to mechanically manipulate the hip exactly following the defined anatomical axes. In addition, in order to represent more realistically the hip motion, a comprehensive anatomical model simulating the restraints of soft tissue, muscles, and ligaments will be deployed.

The major reason of choosing the bounding sphere model instead of other common bounding volumes (e.g., axis-aligned bounding box or oriented bounding box) is that the bounding sphere requires only the sphere center to be transformed during the intersection test for different bone orientations. This advantage simplifies the computation process and optimizes the performance. Our impingement detection algorithm provides an adjustable detection threshold setting. Users can adjust this threshold in order to calibrate the impingement detection for clinical uses. The developed impingement detection approach can be used for not only FAI but also other orthopedic applications, such as ROM evaluation for hip and knee arthroplasty, gap balancing for total knee arthroplasty, as well as finding the contact points between bones for kinematic research.

During the generation of the resection surface model, multiple impingements are observed in some tests with different "to-be-restored" angles, and result in a "fused" point cloud. The generated surface model based on this point cloud cannot represent

correctly the real resection volume. To address this problem, a method to separate the collision points located in different impingement regions is required. In addition, sharp extrusions and holes exist in the smoothed surface model. These may become problematic while generating the haptic model, which provides the resection boundary for the robot and requires a smooth surface. The surface model needs to be further processed and tested by physical bone cutting.

In conclusion, the chapter demonstrates a pre-operative approach to virtually simulate and predict the functional hip ROM based on given surface models from either healthy or FAI bones. An impingement detection system is developed in this study and results in acceptable precision and accuracy. The impingement detection system is implemented into a hip ROM simulation system to simulate the ROM of 1) healthy pelvis and femur, and 2) healthy pelvis and pathologic femur. The ROM simulation system is verified using a 3D tracking system and results in acceptable accuracy. A resection volume is also generated in order to restore the desired degree of hip ROM. The developed impingement detection and ROM simulation systems may be utilized for other orthopedic applications such as total hip arthroplasty, total knee arthroplasty, as well as kinematic studies.

CHAPTER 6

CONCLUSIONS AND FUTURE DIRECTIONS

FAI has been recognized as a cause of early hip OA, particularly in active young adults and athletes. For FAI surgical treatment, arthroscopic technique has become increasingly popular because of its minimal invasiveness. However, current FAI arthroscopy involves cumbersome procedures and may result in over- or under-resection. To address this issue, robot-assisted FAI arthroscopy is a well suited approach because of its high accuracy and reproducible surgical outcomes.

This dissertation provides new approaches and methods for the current challenges in the development of robot-assisted FAI arthroscopy. Three major studies have been completed, including 1) developing a robust calibration method for the A-mode US probe used for noninvasive bone registration, 2) developing a bone registration simulator for verifying the registration accuracy and consistency for any given point-pattern, and 3) developing a hip ROM simulation system that returns the virtual ROM and determines the bone resection volume based on a given bone model. These works are summarized below, before future research directions are discussed in the final section.

6.1 SUMMARY AND CONTRIBUTIONS

Current bone registration in robot-assisted surgery requires extensive incisions to access the bone surface by using mechanical probes. To tackle this problem, A-mode US has been proposed as a possible solution for noninvasive bone registration. In addition, it

115

has also been indicated that a successful US calibration can greatly reduce the registration errors. In chapter 3, the development of a robust calibration method for a custom made A-mode US probe is given. This method involves using a sphere calibration phantom and a 3D optical tracking system. The calibration is done by finding the transformation representing the correct location of the transmitting/sensing element inside the US transducer housing with the LMA optimization algorithm.

After the calibration, the registration errors are greatly reduced. The experimental results show that the robustness of the calibration method is also satisfactory. With further modifications, the A-mode US probe can be calibrated successfully with the developed method to replace the conventional mechanical probes; hence noninvasive bone registration can be achieved in robot-assisted FAI arthroscopic surgery.

In addition, robot-assisted FAI arthroscopy allows only limited access areas on the bone for digitizing registration points. To assist the surgeon during the procedure, a registration point-pattern not only has points located within these available areas but also consists of minimal number of points that can be used to derive acceptable registration accuracy is desired. Chapter 4 covers a registration simulator based on the surface registration technique to evaluate the registration accuracy for any given point-pattern. The simulator takes a bone model and a point-pattern as the input data, and then virtually registers the points to the model. In order to simulate the real registration process, different registration parameters and randomly generated noises are introduced. Furthermore, point-patterns with various access area combinations and different number of points are tested. The registration simulation is then carried out based on the ICP algorithm and Monte

Carlo simulation. Lastly, the registration accuracy and consistency based on the given pattern are computed.

The experimental results show that the registration point-patterns with widely distributed points result in better accuracy and consistency. They also suggest that a trade-off between the number of points and the registration consistency should be considered while designing the point-pattern for FAI application. The developed simulator not only provides the registration result for evaluating a point-pattern designed for FAI arthroscopy, but also serves as a useful tool for determining the "optimized" registration point-pattern, which leads to superior registration accuracy and requires minimal number of points within the access areas. Hence, with this optimized point-pattern, the surgical trauma and the point digitization time can be greatly reduced.

Furthermore, during the pre-operative planning in robot-assisted FAI arthroscopy, a surgical system that can instantly return the surgical outcome based on the resection plan is highly desired. With the system, the surgeon can hence evaluate the surgical plan and determine the resection volume even before the surgery begins. To respond to this demand, a software system which simulates hip ROM and generates the resection volume based on the given bone model is developed, presented in chapter 5.

An impingement detection system is first developed by utilizing bounding sphere computer graphics algorithm. Both the precision and accuracy of the impingement detection system are verified by using a custom-designed phantom. The impingement detection system is then implanted into a hip ROM simulation system, and the ROM of healthy and FAI diseased bones are simulated. The location of the impingement and the penetration depth between bone models are also returned. Next, the simulated ROM is

verified by manual manipulation of the sawbones under the navigation of a tracking system. Lastly, a resection volume is generated by the system based on the degree of ROM that the surgeon wants to restore.

According to the experimental results, the impingement detection system achieves acceptable precision and accuracy, and the ROM simulation system results in acceptable accuracy. The resection volume is also generated successfully by the system. With further improvement based on the developed system, the surgeon can thus finalize the surgical plan by referring the returned ROM information and suggested resection volume; hence the robotic arm can guide the surgeon to perform accurate bone resection for FAI arthroscopy. In this way, the resection volume can be quantified, the human error can be diminished, and radiation exposure of patients can be reduced.

The works in this study have been presented on international conferences (Chang et al., 2009; Chang et al., 2011a) and published on an international journal (Mozes et al., 2010; Chang et al., 2011b). The major contributions of this research are summarized in Table 6-1 below.

Table 6-1: The major contributions of this dissertation for the development of robot-assisted FAI arthroscopy.

Objectives	Problems	Challenges	Solution: Developments/ Methods	Impacts
A-Mode US Calibration	Current surface-based registration techniques require extensive incisions intra-operatively	A-mode US is ideal to solve this problem, but it needs to be calibrated	A robust calibration method is designed, and it leads to reduced registration error	The calibrated A-mode US can be used for noninvasive bone registration
Registration Point-Pattern Simulator	An optimized registration point-pattern is desired to result in the best accuracy and the shortest point digitization time	A method to verify the designed point-pattern	A registration simulator is created, and it returns the registration results based on the given point-pattern	The simulator can be used to find and verify the optimized point-pattern
Hip ROM Simulation and Verification	The bone resection results can only be assessed after the debridement, and over- or under-resection are likely to occur	A surgical system that can instantly return the surgical outcome based on the resection plan pre-operatively	A software system is developed, and it simulates hip ROM and generates the resection volume based on the given bone model	The surgeon can finalize the surgical plan pre-operatively by referring the returned information from the software system

6.2 FUTURE RESEARCH DIRECTIONS

This dissertation addresses three major challenges in developing a reliable robot-assisted surgical system for FAI arthroscopy. Firstly, for the noninvasive A-mode US bone registration, the calibrated US probe needs to be further tested in the registration schemes with sawbones, cadavers, and real patients. One of the major problems has to be noticed is the generated noisy signals because of the nature of the US. Since the hip anatomy involves a lot of large muscles and soft tissues, the US signals may become too noisy to detect the bone surface for registration correctly. To address this issue, further US signal processing need to be performed.

Secondly, for the registration point-pattern simulator, a more comprehensive study using different point-patterns and noise parameters is necessary. The point-pattern will also be tested with the bone models in different sizes to evaluate the usability and reliability of the pattern. Furthermore, the simulator will be verified by physically testing the point-pattern on sawbones and cadavers. A method to find the optimized point-pattern for FAI arthroscopy will be further developed in conjunction with the developed registration simulator.

Lastly, in regards to the study of hip ROM simulation system, we assume that the hip center is fixed in positions during hip movement and calculate only the extensive ROM without taking the restrictions from the ligaments or soft tissues into accounts. Thus, an extensive study on hip kinematics needs to be carried out in the future. Then the ROM simulation system can be improved by simulating more realistic hip motions as well as taking into account the deformable soft tissues. In addition, based on the current system, a method to generate the optimized resection volume needs to be developed in

order to create a smooth haptic model, which will also need to be further tested by physical bone cutting with the robotic arm. Furthermore, a volume sculpting technique requires to be implemented into the system, so that the surgeon will be able to perform virtual resection on the model and see the resulting ROM instantly.

In terms of the long-term research directions, integration between the software system and the robot system should be carried out in order to develop a reliable robot-assisted surgical system for FAI arthroscopy. Various registration methods such as the US technique and 2D/3D registration can be explored for less invasive procedures and more accurate results. Furthermore, new imaging modalities and segmentation methods may also be studied in order to cope with the loss of accuracy caused by soft tissues. Finally, the developed system is suggested to be used in conjunction with the FAI arthroscopic instruments and operated in a similar manner with the current surgical techniques, so that the learning curve for the surgeon can be minimized.

REFERENCES

Adili, A., (2004). Robot-assisted orthopedic surgery. Semin.Laparosc.Surg. 11, 89-98.

Amin, D. V., Kanade, T., DiGioia, A. M., III, Jaramaz, B., (2003). Ultrasound registration of the bone surface for surgical navigation. Comput.Aided Surg. 8, 1-16.

Amiot, L. P., Lang, K., Putzier, M., Zippel, H., Labelle, H., (2000). Comparative results between conventional and computer-assisted pedicle screw installation in the thoracic, lumbar, and sacral spine. Spine (Phila Pa 1976.) 25, 606-614.

Amiot, L. P., Poulin, F., (2004). Computed tomography-based navigation for hip, knee, and spine surgery. Clin.Orthop.Relat Res. 77-86.

Amstutz, C., Caversaccio, M., Kowal, J., Bachler, R., Nolte, L. P., Hausler, R., Styner, M., (2003). A-mode ultrasound-based registration in computer-aided surgery of the skull. Arch.Otolaryngol.Head Neck Surg. 129, 1310-1316.

Anderson, K. C., Buehler, K. C., Markel, D. C., (2005). Computer assisted navigation in total knee arthroplasty: comparison with conventional methods. J.Arthroplasty 20, 132-138.

Arbabi, E., Boulic, R., Thalmann, D., (2009). Fast collision detection methods for joint surfaces. J.Biomech. 42, 91-99.

Arbabi, E., Boulic, R., Thalmann, D., (2007). A fast method for finding range of motion in the human joints. Conf.Proc.IEEE Eng Med.Biol.Soc. 2007, 5079-5082.

Arbabi, E., Chegini, S., Boulic, R., Tannast, M., Ferguson, S. J., Thalmann, D., (2010). Penetration depth method--novel real-time strategy for evaluating femoroacetabular impingement. J.Orthop.Res. 28, 880-886.

Bargar, W. L., (2007). Robots in orthopaedic surgery: past, present, and future. Clin.Orthop.Relat Res. 463, 31-36.

Barratt, D. C., Davies, A. H., Hughes, A. D., Thom, S. A., Humphries, K. N., (2001). Accuracy of an electromagnetic three-dimensional ultrasound system for carotid artery imaging. Ultrasound Med.Biol. 27, 1421-1425.

Barratt, D. C., Penney, G. P., Chan, C. S., Slomczykowski, M., Carter, T. J., Edwards, P. J., Hawkes, D. J., (2006). Self-calibrating 3D-ultrasound-based bone registration for minimally invasive orthopedic surgery. IEEE Trans.Med.Imaging 25, 312-323.

Beck, M., Kalhor, M., Leunig, M., Ganz, R., (2005). Hip morphology influences the pattern of damage to the acetabular cartilage: femoroacetabular impingement as a cause of early osteoarthritis of the hip. J.Bone Joint Surg.Br. 87**,** 1012-1018.

Bernardini, F., Mittleman, J., Rushmeier, H., Silva, C., Taubin, G., (1999). The ball-pivoting algorithm for surface reconstruction. IEEE Transactions on Visualization and Computer Graphics 5**,** 349-359.

Besl, P. J., Mckay, N. D., (1992). A Method for Registration of 3-D Shapes. IEEE Transactions on Pattern Analysis and Machine Intelligence 14**,** 239-256.

Bizzini, M., Notzli, H. P., Maffiuletti, N. A., (2007). Femoroacetabular impingement in professional ice hockey players: a case series of 5 athletes after open surgical decompression of the hip. Am.J.Sports Med. 35**,** 1955-1959.

Byrd, J. W., (2005). Hip arthroscopy, the supine approach: technique and anatomy of the intraarticular and peripheral compartments. Tech.Orthop. 20**,** 17-31.

Cai, D., Lee, W., Joslin, C., Beaule, PE., (2009). Raipd impingement detection and surface distance measurement system for real-time ball-and-socket joint motion simulation. Int.J.Adv.Media.Comm. 3**,** 5-24.

Chang, T. C., Kang, H., Arata, L., Zhao, W., (2011a). Range of motion simulation and verification for femoroacetabular impingement. Orthopaedic Research Society - ORS 2011 36.

Chang, T. C., Kang, H., Arata, L., Zhao, W., (2011b). A pre-operative approach of range of motion simulation and verification for femoroacetabular impingement. Int.J.Med.Robot.

Chang, T. C., Mozes, A., Arata, L., Zhao, W., (2009). A-mode ultrasound bone registration for computer-assisted knee surgery: calibration and robustness test. 25th Southern Biomedical Engineering Conference - IFMBE 2009, Pt 7, Proceedings 24**,** 97-100.

Conditt, M. A., Roche, M. W., (2009). Minimally invasive robotic-arm-guided unicompartmental knee arthroplasty. J.Bone Joint Surg.Am. 91 Suppl 1**,** 63-68.

Coon, T. M., Driscoll, M. D., Conditt, M. A., (2008). Robotically assisted UKA is more accurate than manually instrumented UKA. Proceedings of the 21st Annual Congress of the International Society of Technology in Arthroplasty, 274.

DiGioia, A. M., III, Plakseychuk, A. Y., Levison, T. J., Jaramaz, B., (2003). Mini-incision technique for total hip arthroplasty with navigation. J.Arthroplasty 18**,** 123-128.

Docquier, P. L., Paul, L., Cartiaux, O., Banse, X., (2009). Registration accuracy in computer-assisted pelvic surgery. Comput.Aided Surg. 14, 37-44.

Dorland, W. A., (2000). Dorland's Illustrated Medical Dictionary. W.B. Saunders Company.

Dorr, L. D., Deshmane, P., (2009). Precision surgery. Orthopedics 32.

Ericson C., (2005). Real-time collision detection. Morgan Kaufmann.

Fieten, L., Schmieder, K., Engelhardt, M., Pasalic, L., Radermacher, K., Heger, S., (2009). Fast and accurate registration of cranial CT images with A-mode ultrasound. Int.J.Comput.Assist.Radiol.Surg. 4, 225-237.

Fieten, L. J., Radermacher, K., Kernenbach, M. A., Heger, S., (2010). Integration of model-based weighting into an ICP variant to account for measurement errors in intra-operative A-Mode ultrasound-based registration. Conf.Proc.IEEE Eng Med.Biol.Soc. 2010, 6264-6267.

Ganz, R., Gill, T. J., Gautier, E., Ganz, K., Krugel, N., Berlemann, U., (2001). Surgical dislocation of the adult hip a technique with full access to the femoral head and acetabulum without the risk of avascular necrosis. J.Bone Joint Surg.Br. 83, 1119-1124.

Ganz, R., Parvizi, J., Beck, M., Leunig, M., Notzli, H., Siebenrock, K. A., (2003). Femoroacetabular impingement: a cause for osteoarthritis of the hip. Clin.Orthop.Relat Res. 112-120.

Gelfand, N., Ikemoto, L., Rusinkiewicz, S., Levoy, M., (2003). Geometrically stable sampling for the ICP algorithm. Proceedings of the Fourth International Conference on 3-D Digital Imaging and Modeling, 2003, 260-267.

Glozman, D., Shoham, M., Fischer, A., (2001). A surface-matching technique for robot-assisted registration. Comput.Aided Surg. 6, 259-269.

Guanche, C. A., Bare, A. A., (2006). Arthroscopic treatment of femoroacetabular impingement. Arthroscopy 22, 95-106.

Hagag, B., Abovitz, R., Kang, H., Schmitz, B., Conditt, M. A., (2010). RIO: Robotic-Arm Interactive Orthopedic System MAKOplasty: User Interactive Haptic Orthopedic Robotics. Surgical robotics : systems, applications, and visions. Springer, pp. 219-246.

Harris, W. H., (1986). Etiology of osteoarthritis of the hip. Clin.Orthop.Relat Res. 20-33.

Heger, S., Mumme, T., Sellei, R., De La, F. M., Wirtz, D. C., Radermacher, K., (2007). A-mode ultrasound-based intra-femoral bone cement detection and 3D reconstruction in RTHR. Comput.Aided Surg. 12**,** 168-175.

Heger, S., Portheine, F., Ohnsorge, J. A., Schkommodau, E., Radermacher, K., (2005). User-interactive registration of bone with A-mode ultrasound. IEEE Eng Med.Biol.Mag. 24**,** 85-95.

Heyworth, B. E., Shindle, M. K., Voos, J. E., Rudzki, J. R., Kelly, B. T., (2007). Radiologic and intraoperative findings in revision hip arthroscopy. Arthroscopy 23**,** 1295-1302.

Horisberger, M., Brunner, A., Herzog, R. F., (2010). Arthroscopic treatment of femoroacetabular impingement of the hip: a new technique to access the joint. Clin.Orthop.Relat Res. 468**,** 182-190.

Hu, Q., Langlotz, U., Lawrence, J., Langlotz, F., Nolte, L. P., (2001). A fast impingement detection algorithm for computer-aided orthopedic surgery. Comput.Aided Surg. 6**,** 104-110.

Hudson, T. C., Lin, M. C., Cohen, J., Gottschalk, S., Manocha, D., (1997). V-COLLIDE: accelerated collision detection for VRML. Proceedings of the 2nd Symposium of Virtual Reality Modeling Language, 1997, 119-125.

Hufner, T., Geerling, J., Kfuri, M., Jr., Gansslen, A., Citak, M., Kirchhoff, T., Sott, A. H., Krettek, C., (2003). Computer assisted pelvic surgery: registration based on a modified external fixator. Comput.Aided Surg. 8**,** 192-197.

Ilizaliturri, V. M., Jr., (2009). Complications of arthroscopic femoroacetabular impingement treatment: a review. Clin.Orthop.Relat Res. 467**,** 760-768.

Jamali, A. A., Scott, R. D., Rubash, H. E., Freiberg, A. A., (2009). Unicompartmental knee arthroplasty: past, present, and future. Am.J.Orthop.(Belle.Mead NJ) 38**,** 17-23.

Jenny, J. Y., Ciobanu, E., Boeri, C., (2007). The rationale for navigated minimally invasive unicompartmental knee replacement. Clin.Orthop.Relat Res. 463**,** 58-62.

Johnston, T. L., Schenker, M. L., Briggs, K. K., Philippon, M. J., (2008). Relationship between offset angle alpha and hip chondral injury in femoroacetabular impingement. Arthroscopy 24**,** 669-675.

Kang, A. C., Gooding, A. J., Coates, M. H., Goh, T. D., Armour, P., Rietveld, J., (2010). Computed tomography assessment of hip joints in asymptomatic individuals in relation to femoroacetabular impingement. Am.J.Sports Med. 38**,** 1160-1165.

Kang, M. J., Sadri, H., Moccozet, L., Magnenat-Thalmann, N., (2003). Hip joint modeling for the control of the joint center and the range of motions. Proceedings of the 5th IFAC Symposium on Modeling and Control in Biomedical Systems, 2003, 23-27.

Kang, M. J., Sadri, H., Moccozet, L., Magnenat-Thalmann, N., Hoffmeyer, P., (2002). Accurate simulation of hip joint range of motion. Proceedings of IEEE Computer Animation, 2002, 215-219.

Kaplan, K. M., Shah, M. R., Youm, T., (2010). Femoroacetabular impingement--diagnosis and treatment. Bull.NYU.Hosp.Jt.Dis. 68, 70-75.

Kassarjian, A., Cerezal, L., Llopis, E., (2006). Femoroacetabular impingement. Top.Magn Reson.Imaging 17, 337-345.

Kawasaki, Y., Ino, F., Sato, Y., Sugano, N., Yoshikawa, H., Tamura, S., Hagihara, K., (2004). Real-time estimation of hip range of motion for total hip replacement surgery. Medical Image Computing and Computer-Assisted Intervention - Miccai 2004, Pt 2, Proceedings 3217, 629-636.

Keogh, M. J., Batt, M. E., (2008). A review of femoroacetabular impingement in athletes. Sports Med. 38, 863-878.

Kowal, J., Amstutz, C., Langlotz, F., Talib, H., Ballester, M. G., (2007). Automated bone contour detection in ultrasound B-mode images for minimally invasive registration in computer-assisted surgery-an in vitro evaluation. Int.J.Med.Robot. 3, 341-348.

Kozak, J., Nesper, M., Fischer, M., Lutze, T., Goggelmann, A., Hassfeld, S., Wetter, T., (2002). Semiautomated registration using new markers for assessing the accuracy of a navigation system. Comput.Aided Surg. 7, 11-24.

Kubiak-Langer, M., Tannast, M., Murphy, S. B., Siebenrock, K. A., Langlotz, F., (2007). Range of motion in anterior femoroacetabular impingement. Clin.Orthop.Relat Res. 458, 117-124.

Kwoh, Y. S., Hou, J., Jonckheere, E. A., Hayati, S., (1988). A robot with improved absolute positioning accuracy for CT guided stereotactic brain surgery. IEEE Trans.Biomed.Eng 35, 153-160.

Lanfranco, A. R., Castellanos, A. E., Desai, J. P., Meyers, W. C., (2004). Robotic surgery: a current perspective. Ann.Surg. 239, 14-21.

Larson, C. M., Wulf, C. A., (2009). Intraoperative fluoroscopy for evaluation of bony resection during arthroscopic management of femoroacetabular impingement in the supine position. Arthroscopy 25, 1183-1192.

Lavigne, M., Parvizi, J., Beck, M., Siebenrock, K. A., Ganz, R., Leunig, M., (2004). Anterior femoroacetabular impingement: part I. Techniques of joint preserving surgery. Clin.Orthop.Relat Res. 61-66.

Leunig, M., Beaule, P. E., Ganz, R., (2009). The concept of femoroacetabular impingement: current status and future perspectives. Clin.Orthop.Relat Res. 467, 616-622.

Levenberg, K., (1944). A method for the solution of certain problems in least squares. Q.Appl.Math. 2, 164-168.

Lewinnek, G. E., Lewis, J. L., Tarr, R., Compere, C. L., Zimmerman, J. R., (1978). Dislocations after total hip-replacement arthroplasties. J.Bone Joint Surg. 60, 217-220.

Lonner, J. H., John, T. K., Conditt, M. A., (2010). Robotic arm-assisted UKA improves tibial component alignment: a pilot study. Clin.Orthop.Relat Res. 468, 141-146.

Luring, C., Beckmann, J., Haibock, P., Perlick, L., Grifka, J., Tingart, M., (2008). Minimal invasive and computer assisted total knee replacement compared with the conventional technique: a prospective, randomised trial. Knee.Surg.Sports Traumatol.Arthrosc. 16, 928-934.

Luwig, G., (1950). The velocity of sound through tissues and the acoustic impedance of tissues. J.Acoust.Soc.Am. 22, 862-866.

Ma, B., Ellis, R. E., (2003). Robust registration for computer-integrated orthopedic surgery: laboratory validation and clinical experience. Med.Image Anal. 7, 237-250.

Mardones, R., Lara, J., Donndorff, A., Barnes, S., Stuart, M. J., Glick, J., Trousdale, R., (2009). Surgical correction of "cam-type" femoroacetabular impingement: a cadaveric comparison of open versus arthroscopic debridement. Arthroscopy 25, 175-182.

Mardones, R. M., Gonzalez, C., Chen, Q., Zobitz, M., Kaufman, K. R., Trousdale, R. T., (2005). Surgical treatment of femoroacetabular impingement: evaluation of the effect of the size of the resection. J.Bone Joint Surg.Am. 87, 273-279.

Marieb, E. N., Mallatt, J., (1996). Human Anatomy. Benjamin Cummings.

Marquardt, D. W., (1963). An algorithm for least-squares estimation of nonlinear parameters. SIAM.J.Appl.Math. 11, 431-441.

Matsuda, D. K., (2009). Fluoroscopic templating technique for precision arthroscopic rim trimming. Arthroscopy 25, 1175-1182.

Mercier, L., Lango, T., Lindseth, F., Collins, D. L., (2005). A review of calibration techniques for freehand 3-D ultrasound systems. Ultrasound Med.Biol. 31, 449-471.

Metropolis, N., Ulam, S., (1949). The Monte Carlo Method. Journal of the American Statistical Association 44**,** 335-341.

Meyer, D. C., Beck, M., Ellis, T., Ganz, R., Leunig, M., (2006). Comparison of six radiographic projections to assess femoral head/neck asphericity. Clin.Orthop.Relat Res. 445**,** 181-185.

Moulder, C., Sati, M., Wentkowski, M. V., Nolte, L. P., (2003). A transcutaneous bone digitizer for minimally invasive registration in orthopedics: a real-time focused ultrasound beam approach. Comput.Aided Surg. 8**,** 120-128.

Mozes, A., Chang, T. C., Arata, L., Zhao, W., (2010). Three-dimensional A-mode ultrasound calibration and registration for robotic orthopaedic knee surgery. Int.J.Med.Robot. 6**,** 91-101.

Murphy, S., Tannast, M., Kim, Y. J., Buly, R., Millis, M. B., (2004). Debridement of the adult hip for femoroacetabular impingement: indications and preliminary clinical results. Clin.Orthop.Relat Res. 178-181.

Notzli, H. P., Wyss, T. F., Stoecklin, C. H., Schmid, M. R., Treiber, K., Hodler, J., (2002). The contour of the femoral head-neck junction as a predictor for the risk of anterior impingement. J.Bone Joint Surg.Br. 84**,** 556-560.

Oszwald, M., Citak, M., Kendoff, D., Kowal, J., Amstutz, C., Kirchhoff, T., Nolte, L. P., Krettek, C., Hufner, T., (2008). Accuracy of navigated surgery of the pelvis after surface matching with an a-mode ultrasound probe. J.Orthop.Res. 26**,** 860-864.

Pearle, A. D., O'Loughlin, P. F., Kendoff, D. O., (2010). Robot-assisted unicompartmental knee arthroplasty. J.Arthroplasty 25**,** 230-237.

Peters, C. L., Erickson, J. A., (2006b). Treatment of femoro-acetabular impingement with surgical dislocation and debridement in young adults. J.Bone Joint Surg.Am. 88**,** 1735-1741.

Peters, C. L., Erickson, J. A., (2006a). Treatment of femoro-acetabular impingement with surgical dislocation and debridement in young adults. J.Bone Joint Surg.Am. 88**,** 1735-1741.

Philippon, M. J., Maxwell, R. B., Johnston, T. L., Schenker, M., Briggs, K. K., (2007a). Clinical presentation of femoroacetabular impingement. Knee.Surg.Sports Traumatol.Arthrosc. 15**,** 1041-1047.

Philippon, M. J., Stubbs, A. J., Schenker, M. L., Maxwell, R. B., Ganz, R., Leunig, M., (2007b). Arthroscopic management of femoroacetabular impingement: osteoplasty technique and literature review. Am.J.Sports Med. 35**,** 1571-1580.

Richolt, J. A., Teschner, M., Everett, P. C., Millis, M. B., Kikinis, R., (1999). Impingement simulation of the hip in SCFE using 3D models. Comput.Aided Surg. 4**,** 144-151.

Roche, M. W., Augustin, D., Conditt, M. A., (2008). Accuracy of robotically assisted UKA. Proceedings of the 21st Annual Congress of the International Society of Technology in Arthroplasty, 175.

Rusinkiewicz, S., Levoy, M., (2001). Efficient variants of the ICP algorithm. Proceedings of the Third International Conference on 3-D Digital Imaging and Modeling, 2001, 145-152.

Schlenzka, D., Laine, T., Lund, T., (2000). Computer-assisted spine surgery. Eur.Spine J. 9 Suppl 1**,** S57-S64.

Simon, D., (1996). Shape-based registration. Ph.D. Dissertation Carnegie Mellon University.

Sinha, R. K., Plush, R., Weems, V. J., (2008). Unicompartmental arthroplasty using a tactile guided system. Proceedings of the 21st Annual Congress of the International Society of Technology in Arthroplasty, 276.

Stulberg, S. D., Cordell, L. D., Harris, W. H., Ramsey, P. L., MacEwen, G. D., (1975). Unrecognized childhood hip disease: a major cause of idiopathic osteoarthritis of the hip. Proceedings of the Third Open Scientific Meeting of the Hip society, 2112-2228.

Stulberg, S. D., Harris, W. H., (1974). Acetabular dysplasia and development of osteoarthritis of hip. Proceedings of the Second Open Scientific Meeting of the Hip Society, 82-93.

Sugano, N., Sasama, T., Sato, Y., Nakajima, Y., Nishii, T., Yonenobu, K., Tamura, S., Ochi, T., (2001). Accuracy evaluation of surface-based registration methods in a computer navigation system for hip surgery performed through a posterolateral approach. Comput.Aided Surg. 6**,** 195-203.

Sun, H., Inaoka, H., Fukuoka, Y., Masuda, T., Ishida, A., Morita, S., (2007). Range of motion measurement of an artificial hip joint using CT images. Med.Biol.Eng Comput. 45**,** 1229-1235.

Tannast, M., Kubiak-Langer, M., Langlotz, F., Puls, M., Murphy, S. B., Siebenrock, K. A., (2007a). Noninvasive three-dimensional assessment of femoroacetabular impingement. J.Orthop.Res. 25**,** 122-131.

Tannast, M., Langlotz, U., Siebenrock, K. A., Wiese, M., Bernsmann, K., Langlotz, F., (2005). Anatomic referencing of cup orientation in total hip arthroplasty. Clin.Orthop.Relat Res. 144-150.

Tannast, M., Siebenrock, K. A., Anderson, S. E., (2007b). Femoroacetabular impingement: radiographic diagnosis--what the radiologist should know. AJR Am.J.Roentgenol. 188**,** 1540-1552.

Tanzer, M., Noiseux, N., (2004). Osseous abnormalities and early osteoarthritis: the role of hip impingement. Clin.Orthop.Relat Res. 170-177.

Widmer, K. H., Grutzner, P. A., (2004). Joint replacement-total hip replacement with CT-based navigation. Injury 35 Suppl 1**,** S-9.

APPENDIX A

Three-Dimensional Transformation

In the present study, only a 3D rigid transformation is used considering the bone is a non-deformable object. The rigid transformation is presented as a 4×4 homogenous matrix:

$$\begin{bmatrix} a & b & c & 0 \\ d & e & f & 0 \\ g & h & i & 0 \\ T_x & T_y & T_z & 1 \end{bmatrix}$$

where T_x T_y T_z represent the translation about the x, y, and z-axes; $a \sim i$ represent the rotation. The scale components are fixed so that there is no scaling and shearing for rigid transformation. The transformation matrices of the counterclockwise rotation about the x, y, and z-axes are denoted as T_{rx}, T_{ry}, and T_{rz}:

$$T_{rx}(\theta) = \begin{bmatrix} 1 & 0 & 0 & 0 \\ 0 & \cos\theta & -\sin\theta & 0 \\ 0 & \sin\theta & \cos\theta & 0 \\ 0 & 0 & 0 & 1 \end{bmatrix}$$

$$T_{ry}(\theta) = \begin{bmatrix} \cos\theta & 0 & \sin\theta & 0 \\ 0 & 1 & 0 & 0 \\ -\sin\theta & 0 & \cos\theta & 0 \\ 0 & 0 & 0 & 1 \end{bmatrix}$$

131

$$T_{rz}(\theta) = \begin{bmatrix} \cos\theta & -\sin\theta & 0 & 0 \\ \sin\theta & \cos\theta & 0 & 0 \\ 0 & 0 & 1 & 0 \\ 0 & 0 & 0 & 1 \end{bmatrix}$$

By using these rotation matrices, the Euler angle of the rotation about x, y ,and z axes in XYZ convention can be calculated as:

$$T_{rx}(\theta_1) \times T_{ry}(\theta_2) \times T_{rz}(\theta_3)$$

$$= \begin{bmatrix} 1 & 0 & 0 & 0 \\ 0 & \cos\theta_1 & -\sin\theta_1 & 0 \\ 0 & \sin\theta_1 & \cos\theta_1 & 0 \\ 0 & 0 & 0 & 1 \end{bmatrix} \times \begin{bmatrix} \cos\theta_2 & 0 & \sin\theta_2 & 0 \\ 0 & 1 & 0 & 0 \\ -\sin\theta_2 & 0 & \cos\theta_2 & 0 \\ 0 & 0 & 0 & 1 \end{bmatrix} \times \begin{bmatrix} \cos\theta_3 & -\sin\theta_3 & 0 & 0 \\ \sin\theta_3 & \cos\theta_3 & 0 & 0 \\ 0 & 0 & 1 & 0 \\ 0 & 0 & 0 & 1 \end{bmatrix}$$

$$= \begin{bmatrix} \cos\theta_2\cos\theta_3 & -\cos\theta_2\sin\theta_3 & \sin\theta_2 & 0 \\ \cos\theta_1\sin\theta_3 + \cos\theta_3\sin\theta_1\sin\theta_2 & \cos\theta_1\cos\theta_3 - \sin\theta_1\sin\theta_2\sin\theta_3 & -\cos\theta_2\sin\theta_1 & 0 \\ \sin\theta_1\sin\theta_3 - \cos\theta_1\cos\theta_3\sin\theta_2 & \cos\theta_1\sin\theta_2\sin\theta_3 + \cos\theta_3\sin\theta_1 & \cos\theta_1\cos\theta_2 & 0 \\ 0 & 0 & 0 & 1 \end{bmatrix}$$

In addition, a 3D point in space $P = [X \quad Y \quad Z]$ can be transformed to $P' = [X' \quad Y' \quad Z']$ by following equation:

$$[X \quad Y \quad Z \quad 1] \times \begin{bmatrix} a & b & c & 0 \\ d & e & f & 0 \\ g & h & i & 0 \\ T_x & T_y & T_z & 1 \end{bmatrix} = [X' \quad Y' \quad Z' \quad 1]$$

Furthermore, an identity matrix I is denoted as:

$$I = \begin{bmatrix} 1 & 0 & 0 & 0 \\ 0 & 1 & 0 & 0 \\ 0 & 0 & 1 & 0 \\ 0 & 0 & 0 & 1 \end{bmatrix}$$

The 3D point in space $P = [X \quad Y \quad Z]$ transformed with the identity matrix I results in

$P' = P = [X \quad Y \quad Z]$ by following equation:

$$[X \quad Y \quad Z \quad 1] \times \begin{bmatrix} 1 & 0 & 0 & 0 \\ 0 & 1 & 0 & 0 \\ 0 & 0 & 1 & 0 \\ 0 & 0 & 0 & 1 \end{bmatrix} = [X \quad Y \quad Z \quad 1]$$

APPENDIX B

Application of Levenberg-Marquardt algorithm for A-mode ultrasound calibration

1. Sphere radius: R

2. Sphere center in camera space: $C = [X_c \quad Y_c \quad Z_c] = [C_1 \quad C_2 \quad C_3]$

3. Number of collected surface points: i

4. Measured initial offset in probe space: $T_{Transducer-To-Mar\,ker} = [T_x \quad T_y \quad T_z]$

5. Ultrasound distance of each surface point: d_i

6. Camera returned transformation of the marker origin in camera space:

$$\begin{bmatrix} a_{11i} & a_{12i} & a_{13i} & 0 \\ a_{21i} & a_{22i} & a_{23i} & 0 \\ a_{31i} & a_{32i} & a_{33i} & 0 \\ T_{1i} & T_{2i} & T_{3i} & 1 \end{bmatrix}$$

where $T_{1i} \quad T_{2i} \quad T_{3i}$ represent the translation about the x, y, and z-axes; $a_{11i} \sim a_{33i}$ represent the rotation.

7. Distance between each collected surface point to the sphere center: D_i

$$D_i = \left(\left(\begin{bmatrix} T_x & T_y & T_z + d_i & 1 \end{bmatrix} \times \begin{bmatrix} a_{11i} & a_{12i} & a_{13i} & 0 \\ a_{21i} & a_{22i} & a_{23i} & 0 \\ a_{31i} & a_{32i} & a_{33i} & 0 \\ T_{1i} & T_{2i} & T_{3i} & 1 \end{bmatrix} - \begin{bmatrix} C_1 & C_2 & C_3 & 1 \end{bmatrix} \right) \times \\ \left(\begin{bmatrix} T_x & T_y & T_z + d_i & 1 \end{bmatrix} \times \begin{bmatrix} a_{11i} & a_{12i} & a_{13i} & 0 \\ a_{21i} & a_{22i} & a_{23i} & 0 \\ a_{31i} & a_{32i} & a_{33i} & 0 \\ T_{1i} & T_{2i} & T_{3i} & 1 \end{bmatrix} - \begin{bmatrix} C_1 & C_2 & C_3 & 1 \end{bmatrix} \right)^T \right)^{\frac{1}{2}}$$

$$= \left(\sum_j^3 \left(a_{1ji} T_x + a_{2ji} T_y + a_{3ji} (T_z + d_i) + T_{ji} - C_j \right)^2 \right)^{\frac{1}{2}}$$

8. Error of each point: ε_i

$$\varepsilon_i = |D_i - R|$$

$$= \left| \left(\sum_j^3 \left(a_{1ji} T_x + a_{2ji} T_y + a_{3ji} (T_z + d_i) + T_{ji} - C_j \right)^2 \right)^{\frac{1}{2}} - R \right|$$

9. Initial total error: E_o

$$E_o = \left(\sum_i \varepsilon_i^2 \right)^{\frac{1}{2}}$$

10. For error at each point, taking partial derivative with respect to Tx, Ty, Tz, we

obtain $\dfrac{\partial \varepsilon_i}{\partial T_x}$, $\dfrac{\partial \varepsilon_i}{\partial T_y}$, and $\dfrac{\partial \varepsilon_i}{\partial T_z}$.

11. For Levenberg-Marquardt algorithm, we first calculate the Jacobian Matrix: J

$$J = \begin{bmatrix} \dfrac{\partial \varepsilon_1}{\partial T_x} & \dfrac{\partial \varepsilon_1}{\partial T_y} & \dfrac{\partial \varepsilon_1}{\partial T_z} \\ \vdots & \vdots & \vdots \\ \dfrac{\partial \varepsilon_i}{\partial T_x} & \dfrac{\partial \varepsilon_i}{\partial T_y} & \dfrac{\partial \varepsilon_i}{\partial T_z} \end{bmatrix}$$

12. Levenberg-Marquardt algorithm:

Damping factor: λ

Increment: δ

$$\delta = \begin{bmatrix} \delta_x \\ \delta_y \\ \delta_z \end{bmatrix}$$

Identity matrix: I

$$I = \begin{bmatrix} 1 & 0 & 0 \\ 0 & 1 & 0 \\ 0 & 0 & 1 \end{bmatrix}$$

Levenberg-Marquardt algorithm optimization equation:

$$\left(J^T J + \lambda I \right) \delta = J^T \varepsilon_i$$

$$\delta = \frac{J^T \varepsilon_i}{\left(J^T J + \lambda I \right)}$$

$$\begin{bmatrix} \delta_x \\ \delta_y \\ \delta_z \end{bmatrix} = \cfrac{\begin{bmatrix} \dfrac{\partial \varepsilon_1}{\partial T_x} & \cdots & \dfrac{\partial \varepsilon_i}{\partial T_x} \\ \dfrac{\partial \varepsilon_1}{\partial T_y} & \cdots & \dfrac{\partial \varepsilon_i}{\partial T_y} \\ \dfrac{\partial \varepsilon_1}{\partial T_z} & \cdots & \dfrac{\partial \varepsilon_i}{\partial T_z} \end{bmatrix} \times \begin{bmatrix} \varepsilon_1 \\ \vdots \\ \varepsilon_i \end{bmatrix}}{\begin{bmatrix} \dfrac{\partial \varepsilon_1}{\partial T_x} & \cdots & \dfrac{\partial \varepsilon_i}{\partial T_x} \\ \dfrac{\partial \varepsilon_1}{\partial T_y} & \cdots & \dfrac{\partial \varepsilon_i}{\partial T_y} \\ \dfrac{\partial \varepsilon_1}{\partial T_z} & \cdots & \dfrac{\partial \varepsilon_i}{\partial T_z} \end{bmatrix} \times \begin{bmatrix} \dfrac{\partial \varepsilon_1}{\partial T_x} & \dfrac{\partial \varepsilon_1}{\partial T_y} & \dfrac{\partial \varepsilon_1}{\partial T_z} \\ \vdots & \vdots & \vdots \\ \dfrac{\partial \varepsilon_i}{\partial T_x} & \dfrac{\partial \varepsilon_i}{\partial T_y} & \dfrac{\partial \varepsilon_i}{\partial T_z} \end{bmatrix} + \lambda \begin{bmatrix} 1 & 0 & 0 \\ 0 & 1 & 0 \\ 0 & 0 & 1 \end{bmatrix}}$$

13. New offset: $T_{Transducer-To-Mar\,ker} = [T_x + \delta_x \quad T_y + \delta_y \quad T_z + \delta_z]$

14. New error of each surface point: ε_{Ni}

$$\varepsilon_{Ni} = \left| \left(\sum_j^3 \left(a_{1ji}(T_x + \delta_x) + a_{2ji}(T_y + \delta_y) + a_{3ji}(T_z + \delta_z + d_i) + T_{ji} - C_j \right)^2 \right)^{\frac{1}{2}} - R \right|$$

15. New total error: E_N

$$E_N = \left(\sum_i \varepsilon_{Ni}{}^2 \right)^{\frac{1}{2}}$$

16. If $E_N < E_0$

$$\begin{aligned} T_x &= T_x + \delta_x \\ T_y &= T_y + \delta_y \\ T_z &= T_z + \delta_z \\ \lambda &= \lambda / 10 \\ E_0 &= E_N \end{aligned}$$

Else

$$\lambda = \lambda \times 10$$

17. Iterate step 7~16 to optimize the final offset $T_{Transducer-To-Mar\,\mathrm{ker}}$.